Direct numerical simulation of transitional multicomponent-species gaseous and multicomponent-liquid drop-laden mixing layers

By LAURENT C. SELLE[1]
AND JOSETTE BELLAN[1,2]

[1]California Institute of Technology, Pasadena, CA 91125, USA

[2]Jet Propulsion Laboratory, California Institute of Technology, Pasadena, CA 91109, USA

(Received 1 August 2005)

A model of multicomponent-liquid (MC-liquid) drop evaporation in a three-dimensional mixing layer is here exercised at larger Reynolds numbers than in a previous study, and transitional states are obtained. The gas phase is followed in an Eulerian frame and the multitude of drops is described in a Lagrangian frame. Complete coupling between phases is included, with source terms in the gas conservation equations accounting for the drop/flow interaction in terms of drop drag, drop heating and species evaporation. The liquid composition, initially specified as a single-Gamma (SG) probability distribution function (PDF) depending on the molar mass is allowed to evolve into a linear combination of two SGPDFs, called the double-Gamma PDF (DGPDF). The compositions of liquid and vapor emanating from the drops are calculated through four moments of the DGPDFs, which are drop-specific and location-specific, respectively. The mixing layer is initially excited to promote the double pairing of its four initial spanwise vortices into an ultimate vortex in which small scales proliferate. Simulations are performed for four

liquids of different compositions and the effect of the initial mass loading and initial free-stream gas temperature are explored. For reference, simulations are also performed for gaseous multicomponent mixing layers for which the effect of Reynolds number is investigated. The results encompass examination of the global layer characteristics, flow visualizations and homogeneous-plane statistics at transition. Comparisons are performed with previous pre-transitional MC-liquid simulations and with transitional single-component (SC) liquid studies. It is found that in MC flows at transition, the classical energy cascade is of similar strength, but that the smallest scales contain orders of magnitude less energy than SC flows, which is confirmed by the larger viscous dissipation in the former case. Contrasting to pre-transitional MC flows, the vorticity and drop organization depend on the initial gas temperature, this being due to the drop/turbulence coupling. The vapor-composition mean molar mass and standard deviation distributions strongly correlate with the initial liquid-composition PDF; such a correlation only exists for the magnitude of the mean but not for that of the standard deviation. Unlike in pre-transitional situations, regions of large composition standard deviation no longer necessarily coincide with regions of large mean molar mass. The kinetic energy, rotational and composition characteristics, and dissipation are liquid specific and the variation among liquids is amplified with increasing free-stream gas temperature. Eulerian and Lagrangian statistics of gas-phase quantities show that the different observation framework may affect the perception of the flow characteristics. The gas composition, of which the first four moments are calculated, is shown to be close to, but distinct from a SGPDF. The PDF of the scalar dissipation rate is calculated for drop-laden layers and is shown to depart more significantly from the typically assumed Gaussian in gaseous flows than experimentally measured gaseous scalar dissipation rates, this being attributed to the increased heterogeneity due to drop/flow interactions.

1. Introduction

Turbulent flows laden with drops of liquid containing a multitude of chemical species occur both in nature and in industrial processes. An example of the former is the ocean spray formed when waves break up, and an example of the latter is spray painting (automobiles, wood, etc.). When ocean water drops are transported by wind into the atmosphere, differential evaporation of the chemical species leads to the eventual formation of a solid particle, which, when entrained in the upper atmosphere can bias the interpretation of satellite data. During spray painting, there is a delicate balance between the very volatile components that evaporate before the liquid drops arrive to the substrate, and the other components that eventually reach the substrate; thus, the paint formulation must take into account the physics occurring in the time lag between the paint release and its arrival at the target surface. In both of these examples, the fate of the liquid composition evolution is governed by the interaction between turbulence and the drops.

There is a very substantial body of literature – too many papers to be cited – devoted to the study of single-component (SC) species drops in turbulent flows. Also, there have been numerous studies of single drops of liquid composed of a small number of species, dating back to the landmark binary-species model proposed by Landis & Mills (1974). Emulating Landis & Mills (1974), a large number of investigations are available (some of these studies consider many drops in turbulent flows) that consider a relatively small number (e.g. up to 10) of species in the liquid compared to the composition of liquids that are of interest in many applications. For example, petroleum fuels, which are used to power most of the transportation systems in the world, are composed of hundreds of species, some of

which upon vaporization are instrumental in ignition, others which during combustion are responsible for pollutant production, and yet others which upon vaporization condense on walls and contribute to corrosion. Some of these species may be present in the liquid in minute concentrations, yet their importance may be totally disproportionate to their concentration. Thus, while valuable results were obtained from modeling studies of SC-liquid drops and small-number-of-species liquid drops in turbulent flows, the reality of MC-liquid drop interaction with turbulence has not been explored by those studies. It is only recently that the physical understanding of multicomponent-species (MC) drops in turbulent flows has been addressed through modeling and simulations.

Realizing the impossibility of accounting for each individual species as an element of a discrete set, a statistical approach has recently been developed -- a methodology which is much more attuned to large ensembles of variables. All MC-liquid statistical approaches have been based on Continuous Thermodynamics (CT) concepts. The CT theory, developed by Gal-Or, Cullinan & Galli (1975) and Cotterman, Bender & Prausnitz (1985), includes an appropriate representation of the chemical potential for a mixture containing numerous components and involves a derivation of the Gibbs function through molecular thermodynamic methods in terms of the probability distribution function (PDF) describing the mixture composition. The concepts are fundamental and independent of the physicochemical model chosen for the chemical potential. From a specified initial composition PDF, the evolution of the mixture is determined by the physics of the situation encapsulated into thermodynamic relationships and/or conservation equations. Although the composition PDF generally depends on many variables, it can be tailored to depend on one or a restricted number of variables that govern the phenomena under consideration. Examples of such choices are those of Cotterman, Bender & Prausnitz (1985), Whitson (1983), Rätzsch & Kehlen (1983), Chou & Prausnitz (1986) where it

was shown, with validation, that the single-Gamma PDF (SGPDF) depending on the molar mass, m, can represent an entire homologous species class of hydrocarbons. The normal boiling point, T_b, has been shown by Harstad (2005) to be a good choice in a CT study focussing on atmospheric hydrocarbon partitioning. Cotterman, Bender & Prausnitz (1985) have used thermodynamic relations to show that during evaporation, the same mathematical form of the PDF applies in the gas phase as in the liquid from where the vapor originates. The flexibility of the CT approach in terms of the PDF mathematical form and of the choice of the PDF variable(s) makes it attractive for a variety of studies.

Tamim & Hallett (1995) and Hallett (2000) have pioneered the application of CT concepts to the study of a MC-liquid drop. Their model has been adopted by Lippert & Reitz (1997) in practical simulations of spray combustors and by Le Clercq & Bellan (2004) in a direct numerical simulation (DNS) of a transitional mixing layer having a lower stream initially laden with a large number (e.g. $O(10^6)$) of drops. The Tamim & Hallett (1995) and Hallett (2000) model has also constituted the point of departure for the development of models with increasing range of application (Harstad, Le Clercq & Bellan (2003), Arias-Zugasti & Rosner (2003), Harstad & Bellan (2004)). Specifically, Harstad, Le Clercq & Bellan (2003) have shown that the Tamim & Hallett (1995) and Hallett (2000) model based on representing the liquid composition by a single-Gamma PDF (SGPDF) depending on m, while appropriate for slow evaporation in fuel-unvitiated surroundings, cannot describe even qualitatively evaporation under high-temperature or in fuel-vitiated conditions. Instead, a double-Gamma PDF (DGPDF) has been proposed, which exercised for single drops compared excellently for most conditions with the results from a discrete-species model based on a 32-species representation. The flexibility of the statistical representation was manifested once more in the DGPDF model of Harstad &

Bellan (2004) that was shown to fit all three preponderant homologous classes of Jet A, RP-1 and JP-7 petroleum fuels with only a single DGPDF when the PDF dependence is chosen to be on $m^{0.5}$ instead of m.

The recent pre-transitional DGPDF DNS study of Le Clercq & Bellan (2005) enlarged the SGPDF study of Le Clercq & Bellan (2004) for the same mixing layer configuration. The advantage of the DGPDF representation is that a regime of higher evaporation can be attained and thus that the results may have increased relevance to the realistic high-temperature regime of combustors, which averred impossible with either SC-liquids or with the SGPDF MC-liquid representation. Notable results obtained by Le Clercq & Bellan (2005) were the development of a DGPDF liquid composition from an initially-specified SGPDF, the liquid-specific development of the vortical flow field and vorticity magnitude, and the vapor ('vapor' is here defined as the ensemble of species evolving from the drops through evaporation) composition which was directly traced to the initial liquid composition.

Compared to the transitional SGPDF DNS study of Le Clercq & Bellan (2004) and to the pre-transitional DGPDF DNS study of Le Clercq & Bellan (2005), the present DNS investigation accesses a higher-temperature turbulent-gas regime that is closer to that of real combustors, despite the fact that the initial gas temperature, T_0 (the subscript 0 denotes the initial condition), is still very much lower than in combustors. This lower T_0 value is dictated by the requirement to match the drop characteristic time to that of the flow, which in this transitional regime is much larger than that of fully turbulent flows, which are inaccessible in DNS. The focus of this study is on the effect of the drop/flow interaction which exists only as long as the drop has not entirely evaporated. Thus, the interaction characteristic time is influenced by the liquid volatility, the initial drop size, the initial gas composition, the relative difference between T_0 and the initial drop tem-

perature $T_{d,0}$, and the relative difference between $T_{d,0}$ and the liquid boiling temperature which for MC-liquid drops evolves with time as the liquid composition changes. Not only are the present results necessary to understand the coupled interaction of evaporating MC-liquid drops with a flow exhibiting turbulence features, but such a database has the potential of being further used for *a priori* and *a posteriori* studies similar to those of Okong'o & Bellan (2004) and Leboissetier, Okong'o & Bellan (2005). To aid the unified understanding of MC turbulent flows, simulations are here performed both for single-phase (SP) MC flows, where the effect of the initial Reynolds number, Re_0, is investigated, and for two-phase (TP) MC flows where the effect of the initial mass loading, ML_0, and higher T_0 are explored with the same model (whereas in Le Clercq & Bellan (2004), using a SGPDF, only the ML_0 effect was investigated and in Le Clercq & Bellan (2005), using a DGPDF, only the T_0 influence was studied).

As stated above, this investigation is conducted within the framework of the DNS methodology wherein all scales of the flow are resolved. Originally devised for SP flows, DNS for TP flows with particles that are much smaller than the Kolmogorov scale and which have a volumetrically small loading ($\lesssim 10^{-3}$) was enabled by the results of Boivin, Simonin & Squires (1998) who showed that the drops can be treated as point sources of mass, momentum and energy from the gas-phase perspective. It is thus appropriate to perform TP simulations using a gas-phase resolution that is adequate for SP flow by following the gas phase in an Eulerian frame and tracking the drops in a Lagrangian frame. The terminology DNS, while not strictly accurate, is traditionally applied to such simulations, and several recent studies have used this DNS methodology (Boivin, Simonin & Squires (1998), Mashayek (1998a), Mashayek (1998b), Mashayek & Jaberi (1999), Réveillon & Vervisch (2000), Okong'o & Bellan (2004)).

This paper is organized as follows: In §2 the conservation equations are briefly re-

called from the detailed model developed by Le Clercq & Bellan (2005). Section §3 is devoted to the description of the configuration, the boundary and initial conditions, and then of the results. These results encompass global layer characteristics, flow visualizations, homogeneous-plane statistics, analysis of the irreversible entropy production including the PDF of the scalar dissipation, and an examination the vapor-composition PDF mathematical form away from drop surfaces. Comparisons with the SC DNS study of Okong'o & Bellan (2004) and with the pre-transitional DNS investigation of Le Clercq & Bellan (2005) are also discussed. The results are summarized in §4 and future study directions are discussed.

2. Conservation equations

The model of Le Clercq & Bellan (2005) is adopted wherein the MC liquid and gas compositions are described by

$$P(m;\alpha_1,\beta_1,\alpha_2,\beta_2,\varepsilon) = (1-\varepsilon)f_\Gamma^{(1)} + \varepsilon f_\Gamma^{(2)}, \tag{2.1}$$

where $f_\Gamma^{(k)} = f_\Gamma(m;\alpha_k,\beta_k)$ with integer $k = 1, 2$, ε is a weighting parameter ($0 \leqslant \varepsilon \leqslant 1$), $\int_\gamma^\infty P(m)dm = 1$ and

$$f_\Gamma(m) = \frac{(m-\gamma)^{\alpha-1}}{\beta^\alpha \Gamma(\alpha)} \exp\left[-\left(\frac{m-\gamma}{\beta}\right)\right] \tag{2.2}$$

where $\Gamma(\alpha)$ is the Gamma function and $f_\Gamma(m)$ is a SGPDF. The origin of f is specified by γ (we naturally assume that $\gamma_1 = \gamma_2 = \gamma$), and its shape is determined by α and β. At each time t, $P(m;\alpha_1,\beta_1,\alpha_2,\beta_2,\varepsilon)$ is determined by the vector $\eta \equiv (\alpha_1,\beta_1,\alpha_2,\beta_2,\varepsilon)$. According to Harstad, Le Clercq & Bellan (2003), P can be determined by an inverse mapping from its first four moments, ξ_n where integer $n \in [1,4]$, with a fifth parameter empirically calculated. These moments are defined as

$$\xi_{nl} \equiv \int_\gamma^\infty m^n P_l(m)dm, \;\; \xi_{nv} \equiv \int_\gamma^\infty m^n P_v(m)dm, \tag{2.3}$$

for integer $n \geqslant 1$, where subscripts l and v denote the liquid and vapor, respectively. At each t, P_l describes the liquid-fuel composition, which is specific of each drop, and P_v describes the vapor composition, which varies with spatial location. Throughout this paper we adopt the notation $\theta \equiv \xi_1$ and $\psi \equiv \xi_2$, and the standard deviation of P is calculated as $\sigma = \sqrt{(\psi - \theta^2)}$. Also following Harstad, Le Clercq & Bellan (2003), one can define ξ_n^{SGPDF} as being the moments of a SGPDF that would have the same ξ_1 and ξ_2 values as a specified P. Thus, 'excess moments' of any PDF P with respect to the SGPDF that has the same θ and ψ as P are defined by

$$\xi_n' \equiv \xi_n - \xi_n^{SGPDF}. \tag{2.4}$$

By definition $\xi_1' = \xi_2' = 0$ and a DGPDF then corresponds to $\xi_n' \neq 0$ for $n \geqslant 3$. Thus, the deviation of any PDF from the equivalent SGPDF decreases with decreasing (ξ_n'/ξ_n^{SGPDF}).

The conservation equations derived in Le Clercq & Bellan (2005) are succinctly recalled below.

2.1. *Gas phase equations*

The gas is followed in an Eulerian frame and the generic conservation equations for continuity, momentum, energy, species and DGPDF first four moments $(\theta_v, \psi_v, \xi_{3v}, \xi_{4v})$ representing the composition are

$$\frac{\partial \Phi}{\partial t} + \frac{\partial \left[\Phi u_j\right]}{\partial x_j} = \frac{\partial \left[\Psi(\Phi)\right]}{\partial x_j} + S, \tag{2.5}$$

where

$$\Phi = \{c, cmu_i, cme_t, cX_v, cX_v\theta_v, cX_v\psi_v, cX_v\xi_{3v}, cX_v\xi_{4v}\} \tag{2.6}$$

is the vector of the conservative variables,

$$\Psi(\Phi) = \{cm\mathcal{D}\frac{\partial}{\partial x_j}\left[\frac{X_v}{m}\left(1-\frac{\theta_v}{m_a}\right)\right], \; -p\delta_{ij}+\sigma_{ij},$$
$$-pu_j + u_i\sigma_{ij} + \lambda\frac{\partial T}{\partial x_j} + \alpha_1(T)\frac{\partial}{\partial x_j}\left(\frac{X_v}{m}\right) + \alpha_2(T)\frac{\partial}{\partial x_j}\left(\frac{X_v\theta_v}{m}\right) + \alpha_3\frac{\partial}{\partial x_j}\left(\frac{X_v\psi_v}{m}\right),$$
$$cm\mathcal{D}\frac{\partial}{\partial x_j}\left(\frac{X_v}{m}\right), cm\mathcal{D}\frac{\partial}{\partial x_j}\left(\frac{X_v\theta_v}{m}\right), cm\mathcal{D}\frac{\partial}{\partial x_j}\left(\frac{X_v\psi_v}{m}\right), cm\mathcal{D}\frac{\partial}{\partial x_j}\left(\frac{X_v\xi_{3v}}{m}\right),$$
$$cm\mathcal{D}\frac{\partial}{\partial x_j}\left(\frac{X_v\xi_{4v}}{m}\right)\} \tag{2.7}$$

is the diffusional flux vector corresponding to Φ, and

$$S = \{S_{\text{mole}}, S_{\text{mom},i}, S_{\text{en}}, S_{\text{mole}}, S_{\text{mass}}, S_\psi, S_{\xi_3}, S_{\xi_4}\} \tag{2.8}$$

is the source term vector of components S_r associated with Φ. In (2.5)-(2.7) c is the molar density, x_i is the i^{th} spatial coordinate, $\mathbf{u}$ is the mass-averaged velocity, X is the mole fraction, $m = \theta_v X_v + m_a(1-X_v)$ is the molar mass where m_a is the carrier gas molar mass (subscript a denotes the carrier gas), $\mathcal{D}$ is an effective diffusion coefficient defined by Harstad & Bellan (2004) as the proportionality coefficient between the vapor mass flux and $cm\nabla(X_v/m)$, p is the pressure, σ_{ij} is the viscous stress tensor, δ_{ij} is the Kronecker symbol, $e_t = e_k + e_{int} = u_iu_i/2 + h - p/\rho$ is the total energy of the gas, $\rho = mc$ is the mass density, h is the enthalpy, λ is the thermal conductivity and T is the gas temperature. The last three terms in the heat flux of the energy equation are the portion due to transport of species by the molar fluxes; the detailed expressions for $\alpha_1(T), \alpha_2(T)$ and α_3 are presented in Appendix A. The source vector arises from the coupled interaction of drops and gas, and is presented in §2.3.

The perfect gas equation of state

$$p = (\rho R_u T)/m = cR_uT \tag{2.9}$$

where R_u is the universal gas constant, closes the system of gas-phase equations.

2.2. *Drop equations*

Each drop is individually simulated and the liquid mass-density, ρ_l, is assumed constant although the liquid molar-density, c_l, may vary. Because $\rho/\rho_l = O(10^{-3})$, the gas phase is quasi-steady with respect to the liquid phase (Williams (1965)), and due to the relatively small value of T_0 compared to that in combustors, the evaporation rate is relatively low (verified in Le Clercq & Bellan (2005)) so that the assumption of uniform internal drop properties is justified. The Lagrangian conservation equations for each drop position χ, velocity $\mathbf{v}$, energy, mass $M_d = V_d\rho_l = \pi\rho_l D^3/6$ (V and D represent volume and diameter, and the subscript d denotes the drop), and composition are

$$\frac{d\chi_i}{dt} = v_i, \quad \frac{dv_i}{dt} = \frac{F_i}{M_d}, \tag{2.10}$$

$$M_d C_l \frac{dT_d}{dt} = \underbrace{\frac{\lambda Nu}{D}\frac{\ln(1+B_T)}{B_T} A\,(T - T_d)}_{Q_{\text{conv-diff}}} + \underbrace{\dot{m}_d \frac{L_{veff}}{B}}_{Q_{\text{evap}}}, \tag{2.11}$$

$$\dot{m}_d \equiv \frac{dM_d}{dt} = -\frac{Sh}{3\text{Sc}}\frac{M_d}{\tau_d}\ln(1+B), \tag{2.12}$$

$$\frac{d\xi_{nl}}{dt} = \frac{3\theta_l}{2BD^2}\frac{dD^2}{dt}\{[\frac{X_v}{m} - \frac{X_v^{(s)}}{m^{(s)}}(1+B)]\xi_{nl} + \frac{X_v^{(s)}\xi_{nv}^{(s)}}{m^{(s)}}(1+B) - \frac{X_v\xi_{nv}}{m}\} \tag{2.13}$$

for integer $n = [1, 4]$, where the gas phase at the drop location, interpolated from the Eulerian solution, acts as the drop far field. $F_i = (M_d/\tau_d)\, f_1\,(u_i - v_i)$ where $\tau_d = \rho_l D^2/(18\mu)$ is the particle time constant for Stokes flow; T_d is the drop temperature; C_l is the liquid heat capacity at constant pressure; $A = \pi D^2$ is the drop-surface area; μ is the viscosity of the carrier gas; $\text{Pr} = \mu C_p/(\lambda m)$, where C_p is the gas heat capacity at constant pressure, and $Sc = \mu/(\rho\mathcal{D})$ are the Prandtl and the Schmidt numbers respectively; and $\rho_l = c_l\theta_l$. The Nusselt, Nu, and the Sherwood, Sh, numbers are semi-empirically modified using the Ranz-Marshall correlations, accounting for convective heat and mass transfer effects (Miller & Bellan (1999)), with the similarity assumption $Nu = 2 + 0.552\ \text{Re}_{sl}^{1/2}\,(\text{Pr})^{1/3}$, $Sh = 2 + 0.552\ \text{Re}_{sl}^{1/2}\,(Sc)^{1/3}$. f_1, given in Miller & Bellan

(1999),

$$f_1 = \frac{1 + 0.0545\,\mathrm{Re}_{sl} + 0.1\,\mathrm{Re}_{sl}^{1/2}\,(1 - 0.03\,\mathrm{Re}_{sl})}{1 + a\,|\mathrm{Re}_b|^b}, \tag{2.14}$$

$$a = 0.09 + 0.077\exp(-0.4\,\mathrm{Re}_{sl}), \qquad b = 0.4 + 0.77\exp(-0.04\,\mathrm{Re}_{sl}) \tag{2.15}$$

is an empirical correction to Stokes drag accounting for finite drop Reynolds numbers using the slip Reynolds number $\mathrm{Re}_{sl} = |\mathbf{u}_{sl}|\,\rho D/\mu$ where $\mathbf{u}_{sl} = (\mathbf{u} - \mathbf{v})$ is the slip velocity, and for a Reynolds number $\mathrm{Re}_b = U_b \rho d/\mu$ based on the evaporation blowing velocity U_b obtained from the mass conservation relation at the drop surface, $\dot{m}_d = -\pi\rho D^2 U_b$. The correlation of (2.14) is valid in the ranges $0 \leqslant \mathrm{Re}_{sl} \leqslant 100$ and $0 \leqslant \mathrm{Re}_b \leqslant 10$. $B = (Y_v^{(s)} - Y_v)/(1 - Y_v^{(s)})$ is the Spalding number, where $Y_v = X_v \theta_v / m$ is the vapor mass fraction, $Y_a = 1 - Y_v$, and $(1 + B_T) = (1 + B)^{1/Le}$ with Le being the Lewis number, L_{veff} is an effective latent heat (Harstad, Le Clercq & Bellan (2003)) as defined in Appendix A of Le Clercq & Bellan (2005), and the superscript (s) denotes the drop surface. At this surface, the classical boundary conditions of temperature equality, and mass, species, momentum and energy flux conservation apply (Williams (1965)). Under the ideal-mixture assumption, Raoult's law relates the drop and gas PDFs

$$P_v^{(s)} = \frac{p_{atm}}{X_v^{(s)} p} \exp\left[\frac{m L_v(m)}{R_u T_b(m)}\left(1 - \frac{T_b(m)}{T_d}\right)\right] P_l^{(s)}, \tag{2.16}$$

where $p_{atm} = 1atm$ and $L_v(m)$ and $T_b(m)$ are the latent heat and the normal boiling point, correlated as functions of m by Harstad, Le Clercq & Bellan (2003) using Trouton's law,

$$\Delta s_{\mathrm{lg}} = m L_v / T_b \simeq 10.6 R_u, \tag{2.17}$$

and

$$T_b(m) = A_b + B_b m, \tag{2.18}$$

where $A_b = 241.4$ and $B_b = 1.45$ for T_b in K (see Appendix A of Le Clercq & Bellan (2005) for more details).

2.3. *Source terms*

The source-term-vector components of (2.8) are

$$S_\tau = -\sum_{q=1}^{N} \frac{w_q}{\Delta V_q}[\Lambda_\tau]_q, \tag{2.19}$$

$$\Lambda = \{\frac{d\mathcal{N}}{dt},\ F_j + \frac{d(\mathcal{N}\theta_l)}{dt}v_j,\ v_j F_j + Q_{\text{conv-diff}} + Q_{\text{evap}} + \dot{m}_d\left(\frac{v_j v_j}{2} + C_l T_d\right),$$
$$\frac{d\mathcal{N}}{dt},\ \frac{d(\mathcal{N}\theta_l)}{dt},\ \frac{d(\mathcal{N}\psi_l)}{dt},\ \frac{d(\mathcal{N}\xi_{3l})}{dt},\ \frac{d(\mathcal{N}\xi_{4l})}{dt}\} \tag{2.20}$$

where $\mathcal{N} = M_d/\theta_l$ is the number of moles in the drop, N is the number of drops, and the summation in (2.19) is over all drops residing within a local numerical discretization volume, ΔV_q. Following previous methodology (Miller & Bellan (1999), Okong'o & Bellan (2004) and Le Clercq & Bellan (2005)), a geometric weighting factor w_q distributes the individual drop contributions to the nearest eight grid points in proportion to their distance from the drop location. Le Clercq & Bellan (2004) explained that because convective effects dominate the species flux term, for MC flows, differential species diffusivity is negligible in transport from the drop location to the grid nodes. Because numerical diffusion induced by distributing the Lagrangian source terms at the Eulerian nodes is proportional to $V_d/\Delta V_q$, this potential effect is here negligible since this ratio is initially $O(10^{-3})$ (see §3.1) and decreases with t as the drops evaporate.

3. Results

3.1. *Configuration, boundary and initial conditions, and numerics*

The three-dimensional (3D) mixing layer configuration is displayed in figure 1 where the coordinates (x_1, x_2, x_3) correspond to the streamwise, cross-stream and spanwise directions, respectively. The velocity difference across the layer is $\Delta U_0 = 2U_0$ and its mathematical form is prescribed using an error-function profile (Miller & Bellan (1999)) having a width given by the initial vorticity thickness $\delta_{\omega,0} = \Delta U_0/\langle\partial u_1/\partial x_2\rangle$ ($\langle\rangle$ denotes

averaging over homogeneous (x_1, x_3) planes). A perturbation is imposed on the vorticity field to promote roll-up and pairing (Moser & Rogers (1991), Miller & Bellan (1999), Miller & Bellan (2000)). The forcing wavelengths in the x_1 and x_3 directions are l_1 and l_3, and their amplitudes with respect to the circulation are 10% and 2.25%, respectively. The evolution of the layer comprises two pairings of the four initial spanwise vortices to form an ultimate vortex in which small scales may proliferate if the Reynolds number is high enough. The dimensions of the domain are $L_1 = 4l_1 (= 29.16\delta_{\omega,0} = 0.2$ m), $L_2 = 1.1L_1$, and $L_3 = 4l_3 = 0.6L_1$.

The gas-phase initial condition is specified by six parameters: T_0; the free-stream pressure p_0; $\mathrm{Re}_0 = \rho_{a,0}\Delta U_0 \delta_{\omega,0}/\mu$, where $\rho_{a,0}$ is the initial carrier gas (air) mass-density and μ is calculated from the specified value of Re_0; the Mach number $M_{c,0}$ based on the carrier gas initial speed of sound $a_{a,0} = \sqrt{R_a T_0 C_{p,a}/C_{v,a}}$ where $R_a = R_u/m_a$ and the specific heats of the carrier ($C_{p,a}$ and $C_{v,a}$) are computed as in Miller, Harstad & Bellan (1998); the vapor molar fractions in the lower stream, $X^l_{v,0}$, and upper stream, $X^u_{v,0}$, here specified $X^l_{v,0} = X^u_{v,0} = 10^{-4}$ for all TP simulations (this non-null value is realistic in that it simulates drop evaporation in vitiated air, as occurs in engines); and the specification of the free-stream vapor composition, which for each liquid is found from a single-drop simulation in air at the specified T_0 by choosing it to be the first-time-step surface-vapor composition. For SP simulations, either $X^l_{v,0} = X^u_{v,0}$, in which case there is no mass flux between streams, or $X^l_{v,0} = 10^{-1}$ so as to create a vapor mass flux between the two streams; the value of 10^{-1} approximately corresponds to the average lower-stream value encountered at transitional states in TP simulations. The free-stream velocity $U_0 = M_{c,0}a_{a,0}$ is calculated from the specified value of $M_{c,0}$. The thermal conductivity and diffusivity (both constant) are computed using the value of μ and specified values of $\mathrm{Pr} = Sc$, 0.696 at $T_0 = 375$ K and 0.694 at $T_0 = 400$ K, calculated as in Miller,

Harstad & Bellan (1998). The vapor heat capacity at constant pressure, $C_{p,v}$ is calculated as in Appendix A of Le Clercq & Bellan (2005). Table 1 lists all initial conditions and defines a baseline simulation; additional to the $\mathrm{Re}_0 = 500$ and 600 simulations performed here, the table also lists some Le Clercq & Bellan (2005) $\mathrm{Re}_0 = 200$ computation conditions, as the present results will be compared to those of the listed pre-transitional simulations. The initial mass loading, ML_0, defined as the ratio of the initial liquid mass to that of the gas in the lower stream, is null for SP simulations and $0 < ML_0 < 1$ for TP simulations. For TP computations, the $\mathrm{Re}_0 = 500$ simulations were close to the limit of the memory capacity of the computational platform (the $ML_0 = 0.5$ simulation was almost at the memory limit), preventing TP simulations at higher Re_0.

In the TP simulations, initially only the lower stream of the mixing layer ($x_2 < 0$) is laden with drops, which are randomly distributed with a uniform number density and have at $t = 0$ a null slip velocity with respect to the gas. The mean drop number density profile is smoothed near the center-line, $x_2 = 0$, using an error-function profile. The initial conditions for the drops are specified by: $T_{d,0}$ which is uniform, with $T_{d,0} < T_0$ and a selected value of $(T_0 - T_{d,0})$ to ensure that the drop/flow interaction is captured over the entire layer evolution with a substantial number of drops remaining in the simulation at all times (for the chosen $T_{d,0} = 345$ K, these conditions were conservatively satisfied for all liquids when $T_0 = 375$ K and 400 K as shown in §3.4); ML_0; the Stokes number St_0, where $St \equiv \tau_d \Delta U_0 / \delta_{\omega,0}$; ρ_l; and the liquid composition shown in figure 2, obtained through the selected-PDF moments. Le Clercq & Bellan (2005) emphasize that it is not possible to initialize all computations with the same values of the total number of drops, N_0, since ρ_l does not have the same value for all liquids and μ changes with T_0. Following the well accepted methodology of comparing simulations performed with specified non-dimensional numbers rather than physical quantities (Batchelor (1967)),

the specification of ML_0 and St_0 determines for given ρ_l and T_0 the value of N_0 and D_0 (see table 1). The initial Stokes number is specified through a Gaussian distribution with mean $\{\{St_0\}\} = 3$ and standard deviation $\sqrt{\{\{St_0^2\}\} - \{\{St_0\}\}^2} = 0.5$ where $\{\{\}\}$ symbolizes drop-ensemble averages over all drops. Similarly to the study of Le Clercq & Bellan (2005), four fuels are considered as practically-significant examples of liquids – diesel, Jet A, RP-1 and JP-7 – whose initial composition (Edwards & Maurice (2001)), provided as a mole fraction versus the carbon number by Edwards (2002) was fitted in PDF form by Harstad & Bellan (2004). Table 1 lists the mean and standard deviation of the initial liquid PDF, $P_{l,0}$, which is assumed to be a SGPDF to enable the examination of the potential deviation from its initial SGPDF form.

The boundary conditions in the x_1 and x_3 directions are periodic, and adiabatic slip-wall conditions in the x_2 direction previously derived (Poinsot & Lele (1992), Baum, Poinsot & Lele (1994)) were adapted by Le Clercq & Bellan (2005) to the DGPDF CT model for MC mixtures (see Appendix B of Le Clercq & Bellan (2005)). Drops reaching the slip walls are assumed to stick to them and are otherwise followed using the drop equations of §2.2.

The equations displayed in §2.1 were solved using an eighth-order central finite difference discretization in space and a fourth-order Runge-Kutta for temporal advancement. To mitigate potential numerical instabilities for long CPU time simulations, following Kennedy & Carpenter (1994), a tenth-order filtering for spatial derivatives was used (except in a half-filter-size band located at the lower and upper x_2 boundaries) at every time step. This filtering introduces a small amount of dissipation that serves only to stabilize the computations for long-time integrations, but since it acts only on the shortest waves that can be resolved on the grid, it does not act as a turbulence model and thus does not allow under-resolved computations (see Okong'o & Bellan (2004)). The time

step was controlled by the CFL number. The grid size is listed in table 1 and scales approximately linearly with Re_0 (see Tennekes & Lumley (1972)). The grid resolution is approximately 10^{-3} m, 0.55×10^{-3} m and 0.46×10^{-3} m when $\mathrm{Re}_0 = 200, 500$ and 600, respectively. The $\sim 10^{-3}$ value of $\{\{V_{d0}\}\}/\Delta V_q$ (computed using the values of $\{\{D_0\}\}$ in table 1) ensures that numerical diffusion induced by distributing the Lagrangian source terms at the Eulerian nodes is negligible. A fourth-order Lagrange interpolation, $\mathcal{I}$, was used to obtain gas-phase variable values at drop locations. Drops whose mass decreased below 3% of the initial mass $M_{d,0}$ were removed from the calculation; for the conditions of this study, few drops fell below 3% of $M_{d,0}$ (at the two extremes are diesel simulations, where no drops disappeared, and RP-1 at $T_0 = 400$ K, where 9.8% of drops disappeared by transition) and mass was conserved in the system to a maximum relative error of 5×10^{-5}.

3.2. *Global layer evolution*

3.2.1. *Growth and dynamics*

Figure 3 illustrates the global growth, mixing and rotational characteristics of the layers. Growth is measured by the momentum thickness, δ_m

$$\delta_m = \frac{\int_{x_2,\min}^{x_2,\max} \left[\langle\rho u_1\rangle_{x_2,\max} - \langle\rho u_1\rangle\right]\left[\langle\rho u_1\rangle - \langle\rho u_1\rangle_{x_2,\min}\right] dx_2}{\left(\langle\rho u_1\rangle_{x_2,\max} - \langle\rho u_1\rangle_{x_2,\min}\right)^2} \tag{3.1}$$

plotted versus $t^* \equiv t\Delta U_0/\delta_{\omega,0}$, where $x_{2,\max} = L_2/2$ and $x_{2,\min} = -L_2/2$ are the lower and upper boundaries of the computational domain. The overall variation of $\delta_m/\delta_{\omega,0}$ is typical of mixing layers with a roll-up region ($t^* < 20$), and two regions of rapid increase ($20 \leqslant t^* \leqslant 50$ and $65 \leqslant t^* \leqslant 95$) each ending by a plateau corresponding to a pairing. Comparing simulations with different values of ML_0 in figure 3a, $\delta_m/\delta_{\omega,0}$ peaks at $t^* = 98$ for $ML_0 = 0$ (unless otherwise stated, the $ML_0 = 0$ simulations considered are those with $X^l_{v,0} = 10^{-1}$ so as to approach as close as possible the $ML_0 \neq 0$ simulations

in terms of species mass transfer) independent of Re_0, at $t^* = 103$ for all $ML_0 = 0.2$ computations, and at $t^* = 106$ for the $ML_0 = 0.5$ simulation. The delay of the second pairing with increasing ML_0 is explained by the increasing total mass that must be entrained as the layer grows. For all $ML_0 = 0.2$ computations shown in figure 3b, $\delta_m/\delta_{\omega,0}$ peaks at $t^* = 103$ showing independence of liquid composition; similarly, there seems to be independence of T_0 (figure 3a and information not shown). The $\delta_m/\delta_{\omega,0}$ peak does not necessarily correspond to the transition time, t^*_{tr}, defined as that occurring when the energy spectra (discussed below) first exhibit classical turbulence characteristics. In table 2, t^*_{tr} and $\mathrm{Re}_{m,tr}$ are listed where $\mathrm{Re}_m \equiv \mathrm{Re}_0\,\delta_m/\delta_{\omega,0}$. Tested only for SP computations, the value of $\mathrm{Re}_{m,tr}$ increases nearly proportionally with Re_0 . The $\mathrm{Re}_{m,tr}$ value increases with ML_0 up to $ML_0 = 0.2$, and decreases from $ML_0 = 0.2$ to $ML_0 = 0.5$, which was also found by Okong'o & Bellan (2004) for SC-liquid drop-laden transitional mixing layers and was attributed to the initial forcing that has a relatively weaker influence on the highest ML_0 value layers; that is, SP flows do not behave merely as a simple limit of TP flows. Although a small variation, at $T_0 = 375$ K the value of $\mathrm{Re}_{m,tr}$ increases with increasing mean liquid molar mass, which is attributed to the decreased liquid volatility and consequently to the larger residual drop mass that promotes turbulence through drop/flow interactions (see §3.5). At $T_0 = 400$ K, the three kerosenes have similar $\mathrm{Re}_{m,tr}$ values, which are distinctively smaller than that for diesel, showing that liquid-specificity effects increase with larger T_0. Therefore, the growth of the layer seems insensitive, but the global transitional characteristics seem mildly sensitive, to the liquid identity.

Because the gas phase mass, M_G, can only increase due to vapor addition, the plot of $M_G/M_{G,0}$ in figures 3c and 3d gives a direct measure of global mass evolution. Expectably, no change in the initial amount of vapor occurs when $ML_0 = 0$, but either an increase in ML_0 or in T_0 results in an augmentation in $M_G/M_{G,0}$, as shown in figure 3c. The major

augmentation occurs before roll-up, after which $M_G/M_{G,0}$ increases more gradually and at generally similar rates for all diesel simulations, independent of ML_0 or T_0 values. However, the augmentation in $M_G/M_{G,0}$ occurs during the early part before roll-up for the larger ML_0 and during the late part before roll-up at the higher T_0, and is a much stronger function of T_0 than of ML_0. The strongest parameter influencing $M_G/M_{G,0}$ is though the fuel composition, as depicted in figure 3d. Compared to diesel, the more volatile kerosenes evaporate at a much larger rate during roll-up, and they continue to increase the vapor in the gas phase at a slightly higher rate than diesel even during the remaining layer evolution.

Figures 3e - 3h display the rotational characteristics of the layer: the positive spanwise vorticity, $\langle\langle\omega_3^+\rangle\rangle\,\delta_{\omega,0}/\Delta U_0$, which is initially null and measures the small-scale activity, in figures 3e and 3f and the enstrophy, $\langle\langle\omega_i\omega_i\rangle\rangle\,(\delta_{\omega,0}/\Delta U_0)^2$, which is related to stretching and tilting and represents an important mechanism for turbulence production (see Chorin (1991)), in figures 3g and 3h; $\langle\langle\rangle\rangle$ denotes averaging over all grid points. The results show that the variation with Re_0 and ML_0 of both $\langle\langle\omega_3^+\rangle\rangle\,\delta_{\omega,0}/\Delta U_0$ and $\langle\langle\omega_i\omega_i\rangle\rangle\,(\delta_{\omega,0}/\Delta U_0)^2$ emulates the SC-liquid results discussed in detail by Okong'o & Bellan (2004): For $\langle\langle\omega_3^+\rangle\rangle\,\delta_{\omega,0}/\Delta U_0$ the time of the major peak seems independent of Re_0 for the SP layers; the peak is delayed with increasing ML_0 indicating the well-known stabilizing effect of small drops on a flow; and the value at the peak increases with Re_0 and ML_0, this being attributed to the enhanced small-scale formation at larger Reynolds numbers and the increased source of vorticity represented by a larger liquid mass (S_{mom} represents a source term in the vorticity equation), respectively. For all simulations, $\langle\langle\omega_i\omega_i\rangle\rangle\,\delta_{\omega,0}/\Delta U_0$ exhibits a peak earlier than $\langle\langle\omega_3^+\rangle\rangle\,\delta_{\omega,0}/\Delta U_0$, similar to the observations Okong'o & Bellan (2004). Variation of the enstrophy from its initial value is associated with the classical energy cascade that, unlike in two-dimensional flows, occurs

in 3D flows (Chorin (1991)), and thus the $\langle\langle\omega_i\omega_i\rangle\rangle\,\delta_{\omega,0}/\Delta U_0$ relative magnitude with respect to the initial conditions is directly associated with the strength of the energy cascade. Viewed in this perspective, the fact that for the same initial conditions both SC SP and SC TP results of Okong'o & Bellan (2004) (their figure 3h) display a similar magnitude $\langle\langle\omega_i\omega_i\rangle\rangle\,\delta_{\omega,0}/\Delta U_0$ peak to the corresponding MC SP and MC TP simulation means that the energy cascade is of similar strength for SC and MC flows. Whether for $\langle\langle\omega_3^+\rangle\rangle\,\delta_{\omega,0}/\Delta U_0$ in figures 3e and 3f or for $\langle\langle\omega_i\omega_i\rangle\rangle\,(\delta_{\omega,0}/\Delta U_0)^2$ in figures 3g and 3h, T_0 and the liquid composition seem to have negligible effect on the global rotational characteristics.

The peculiarities of energy transfer among scales in MC flows (of which the stretching and tilting activity is only one manifestation) are manifested in the energy spectra depicted in figure 4 at t^*_{lr}. Both the streamwise spectra in figure 4a and the spanwise spectra in figure 4b, shown as an example for u_1 and for selected simulations, exhibit a smooth behavior characteristic of turbulence (the peak observed in figure 4b is at the forcing frequency) and no accumulation of energy at the smallest scales, which indicates excellent spatial resolution. At same Re_0, SP spectra have less energy in a given wavenumber than TP flows, which is attributed to their reduced vortical characteristics at t^*_{lr}. Compared to SP spectra, of particular interest is the enhanced energy in the TP spanwise spectra at the smallest wavenumber, portraying the increased vortical features of TP flows resulting from the source terms in the vorticity equations. The fact that at the smallest scale TP flows have more than two orders of magnitude more energy than SP flows is due to reasons discussed in §3.5. Increasing Re_0 produces a SP flow with an increased range of large wavenumbers, as expected, while increasing ML_0 increases the energy at the smaller wavenumbers and imperceptibly decreases the energy at the largest wavenumbers indicating a larger dissipation, a fact confirmed by the dissipation budget

analysis of §3.5. There is no sensitivity to T_0 and to the fuel composition. Compared to the TP SC results of Okong'o & Bellan (2004) (their figure 2), the energy in the highest wavenumbers is here reduced by a factor of 10^5 in the streamwise direction and by a factor of more than 10^4 in the spanwise direction suggesting that because the energy cascade is of similar strength in SC and MC flows, the viscous dissipation must be larger in TP MC flows, which is confirmed in §3.5.

The kinetic energy of the flow, $E_{kG} = \int_{\text{domain}} \rho\,(u_i u_i/2)\,dV$, is illustrated in figure 5 as a fraction of its initial value. Insensitive to the Re_0 magnitude, the fraction of SP-flow kinetic energy slowly decays up to the end of roll-up (figure 5a), after which the rate of decay accelerates and by transition only about 80% of the kinetic energy remains in the system, the balance of 20% having been dissipated by the evolved small scales. In TP flows, the fraction of kinetic energy slightly (less than 4%) augments during the early roll-up, culminates, after which it monotonically decreases. Increasing ML_0 or T_0 promotes an initial augmentation of the kinetic energy, and for ML_0 it eventually leads to a larger decay at t^*_{tr}, while for T_0 the opposite is observed. The different variation with ML_0 and T_0 is consistent in that in the former case the liquid mass, ML, is larger with respect to the baseline case during the simulation, whereas in the latter case ML is smaller due to the larger evaporation. Liquid composition effects are shown in figure 5b and are seen to be as strong as the ML_0 or T_0 effects. With increasing liquid volatility, the fraction of kinetic energy increases, emulating the increased T_0 effect of figure 5a, and the rate of decay is slightly reduced, consistent with the dissipation budget shown in §3.5. At $T_0 = 375$ K the effect is small, and similar plots at $T_0 = 400$ K in figure 5b exhibit a slightly larger difference between liquids, which indicates that at larger T_0 the liquid-specific effects are enhanced.

3.2.2. *Drop characteristics*

Shown in figure 6 are mixing-layer Lagrangian ensemble averages portraying the evolution of the drop characteristics in that portion of the domain. The lower (upper) stream is defined as the region in which $\langle u_1 \rangle \leqslant -0.99U_0$ ($\langle u_1 \rangle \geqslant 0.99U_0$), and the mixing layer, which is the complement of the free-stream domain, is the region where $-0.99U_0 > \langle u_1 \rangle > 0.99U_0$. Ensemble averages over the mixing layer are here of interest because it is that site which hosts most of the interaction between drops and a flow with turbulent characteristics; comparisons with the simulations of Le Clercq & Bellan (2005) where the flow was pre-transitional should reveal the effect of drop/turbulence interactions.

We define net evaporation as corresponding to a decrease in M_d, or equivalently $\dot{m}_d < 0$ or since ρ_l is assumed constant a decrease in D; net condensation corresponds to the reverse variation of these variables. Each of net evaporation and net condensation encompass concomitant evaporation of some species and condensation of other species. Figures 6a and 6b portray $\{\{T_d\}\}_{ml}/T_{d,0}$ and $\{\{D^2\}\}_{ml}/\{\{D_0^2\}\}$ where the subscript ml denotes the mixing layer. $\{\{T_d\}\}_{ml}/T_{d,0}$ varies only slightly, by at most a few % from $T_{d,0}$, and exhibits the undulatory behavior identified by Le Clercq & Bellan (2004) and Le Clercq & Bellan (2005) to originate in the cooling and heating cycles experienced by the drops. Up to the first pairing, there is practically no difference between the present simulations and those of Le Clercq & Bellan (2005), however, past that station $\{\{T_d\}\}_{ml}/T_{d,0}$ is here larger, which is a manifestation of the enhanced mixing due to turbulence that promotes drop heating. At the higher T_0, the drop heating is dominated between roll-up and first pairing by the total number of drops, resulting in a larger $\{\{T_d\}\}_{ml}/T_{d,0}$ for $\mathrm{Re}_0 = 200$ (fewer drops), whereas past the first pairing the enhanced turbulent heating governs, leading to a larger $\{\{T_d\}\}_{ml}/T_{d,0}$ for $\mathrm{Re}_0 = 500$. Jet A being

the liquid containing the most volatile species, the corresponding drops experience the largest initial cooling resulting from the early evaporation, with further drop heating. RP-1 and JP-7, having relatively less-volatile species than Jet A and narrow compositions, exhibit only modest cooling followed by heating, and the slightly more volatile species in RP-1 lead to a slightly increased cooling with respect to JP-7. A larger ML_0 manifests in an enhanced drop cooling which rivals for diesel at $ML_0 = 0.5$ the cooling experienced by Jet A. For all liquids, the small variations in $\{\{T_d\}\}_{ml}/T_{d,0}$ though translate in considerably larger variations in $\{\{D^2\}\}_{ml}/\left\{\left\{D_0^2\right\}\right\}$, with the rapid initial temperature change corresponding to the steepest decrease in the drop size, which subsides by the end of roll-up. An intermediary rate of evaporation follows which abates by the middle of the second pairing, upon reaching a very gradual drop reduction. The non-constant rate of $\{\{D^2\}\}_{ml}/\left\{\left\{D_0^2\right\}\right\}$ decay is a mark of the ensemble averaging, as each individual drop obeys the classical D^2-law (Harstad, Le Clercq & Bellan (2003)). On going from pre-transitional to transitional flow results, one notes an eventual reduction in $\{\{D^2\}\}_{ml}/\left\{\left\{D_0^2\right\}\right\}$ by $\sim 5\%$ (V_d by $\sim 11\%$). Kerosene drops reach by the end of the simulation $\sim 46\%$ of $V_{d,0}$ compared to diesel's $\sim 63\%$, and an increase in mass loading of a factor of 2.5 leads to a factor of ~ 1.7 increase in V_d by the end of the computation. Clearly, within the range of parameters investigated, the fuel identity is the most prominent factor influencing the drop size evolution.

Companion plots of $\{\{\theta_l\}\}_{ml}/\theta_{l,0}$ and $\{\{\sigma_l\}\}_{ml}/\sigma_{l,0}$ are displayed in figures 6c and 6d. As in results portraying entire-domain ensemble averages from simulations of Le Clercq & Bellan (2005), the initial $\{\{\theta_l\}\}_{ml}/\theta_{l,0}$ surge is accompanied by a drastic reduction in $\{\{\sigma_l\}\}_{ml}/\sigma_{l,0}$ as the most volatile species evaporate, thus reducing the number of species in the drop. Eventually $\{\{\sigma_l\}\}_{ml}/\sigma_{l,0}$ reaches a minimum which coincides with a tapering off in the augmentation of $\{\{\theta_l\}\}_{ml}/\theta_{l,0}$. The interaction of drops with the flow

promotes evaporation/condensation, and thus enhances changes in both $\{\{\theta_l\}\}_{ml}/\theta_{l,0}$ and $\{\{\sigma_l\}\}_{ml}/\sigma_{l,0}$. The augmentation in $\{\{\sigma_l\}\}_{ml}/\sigma_{l,0}$ indicates that condensation occurs, with a local plateau evident by the end of the first pairing; the concomitant increase in $\{\{\theta_l\}\}_{ml}/\theta_{l,0}$ indicates than on an ensemble basis evaporation is more effective than condensation in determining the mean liquid molar mass. Up to the first pairing there is no sensitivity to Re_0, however, once small scales become preponderant (figure 3g and 3h) one can detect not only quantitative but also qualitative differences between the pre-transitional and transitional results; although $\{\{\theta_l\}\}_{ml}/\theta_{l,0}$ continues to increase in both cases, being larger in the latter situation, $\{\{\sigma_l\}\}_{ml}/\sigma_{l,0}$ for transitional computations reaches a minimum, then increases, and eventually crosses over the ever increasing $\{\{\sigma_l\}\}_{ml}/\sigma_{l,0}$ at $\mathrm{Re}_0 = 200$. The decrease in $\{\{\sigma_l\}\}_{ml}/\sigma_{l,0}$ corresponds to a narrower DG-PDF, and represents the accelerated release of species due to the drop/turbulence interaction. Eventually, the species evaporation becomes limited by the value of T_d while species condensation again augments $\{\{\sigma_l\}\}_{ml}/\sigma_{l,0}$. The lack of $\{\{\theta_l\}\}_{ml}/\theta_{l,0}$ and $\{\{\sigma_l\}\}_{ml}/\sigma_{l,0}$ variation in tandem as a function of Re_0 means that the pre-transitional simulations do not merely represent an intermediary state to the transitional results because not only is the mean molar mass here larger, but the entire composition distribution is different due to the simultaneous evaporation and condensation of different species promoted by the turbulent flow transporting drops to various sites of the layer. For all liquids at the baseline conditions, $\{\{\theta_l\}\}_{ml}/\theta_{l,0}$ continuously increases with t^* as evaporation depletes increasingly less volatile species, but the rate of augmentation is not uniform even after the initial surge. This nonuniform rate is consistent with the non-monotonic evolution of $\{\{\sigma_l\}\}_{ml}/\sigma_{l,0}$ representing evaporation when it decreases and condensation when it increases. At the larger ML_0, $\{\{\theta_l\}\}_{ml}/\theta_{l,0}$ no longer increases monotonically and instead experiences a minimum about half-way through the first pairing while $\{\{\sigma_l\}\}_{ml}/\sigma_{l,0}$ dis-

plays a maximum at the first pairing; that is, the reduction in T_d at the larger ML_0 results in decreasing evaporation which combined with the condensation of the lighter species reduces the mean molar mass and further increases the width of the composition distribution. Clearly, as ML_0 increases, evaporation becomes governed by limitations in drop heat up rather than by the drop/turbulence interaction. At the larger T_0, the larger (smaller) $\{\{\theta_l\}\}_{ml}/\theta_{l,0}$ for $\mathrm{Re}_0 = 200$ than for $\mathrm{Re}_0 = 500$ between roll-up and first pairing (after the first pairing) corresponds to the higher (lower) $\{\{T_d\}\}_{ml}/T_{d,0}$.

Noteworthy, except for the liquids with the most narrow composition PDF (i.e. RP-1 and JP-7), $\{\{\sigma_l\}\}_{ml}/\sigma_{l,0}$ does not exceed unity. That is, drops of liquids with a narrower composition are more prone to larger changes in the width of their composition distribution as each condensing species onto a drop makes a larger impact on the composition of the liquid drop. When the liquid composition has a PDF with a larger width, evaporation of species of ever decreasing volatility dominates the condensation of the lighter species within the time span of these simulations, resulting in a reduced composition heterogeneity.

3.2.3. *Vapor composition characteristics*

The effect of Re_0 and ML_0 on the vapor composition is illustrated in figures 7a and 7c, and the influence of liquid identity and T_0 is depicted in figures 7b and 7d. Paralleling the drop ensembles averages of figure 6, the volumetric averages of figure 7 are also over the mixing layer portion of the domain. Noteworthy, the simulation provides only the first four moments of the vapor composition, but not the mathematical form of its PDF. Indeed, consistent with the calculation of the source terms at grid nodes, the vapor-composition PDF is at each node the sum, according to equation 2.19, of all vapor PDFs at the drop surface for drops located within the grid volume associated with the specified node. The summation of DGPDFs having different values of same-order moments is not

necessarily a DGPDF. Only the first two moments of the composition are examined in figure 7. The PDF representation of the vapor composition, including the higher moments, is addressed in §3.6.

For diesel, independent of the initial conditions, $\langle\langle\theta_v\rangle\rangle_{ml}/\theta_{v,0}$ experiences a sustained growth from unity, initially representing the combined effect of condensation of lighter species onto drops, as obvious from by the sharp decay in $\langle\langle\sigma_v\rangle\rangle_{ml}/\sigma_{v,0}$, and of species heavier than $\theta_{v,0}$ that may have been released through drop evaporation. Further increase in $\langle\langle\theta_v\rangle\rangle_{ml}/\theta_{v,0}$ is accompanied by an augmentation in $\langle\langle\sigma_v\rangle\rangle_{ml}/\sigma_{v,0}$, showing that although evaporation of some species occurs concomitantly with condensation of other species, during the remaining of the simulation it is species addition from the liquid phase that dominates the changes in the vapor composition. In contrast, the kerosenes experience immediate increase in $\langle\langle\theta_v\rangle\rangle_{ml}/\theta_{v,0}$ due to evaporation, as $\langle\langle\sigma_v\rangle\rangle_{ml}/\sigma_{v,0}$ simultaneously increases. Compared to a change in Re_0 by a factor of 2.5, a change by the same factor in ML_0 produces a much larger effect on $\langle\langle\theta_v\rangle\rangle_{ml}/\theta_{v,0}$ and $\langle\langle\sigma_v\rangle\rangle_{ml}/\sigma_{v,0}$. The much reduced $\langle\langle\theta_v\rangle\rangle_{ml}/\theta_{v,0}$ obtained when $ML_0 = 0.5$ results from the increased condensation detected in figure 7c, reflecting drop-heating relative impediments, and is consistent with the lower $\{\{T_d\}\}_{ml}/T_{d,0}$ in figure 6a. The larger initial decay experienced by $\langle\langle\sigma_v\rangle\rangle_{ml}/\sigma_{v,0}$ at the lower Re_0 (figure 7c) shows that relative to the higher Re_0 a larger number of species condenses and because the condensing species have a smaller molar mass, this process produces a higher $\langle\langle\theta_v\rangle\rangle_{ml}/\theta_{v,0}$ from roll-up to the first pairing (figure 7a). Past the first pairing, the larger $\{\{T_d\}\}_{ml}/T_{d,0}$ at the higher Re_0 (figure 6a) leads to increasing evaporation versus condensation which augments $\langle\langle\sigma_v\rangle\rangle_{ml}/\sigma_{v,0}$ and elevates $\langle\langle\theta_v\rangle\rangle_{ml}/\theta_{v,0}$ through the addition of higher molar mass species.

Mirroring the drop composition characteristics, changes in the vapor composition are smallest for the narrowest composition-PDF kerosenes for which the vapor mean molar

mass increases (figure 7b) owing to net evaporation (figure 7d); T_0 has only a very modest effect as the species thermodynamics are quite similar for the narrow compositions. Although initial net evaporation also increases $\langle\langle\theta_v\rangle\rangle_{ml}/\theta_{v,0}$ for Jet A, its much wider composition PDF leads to a correspondingly greater T_0 impact. Finally, as already discussed, diesel is distinct from all other liquids in that the augmentation of $\langle\langle\theta_v\rangle\rangle_{ml}/\theta_{v,0}$ is initially due to condensation of lighter vapor species onto the drops and also to evaporation of heavier species from the drops, and its much wider composition PDF makes it prone to the largest influence of T_0. Noteworthy, the value of $\langle\langle\theta_v\rangle\rangle/\theta_{v,0}$ has a theoretical maximum limit corresponding to complete drop evaporation. Neglecting the initial amount of vapor (which here represents less than 0.53 % of the total liquid mass), if all liquid were evaporated, the composition of the vapor would be that of the liquid at $t^* = 0$, that is, $\max(\langle\langle\theta_v\rangle\rangle/\theta_{v,0}) = \theta_{l,0}/\theta_{v,0}$. From table 1 one finds that $\theta_{l,0}/\theta_{v,0}$ is 1.32 for diesel, 1.23 for Jet A, 1.076 for RP-1 and 1.087 for JP-7. The departure of $\langle\langle\theta_v\rangle\rangle/\theta_{v,0}$ from these asymptotic limits depends on the amount of vapor already released. The impact of T_0 is only on the evaporation rate, and thus on the time needed to reach this asymptotic value. Consequently, the bunching in figure 7b of $\langle\langle\theta_v\rangle\rangle/\theta_{v,0}$ for RP-1 and JP-7 is consistent with their similar values of $\theta_{l,0}/\theta_{v,0}$ and evaporation rates (figure 6b), and curves for Jet A and diesel match by happenstance as a result of the competing effects between the significantly higher asymptotic limit for diesel and the much higher evaporation rate for Jet A (figure 6b). These considerations are independent of the actual composition of the initial vapor; however, because the initial vapor is here found from a single-drop simulation in air at the specified T_0 (by choosing it to be the first-time-step surface-vapor composition,) this means that $\theta_{v,0}$ depends on $\theta_{l,0}$ through the width of the liquid-PDF, finally explaining why RP-1 and JP-7 on the one hand and diesel and Jet A on the other hand show similar $\langle\langle\theta_v\rangle\rangle/\theta_{v,0}$.

Clearly, averaged quantities can only give a general physical picture of the flow, and detailed visualizations, presented next, are necessary to understand the details of the situation.

3.3. *Flow visualizations*

3.3.1. *Drop field*

The detailed distribution of the drop number density, ρ_n, calculated as an Eulerian field from the Lagrangian distribution

$$\rho_n = \sum_{q=1}^{N_d} \frac{w_q}{\Delta V_q} \tag{3.2}$$

is presented in figure 8. The plots depict the between-the-braid plane $x_3/L_3 = 0.5$ for selected simulations, each at t^*_{ir}. All simulations display an intricate drop organization exhibiting a multitude of scales. The void regions correspond to locations of high vorticity (Squires & Eaton (1991)) and contain no drops as the ρ_n value based on one drop per computational volume leads to $\rho_n = 5.9 \times 10^9$ m^{-3}. The outline of the void regions corresponds to high-strain locations (Squires & Eaton (1991); also see §3.4.1) and displays large concentrations of drops.

Increasing ML_0 (figures 8a and 8c) leads to a more intricate drop organization exhibiting a larger range of scales; this is because at same St_0 value the larger N_0 induces more drop/flow interaction which amplifies local non-uniformities through the drag action. The larger ML_0 leads expectably to higher ρ_n values.

With increasing T_0, diesel (figures 8a and 8b) and JP-7 (figures 8g and 8h) exhibit more heterogeneity in the lower stream and part of the mixing layer, with void regions which now punctuate the rather uniform ρ_n lower stream. These new regions of small ρ_n result from the enhanced drop heating which promotes evaporation. No such regions are detected for Jet A (figures 8e and 8f) within the range of displayed ρ_n, although

structural changes with increasing T_0 are clearly visible. This dependency of the drop organization as a function of T_0 should be contrasted with the insensitivity to T_0 found in the pre-transitional simulations of Le Clercq & Bellan (2005). It is thus clear that the coupling between turbulence and drops creates this T_0 dependency.

Composition effects, examined at both $T_0 = 375$ K (figures 8a, 8e and 8g) and 400 K (figures 8b, 8d, 8e and 8h) show that the complexity of the drop organization decreases with increased fuel volatility, indicating that by reducing the drop size and thus the local drop/flow drag force, early evaporation has a homogenizing effect on the ρ_n structure. Because at $T_0 = 400$ K all kerosenes have the same N_0 and $\{\{D_0\}\}$ (see table 1), the different ρ_n distributions portrayed in figures 8b, 8d, 8e and 8h result solely from the different liquid composition. The global structural organization for RP-1 and JP-7 (which have similar composition PDFs) at same initial conditions is virtually identical, although local differences in the structure of the field and value of ρ_n are visible.

Additional insight into the relationship between the drop position, its temperature and its composition is achieved by examining Lagrangian visualizations displayed for the baseline case in figure 9 at $t^*_{l_T}$ in the mixing layer portion of the domain; each sphere in the plot represents a physical drop, the drops are magnified for readability and there is no relationship between a drop size and its plotted volume. Due to the viewing angle, the void regions evident in figure 8 are obscured. The lower part of the mixing layer is populated by low-T_d drops (figure 9a), but as the drops penetrate further into the mixing layer, they heat up and form temperature-wise a very heterogeneous drop ensemble. The largest T_d is achieved by drops located at the top of the ultimate vortex, as they are in contact with the upper stream carrier gas at T_0. The impact of T_d on θ_l is evident in figure 9b. Both the drop history and its instantaneous T_d determine the value of θ_l, as not all drops within a given temperature range have the same composition. The drops

with the smallest θ_l are located in the lower part of the mixing layer, and their θ_l is noticeably higher than $\theta_{l,0}$ owing to the already evaporated volatiles. The mixing layer contains drops with a great variety of compositions and the composition diversity is also obvious in the remnant of the initial four spanwise vortices; a quantitative measure of the heterogeneous distribution is presented in §3.4.1. Drops having $\theta_l > 245$ kg/kmol are primarily located at the top of the ultimate vortex. However, not all drops at that location have $\theta_l > 245$ kg/kmol, as most drops have there 235 kg/kmol $< \theta_l < 245$ kg/kmol. Moreover, some drops with 235 kg/kmol $< \theta_l < 245$ kg/kmol are also found embedded deep in the lower part of the ultimate vortex. This substantial local variation in θ_l is premonitory of what could be expected for θ_v.

3.3.2. *Flow field*

Dynamics

To differentiate between SP and TP simulations, the between-the-braid plane $\omega_3\delta_{\omega,0}/\Delta U_0$ is first displayed in figure 10 for all $ML_0 = 0$ computations. In all cases, the complex structure of the flow is apparent with regions of negative values, as in the initial condition, interspersed with regions of substantial positive values which are a manifestation of the developed small-scale activity. The maximum $\omega_3\delta_{\omega,0}/\Delta U_0$ value increases with Re_0, as expected, and decreases with increasing $(X^l_{v,0} - X^u_{v,0})$, which is attributed at this point to the correspondingly increasing scalar dissipation, a fact confirmed in §3.5. The increased scalar dissipation contributes to the larger dissipation and due to the coupling of the dynamics with scalar transport, the viscous dissipation whose role is the reduction of organized motion also increases (see §3.5), which decreases the vorticity.

The $ML_0 \neq 0$ spanwise vorticity is illustrated in figure 11 for the same simulations shown in figure 8. The maximum $\omega_3\delta_{\omega,0}/\Delta U_0$ value increases with increasing ML_0 when going from null to non-null values (compare with figure 10a) but the opposite occurs

when ML_0 changes from 0.2 to 0.5, and instead concentrated regions of high vorticity appear, conjectured to result from the amplified local interaction of the larger size drops (figure 6b) with the flow. The value of T_0 has considerably more impact than ML_0 in determining the $\omega_3\delta_{\omega,0}/\Delta U_0$ activity and its maximum value. Although for diesel, JP-7 and RP-1 the larger T_0 increases the maximum $\omega_3\delta_{\omega,0}/\Delta U_0$, the opposite occurs for Jet A. This liquid-specific behavior is explained by the variation of the source magnitude, $\nabla\times(\frac{1}{\rho}\mathbf{S}_{\mathrm{mom}}) = \nabla\times\left\{\frac{1}{\rho}\left[\mathbf{F}+\frac{d(\mathcal{N}\theta_l)}{dt}\mathbf{v}\right]\right\}$, in the vorticity equation. Evidently, this source contains two terms: the drag, which is positive and decreases with the decreasing drop size promoted by the increasing T_0, and the momentum of the vapor released from the drops which is negative and increases in absolute value with increasing T_0. In the ω_3 equation, this term is $\left(\frac{\partial(S_{\mathrm{mom},1}/\rho)}{\partial x_2}-\frac{\partial(S_{\mathrm{mom},2}/\rho)}{\partial x_1}\right)$ meaning that it is not only the sign of each of the two contributions that is important, but also their spatial variation that influences the sign of the source term. Although a direct relationship between liquid volatility and the sign of the source term is not immediately apparent, we note that for a very volatile liquid such as Jet A, $[\nabla\times(\frac{1}{\rho}\mathbf{S}_{\mathrm{mom}})]_3$ evidently becomes smaller with increasing T_0, whereas for a relatively much less volatile liquid, such as diesel, the vorticity source term becomes larger with increasing T_0. Because JP-7 and RP-1 follow the diesel trend, what seems to be the determining factor in this variation is the lightest species entering the composition of the liquid (see figure 2) rather than the width of the composition PDF. This T_0 effect on the vortical activity should be contrasted to the insensitivity observed in the pre-transitional simulations of Le Clercq & Bellan (2005), indicating that this aspect is intimately related to the turbulence production through the drop/flow interaction.

Thermodynamics

The Y_v contours are shown in figure 12 for the same simulations illustrated in figure 8. The heterogeneity of the vapor distribution is noteworthy in all cases, with the larger

values generally confined to the lower stream. As either T_0 or ML_0 increase (figures 12a, 12b and 12c), the maximum Y_v increases, but this effect is a much stronger function of T_0 than of ML_0 because an augmentation in T_0 promotes single-drop evaporation through enhanced heat transfer, whereas the opposite happens at a more elevated ML_0 due to limitations on heat transfer from a gas phase with a fixed amount of heat. The larger maximum Y_v at $ML_0 = 0.5$ compared to $ML_0 = 0.2$ is thus a consequence of N_0 which affects $N\dot{m}$. Examination of the Y_v field structure shows increased heterogeneity with increasing T_0 or ML_0, with regions of the largest Y_v penetrating well into the mixing layer and reaching its boundary adjacent to the upper stream while pockets of negligible Y_v embedding deep into the mixing layer. Concomitantly, regions of low Y_v are now present as isolated pockets in the lower stream. At fixed T_0 and ML_0, the maximum Y_v increases with increasing fuel volatility, while the structural complexity of the Y_v field decreases, which is attributed to the earlier evaporation that allows substantial small-scale mixing before the achievement of transition.

To entirely characterize the vapor, composition contours are displayed for θ_v in figure 13 and for σ_v in figure 14 corresponding to the simulations presented in figure 12. Compared to the pre-transitional results of Le Clercq & Bellan (2005), the θ_v contours are considerably more heterogeneous, with multiple locations of very high values throughout the mixing layer. With increasing T_0, the maximum value of θ_v increases (figures 13a and 13b; figures 13g and 13h) due to the evaporation of the heavier components; the opposite occurs when ML_0 increases (figures 13a and 13c) due to the limitation in heat transfer which prevents the release of heavier components. Generally, the range of θ_v values mirrors that in the initial liquid composition (figure 2) in that a narrow initial PDF range translates into a narrow range of θ_v values. For a narrower initial PDF having a larger-m component as its most volatile species (e.g. JP-7, for which $\gamma = 93$ kg/kmol,

shown in figure 13g relative to diesel, for which $\gamma = 86$ kg/kmol, shown in figure 13a), the lower stream is uniquely composed of very light species due to the larger time lag necessary for the drops to reach a T_d value at which evaporation may proceed (not visible at the reduced number of contour levels shown); at the more elevated ML_0, θ_v is in the lower stream also smaller (not detectable on the contour levels of figures 13a and 13c), this being attributed to the lower T_d which hinders evaporation of relatively less volatile species. The very close association between initial liquid composition and the magnitude and distribution of θ_v is best highlighted when examining figures 13d and 13h representing RP-1 and JP-7 at same conditions: their almost coincidental PDFs of figure 2 results in virtually the same contour distribution and magnitude. Whether at $T_0 = 375$ K (figures 13a, 13e and 13g) or at $T_0 = 400$ K (figures 13b, 13d, 13f and 13h), the heterogeneity of the θ_v distribution increases with decreasing PDF width.

Parallel contour plots of σ_v add more details to the information on the vapor composition. For all simulations, σ_v displays a complex distribution with generally small values in either stream, and intermediate and high values confined to the mixing layer. Notable exceptions are the baseline diesel simulation (figure 14a) and that with $ML_0 = 0.5$ (figure 14c) where the upper stream exhibits larger σ_v than the lower stream (only detectable in equivalent color plots, not shown), this being a manifestation of the lower stream condensation rather than implying that the upper stream is heterogeneous. Whereas in the pre-transitional study of Le Clercq & Bellan (2005) the locations of maximum θ_v and σ_v entirely coincided, here this is no longer the case. Although the intersection of the maximum-value θ_v and σ_v locations is not null in corresponding plots of figures 13 and 14, there is a considerable number of locations of maximum θ_v value that do not correspond to a location of maximum σ_v value, and vice versa. After substantial evaporation, when only the heavier species remain in a drop, the evolved turbulence is responsible for trans-

porting that drop in regions where the vapor composition may be relatively uniform, and thus the local drop evaporation will result in a location of large θ_v but relatively small σ_v (e.g. figures 13a, 13e and 13g compared to 14a, 14e and 14g, respectively). Conversely, drops at intermediary stages of evaporation may be brought by turbulence in a region of strong composition non-uniformity, thereby creating through evaporation a location of intermediary θ_v values and high σ_v values (i.e. figure 13f compared to 14f). Scrutiny of figures 14d and 14f makes it clear that, unlike for θ_v, here there is no longer as strong a relationship between the initial liquid-composition PDF and the σ_v magnitude, although the qualitative aspect and the relative structure of the σ_v distribution are still closely related to this PDF. Increasing T_0 (figures 14a and 14b; 14e and 14f; 14g and 14h) results in the maximum σ_v increasing, and this effect is stronger with decreased fuel volatility (diesel versus all kerosenes) because this promotes the release of an increasing range of heavier components from drops, as seen when comparing figures 13a and 13b.

The general picture that emerges is that of the importance of drop/turbulent-flow interaction and initial liquid-composition PDF in determining the vapor distribution and local composition. Both T_0 and ML_0 couple non-linearly with that interaction and with the initial liquid-composition PDF.

3.4. *Liquid and vapor first-order statistics*

3.4.1. *Statistics related to the drops*

Thermodynamics

Figure 15 displays the homogeneous (x_1, x_3) plane average number of drops, N_{x_2}, at t^*_{tr}. For a specified x_2, the value of N_{x_2} represents the number of drops in the region $(x_2 - \Delta x_2/2, x_2 + \Delta x_2/2)$. Clearly, for $ML_0 = 0.2$, in the lower stream (qualitatively meaning here $x_2/\delta_{\omega,0} < -10$) and in the mixing layer (qualitatively meaning here $-10 \leqslant x_2/\delta_{\omega,0} < 7$) there is a very large number of drops, and thus all drop statistics performed

at these locations are meaningful. With increasing $x_2/\delta_{\omega,0}$ beyond $x_2/\delta_{\omega,0} = 7$, the quality of the statistics deteriorates. For $ML_0 = 0.5$, the number of drops in the lower stream increases proportionally to the ML_0 augmentation and in the mixing layer, despite the local (with $x_2/\delta_{\omega,0}$) fluctuations, the number of drops remains proportional.

Statistics over a specified drop ensemble may be of interest either for drop-defined quantities, in which case the concept is straightforward, or for gas-defined quantities interpolated at the drop locations, in which case it represents the drop's far field value. From a gas-defined quantity, A, interpolated through $\mathcal{I}$ to drop locations, resulting in the quantity $A^{\mathcal{I}}$, three types of drop ensemble averages can be defined as shown in table 3. For example, ρ_n can be interpolated to the drop locations to obtain $\rho_n^{\mathcal{I}}$, and one can further calculate the number of drops per computational cell (i.e. inside ΔV_q), $n_c \equiv [\rho_n^{\mathcal{I}}]_c = \rho_n^{\mathcal{I}} \times \Delta V_q$, where $\Delta V_q = \Delta x_1 \times \Delta x_2 \times \Delta x_3$ is the cell volume defined in § 2.3. Drop ensemble averages of n_c, T_d, θ_l and σ_l and their standard deviations are presented in figure 16.

Despite the large number of drops in the lower stream, $\{n_c\} < 1$ ($\{\}$ defined in table 3) for all simulations (for readability, only a restricted selection of simulations is shown in figure 16a). In the mixing layer, $\{n_c\} < 1.5$ for $ML_0 = 0.2$ and $\{n_c\} \lesssim 2$ for $ML_0 = 0.5$, showing again the consistency of our assumptions regarding the volumetric loading past the initial condition, particularly since $\{\{V_d\}\}/\{\{V_{d,0}\}\}$ has considerably decreased from unity, as conservatively indicated by $\{\{D^2\}\}_{ml}/\{\{D_0^2\}\}$ in figure 6b, the mixing layer region being that where both $\{n_c\}$ and the standard deviation, $(\{n_c^2\} - \{n_c\}^2)^{0.5}$ shown in figure 16b, are largest; the same result prevails for $x_2/\delta_{\omega,0} > 7$, although the statistics are not considered converged.

For all simulations at $ML_0 = 0.2$ and $T_0 = 375$ K, $\{T_d\}/T_{d,0}$ decreases in the lower stream from its initial value (figure 16c) and this reduction is by happenstance similar

for diesel, RP-1 and JP-7, while for Jet A, the most volatile liquid, slightly smaller values are obtained. This reduction is due to the immediate evaporation of the most volatile species, and since Jet A contains more-volatile species than each of the other liquids (figure 2), the decrease in $\{T_d\}/T_{d,0}$ is largest. Expectably, with increasing T_0, $\{T_d\}/T_{d,0}$ is larger and even exceeds unity at $T_0 = 400$ K, indicating that heat transfer to the drops combined with condensation more than compensates for that lost from evaporation ($\{\sigma_l\}/\sigma_{l,0} < 1$ in figure 16g). Conversely, when $ML_0 = 0.5$, $\{T_d\}/T_{d,0}$ is further depressed due to the same heat now being available for an increased number of drops. ML_0 trends similar to the lower stream are observed throughout the mixing layer, with the important difference that in this region of high drop/flow interaction, with increasing $x_2/\delta_{\omega,0}$ there is increasing coincidence among all kerosenes, which is attributed to the similar species in the three kerosenes once the very volatile ones have been released, that is, to the coincidence of the high-m region for Jet A, RP-1 and JP-7 (figure 2). With increasing $x_2/\delta_{\omega,0}$ beyond the lower stream, and for $T_0 = 400$ K, $\{T_d\}/T_{d,0}$ augments at a higher rate than at $T_0 = 375$ K, this being explained by the hotter air entrained into the mixing layer from the upper stream, which promotes drop heating. Whereas $(\{T_d^2\} - \{T_d\}^2)^{0.5}/T_{d,0}$ is minimal in the lower stream (figure 16d), in the mixing layer it abruptly increases by approximately a factor of 10, indicating the great $\{T_d\}/T_{d,0}$ variability of conditions in this region of high drop/turbulence interaction; the plateau-like value exhibited by the standard deviation across the entire mixing layer is indicative of nearly uniform variability. The least $\{T_d\}/T_{d,0}$ variability occurs for RP-1 and JP-7, portraying their narrow composition, followed by diesel and Jet A which have wider PDFs. The $\{T_d\}/T_{d,0}$ variability declines with increasing ML_0 and augments with higher T_0, being a direct consequence of the reduced/increased availability of heat for each drop in the layer.

The drop composition statistics are illustrated in figures 16e and 16f for $\theta_l/\theta_{l,0}$ and in figures 16g and 16h for $\sigma_l/\sigma_{l,0}$. The lower stream is characterized by a uniform $\{\theta_l\}/\theta_{l,0} > 1$, resulting from the early evaporation of the most volatile species, with the largest values reached by diesel and Jet A that contain more volatile species than RP-1 and JP-7. However, while $\{\sigma_l\}/\sigma_{l,0} < 1$ for diesel and Jet A, indicative of evaporation, $\{\sigma_l\}/\sigma_{l,0} > 1$ for RP-1 and JP-7 indicative of condensation, both with respect to the initial condition. Increasing ML_0 or T_0 has opposite effects on $\{\theta_l\}/\theta_{l,0}$ in that it decreases/increases its value, portraying reduced/enhanced evaporation with respect to the baseline case, whereas it has a qualitatively similar, increasing effect on $\{\sigma_l\}/\sigma_{l,0}$ with the influence of ML_0 being much weaker. It is clear that within the restricted parametric range investigated, ML_0 has in the lower stream a much stronger influence on $\{\theta_l\}/\theta_{l,0}$ than on $\{\sigma_l\}/\sigma_{l,0}$, while the opposite is true for T_0. Both $(\{\theta_l^2\} - \{\theta_l\}^2)^{0.5}/\theta_{l,0}$ and $(\{\sigma_l^2\} - \{\sigma_l\}^2)^{0.5}/\sigma_{l,0}$ are minimal within the lower stream, consistent with the low level of heterogeneity encountered in this region. At $ML_0 = 0.2$ and $T_0 = 375$ K, proceeding into the mixing layer, $\{\theta_l\}/\theta_{l,0}$ augments with $x_2/\delta_{\omega,0}$ at a larger rate for diesel and Jet A than for the other two kerosenes, which is evidence of increased evaporation of the most volatile species in diesel and Jet A that are not part of the RP-1 and JP-7 compositions. In contrast to the $\{\theta_l\}/\theta_{l,0}$ variation, for $\{\sigma_l\}/\sigma_{l,0}$ two distinct behaviors are apparent: RP-1 and JP-7, which have the narrower compositions, have experienced increasing condensation in the lower part of the mixing layer (i.e. $\{\sigma_l\}/\sigma_{l,0} > 1$ and increases) with $x_2/\delta_{\omega,0}$, followed by reduced condensation (i.e. $\{\sigma_l\}/\sigma_{l,0} > 1$ and decreases) with $x_2/\delta_{\omega,0}$, and finally by evaporation in the upper part of the mixing layer (i.e. $\{\sigma_l\}/\sigma_{l,0} < 1$ and decreases) with $x_2/\delta_{\omega,0}$, whereas for diesel and Jet A globally evaporation has occurred (i.e. $\{\sigma_l\}/\sigma_{l,0} < 1$) which was enhanced (i.e. $\{\sigma_l\}/\sigma_{l,0}$ decreases) with increasing $x_2/\delta_{\omega,0}$. The non-monotonic behavior for the narrower PDF kerosenes is

conjectured to result from a combination of the smaller T_d value in the lower part of the mixing layer and of entrainment into this region of the very volatile species that have evaporated early into the lower stream and are here encountering favorable conditions for condensation; while both evaporation and condensation may concomitantly occur for diesel and Jet A, the larger separation in saturation pressure between the early evaporated species residing in the lower stream and the intermediate species released in the mixing layer leads to a larger loss of species through evaporation. Neither a change of value in ML_0 nor in T_0 results in qualitative changes in the variation of $\{\theta_l\}/\theta_{l,0}$ and $\{\sigma_l\}/\sigma_{l,0}$ with $x_2/\delta_{\omega,0}$, and even the quantitative rate of augmentation trends remain for $\{\theta_l\}/\theta_{l,0}$. However, $\{\sigma_l\}/\sigma_{l,0}$ exhibits a stronger decay at the higher T_0, indicative of stronger evaporation, whereas the opposite occurs at the larger ML_0. The larger $(\{\theta_l^2\} - \{\theta_l\}^2)^{0.5}/\theta_{l,0}$ and $(\{\sigma_l^2\} - \{\sigma_l\}^2)^{0.5}/\sigma_{l,0}$ values, by approximately a factor of 10, in the mixing layer compared to the lower stream remind of the enhanced heterogeneity of the layer. Of note, among all liquids the largest values of $(\{\theta_l^2\} - \{\theta_l\}^2)^{0.5}/\theta_{l,0}$ occur for diesel, closely followed by RP-1 and JP-7, with Jet A showing distinctively less $\{\theta_l\}/\theta_{l,0}$ variability in the lower part of the mixing layer, apparently due to its increased volatility with respect to all other liquids. Within the range explored, either changes in ML_0 or T_0 lead to substantially ($\sim 60\%$) more elevated values of $(\{\theta_l^2\} - \{\theta_l\}^2)^{0.5}/\theta_{l,0}$, indicating that the diversity of $\{\theta_l\}/\theta_{l,0}$ values will be considerably greater in real combustors where T_0 is much larger. Contrasting to the variation of $(\{\theta_l^2\} - \{\theta_l\}^2)^{0.5}/\theta_{l,0}$ with fuel composition, $(\{\sigma_l^2\} - \{\sigma_l\}^2)^{0.5}/\sigma_{l,0}$ is largest for RP-1 and JP-7 because their narrow composition means that either evaporation or condensation of a very small number of species can greatly affect the liquid PDF. This interpretation is supported by the fact that continuing in decreasing order of magnitude are the $(\{\sigma_l^2\} - \{\sigma_l\}^2)^{0.5}/\sigma_{l,0}$ values for Jet A and diesel, an ordering aligned with the width of their composition, and that the

diesel results fall considerably lower than those of the three kerosenes, consistent with its much larger PDF width.

Size and organization

The information provided by the contour plots of figure 8 was of pictorial nature and did not provide quantitative information about drop size and organization according to position within the volume. Such quantitative information is first provided in figure 17 through St which was defined in §3.1 and is here re-written as

$$St = \frac{\rho_l}{18\rho_{g,0}} \mathrm{Re}_0 \frac{D^2}{\delta^2_{\omega,0}} \tag{3.3}$$

using the definition of Re_0 to eliminate μ. From equation 3.3, it is clear that because all other quantities are initially specified, the variation of St is determined by that of D^2. Illustrated in figures 17a and 17b are $\{St\}$ and $(\{St^2\} - \{St\}^2)^{0.5}$, respectively, at t^*_{tr}. Regarding the drop preferential organization, Le Clercq & Bellan (2004) have discussed how the second invariant of the deformation tensor for compressible flow

$$II_u = -\frac{1}{2}\left[(S_{ij}S_{ij} - S_{kk}S_{ll}) - \frac{1}{2}\omega_i\omega_i\right], \tag{3.4}$$

where the strain rate is

$$S_{ij} = \frac{1}{2}\left(\frac{\partial u_i}{\partial x_j} + \frac{\partial u_j}{\partial x_i}\right), \tag{3.5}$$

is conducive to distinguishing portions of the flow that are of rotational or compressible nature, corresponding to $II_u > 0$, from regions where strain dominates, corresponding to $II_u < 0$. Thus $II_u^{\mathcal{I}}$ is a measure of II_u at the drop locations indicating in particular the sign of this quantity, that is, whether the drop is in a region of rotation and compression, or in a region of strain. Plots of $\{II_u^{\mathcal{I}}\}/(\Delta U_0/\delta_{\omega,0})^2$ and $(\{(II_u^{\mathcal{I}})^2\} - \{II_u^{\mathcal{I}}\}^2)^{0.5}/(\Delta U_0/\delta_{\omega,0})^2$ at t^*_{tr} are presented in figures 17c and 17d.

The average drop size is evidently approximately constant throughout the lower stream and continuously decreases from the lower stream to the mixing layer and throughout

the mixing layer in the direction of the upper stream. In the light of the $\{n_c\}$ variation discussed in conjunction with figure 16a, the larger number of drops per cell in the mixing layer is balanced by their smaller volume, which still leads to a negligible ratio of the drop-to-cell volume, and consequently negligible error in the calculation of the Lagrangian source terms at grid locations. The fact that at all locations $\{St\} < 3$, which is the initial volumetric mean, is indicative of the drop-size reduction due to evaporation. In the lower stream, $(\{St^2\} - \{St\}^2)^{0.5}$ is smaller than the initial volumetric value of 0.5 meaning that the drop size distribution is more uniform, whereas the opposite is evident in the mixing layer, which is a manifestation of the increased size polydispersity resulting from the drop/flow interaction. As expected, both $\{St\}$ and $(\{St^2\} - \{St\}^2)^{0.5}$ decrease with liquid volatility or increasing T_0, and increase with larger ML_0.

Figures 17c and 17e show that except for the lower stream where the drops reside in regions of $II_u = 0$, in the entire mixing layer the drops reside in strain-dominated locations, consistent with the findings of Squires & Eaton (1991). This result gives perspective to the finding of Le Clercq & Bellan (2004) that most drops in the volume accumulate in regions of $II_u \simeq 0$ showing that the result was biased by the much larger number of drops in the lower stream (figure 15). The present results show that with increasing volatility or T_0 and with decreasing ML_0, the drops generally reside in regions of increasing strain. As either T_0 or ML_0 increase, or as the volatility increases (RP-1 and JP-7 not displayed) sharp peaks of larger-strain regions populated with drops are evident, remnant of the parallel sharp peaks observed in figure 16a; this finding indicates that the much larger T_0 in combustors is conducive to generating very-high-strain drop laden regions. Considering the variation of $(\{(II_u^{\mathcal{I}})^2\} - \{II_u^{\mathcal{I}}\}^2)^{0.5}/(\Delta U_0/\delta_{\omega,0})^2$ with $x_2/\delta_{\omega,0}$ (figures 17d and 17f), it appears that the diversity of $\{II_u^{\mathcal{I}}\}/(\Delta U_0/\delta_{\omega,0})^2$ also increases

with more elevated values of volatility, T_0 or ML_0, reinforcing the conclusion about the heterogeneity of characteristics associated with drop locations in combustors.

Probabilities

All homogeneous (x_1, x_3) plane averages show that the drop characteristics are strongly affected by the surrounding flow. To elucidate the influence of the location on the drops, PDFs are separately calculated over the lower-stream and over the mixing-layer drop ensemble, and are displayed in figure 18. For figure readability, results are only shown for diesel and different T_0, as T_0 is considered important in projecting how the results might change at the very much higher T_0 in combustors. (For readability, the curve labels are specific to this figure and changed from those listed in the figure 3 caption.) Because variations with increased T_0 mimic those for liquids with increased volatility, the following results at $T_0 = 400$ K can also be interpreted as being applicable to the kerosenes.

Apparently, the probability of a given number of drops per cell, whether in the lower stream or the mixing layer, is insensitive to T_0 as shown by $P(n_c)$ in figure 18a. Independent of the two locations, the PDF peaks at $\simeq n_c = 0.6$, but is considerably wider for the mixing layer relative to the lower stream, consistent with figure 16b. This is the consequence of drop segregation in the mixing layer, as seen in figures 17c and 17e. In contrast, $P(T_d)$ in figure 18b exhibits high specificity both to T_0 and to the drop location. Independent of T_0, T_d has a much larger range of higher values in the mixing layer than in the lower stream. Also independent of T_0, in both regions, the PDF displays a major peak and then a minor peak at smaller T_d values; although the larger peak is at the same T_d value in both regions, in the mixing layer the minor peak is at inferior values than in the lower stream, making the lower stream PDF wider in the region of most probability. The dual T_d peak corresponds to regions of relatively low T in the central streamwise

portion of the domain caused by the lower p at the center of the final vortex (not shown), surrounded by regions of higher p and thus larger T; figure 9a clearly depicts the dual T_d preferential values in the lower portion of the mixing layer. The major peak indicates a preferential value which for $T_0 = 375$ K is in the lower stream slightly inferior to $T_{d,0}$ and the location of this minor peak, which indicates the lower boundary of the range of most probable values, shows that even within these most probable values, the mixing layer has more variability than the lower stream, consistent with the physical understanding derived from scrutiny of figure 16d.

The composition information presented in figures 18c and 18d shows that independent of T_0, $P(\theta_l)$ peaks at the same θ_l but is much narrower in the lower stream than in the mixing layer, consistent with the similar history of all drops in the lower stream and the diversity of drop history for the mixing layer drops, as clearly seen in figure 9b. At larger T_0, $P(\theta_l)$ is translated to the range of larger θ_l as the more volatile species have been released earlier from the drops, and its width increases, consistent with the information of figure 16f. Of note, some drops have a liquid mean molar mass as heavy as 260 kg/kmol, and this value increases to ~ 300 kg/kmol at $T_0 = 400$ K (not shown). Thus, for the much larger T_0 in combustors, it is expected that the mean molar mass of the liquid will increase from the present values, leading to coke or cenosphere formation when species as heavy as ~ 500 kg/kmol have a non-negligible presence in the drop (Goldstein & Siegmund (1976), Groenzin & Mullins (2000) and Sheu (2002)). Complementary to $P(\theta_l)$, $P(\sigma_l)$ shows that the preferred value is similar for both lower-stream and mixing-layer regions, and that the location of the peak slightly increases with larger T_0. Independent of T_0, the $P(\sigma_l)$ width is larger in the mixing layer, consistent with the information in figure 16h.

3.4.2. *Vapor statistics*

Homogeneous-plane averages of $\theta_v/\theta_{v,0}$ and $\sigma_v/\sigma_{v,0}$ at t^*_{tr} are displayed in figure 19. For both $\langle\theta_v\rangle/\theta_{v,0}$ and $\langle\sigma_v\rangle/\sigma_{v,0}$ the lower stream is characterized by a uniform distribution, with the values increasing into and culminating in the mixing layer, then decreasing and reaching unity in the upper stream.

As ML_0 increases (figures 19a and 19c), both $\langle\theta_v\rangle/\theta_{v,0}$ and $\langle\sigma_v\rangle/\sigma_{v,0}$ decrease throughout the lower stream and mixing layer, indicative of evaporation being relatively restricted to the more volatile, lighter species. The magnitudes of $\langle\theta_v\rangle/\theta_{v,0}$ and $\langle\sigma_v\rangle/\sigma_{v,0}$ are mildly sensitive to an augmentation in Re_0 (figures 19a and 19c), as evidenced by similar values at different Re_0 both in the lower stream and in the lower part of the mixing layer, however, additional structure is observed at the higher Re_0 and the upper edge of the layer contains now heavier species meaning that the composition is more heterogeneous.

Figure 19b shows that the diesel and Jet A $\langle\theta_v\rangle/\theta_{v,0}$ profiles coincide, independent of T_0, and that RP-1 and JP-7 results are very close at both values of T_0. We conjecture here that the coincidence of diesel and Jet A means that it is not only the width of the liquid composition PDF that matters under transitional conditions, differentiating the diesel and Jet A from RP-1 and JP-7, but also the identity of the most volatile species. Jet A experiences evaporation in the lower stream, as shown by $\langle\sigma_v\rangle/\sigma_{v,0} > 1$ in figure 19d, which together with the larger mean molar mass there indicates enhanced release of less volatile species. Across the layer, evaporation occurs for all kerosenes, but for diesel condensation occurs except at the larger T_0 where evaporation prevails only at locations higher than $\sim x_2/\delta_{\omega,0} > 5$ in the layer. The physical picture that emerges from consideration of $\langle\sigma_v\rangle/\sigma_{v,0}$ together with the $\langle\theta_v\rangle/\theta_{v,0}$ profiles is that of an accumulation of high molar mass species in the core of the layer, with a relatively narrower distribution than at both lower and upper layer boundaries. The composition at the lower boundary

of the mixing layer does not have in the mean as high a molar mass as the layer core, but it has a wider species distribution, with presumably a multitude of highly volatile species entrained from the lower stream. At the upper mixing layer boundary, the composition is also wider than in the layer core, with a larger mean molar mass than either the core or the lower layer region, this being due to the higher-m species that evaporate once the very volatile and moderately volatile species have been released from the drops that have traversed the mixing layer to reach its upper boundary. This physical picture is consistent with that derived from examination of figure 9b.

3.5. *Dissipation analysis*

3.5.1. *Irreversible entropy production*

Because the energy spectra of figure 4 showed significant differences in the small-scale energy from the SC-liquid study of Okong'o & Bellan (2004), suggesting here a more pronounced small-scale dissipation, it is of interest to examine the irreversible entropy production, which is essentially the dissipation. Okong'o & Bellan (2004) have shown that for a TP flow, additional to the semi-definite positive quadratic terms in the SP dissipation, there are also source terms present; in the SC-liquid study of Okong'o & Bellan (2004), the source terms entirely dominated the dissipation budget at transition. Here the same result applies as in Okong'o & Bellan (2004), as the equations for ξ_{nv} are not involved in the derivation. Specifically, according to Okong'o & Bellan (2004) the dissipation, g is

$$g = g_{III} + g_{II} + g_{I,kine} + g_{I,chpot} + g_{visc} + g_{temp} + g_{mass}, \tag{3.6}$$

$$g_{III} = \frac{S_{en}}{T}, \quad g_{II} = -\frac{u_i S_{mom,i}}{T}, \quad g_{I,kine} = \frac{\frac{1}{2}u_i u_i S_{mass}}{T}, \quad g_{I,chpot} = -\frac{\mu_v S_{mass}}{T}, \tag{3.7}$$

$$g_{visc} = \frac{2\mu}{T}\left(S_{ij} - \frac{1}{3}S_{kk}\delta_{ij}\right)\left(S_{ij} - \frac{1}{3}S_{ll}\delta_{ij}\right), \tag{3.8}$$

$$g_{temp} = \frac{\lambda}{T^2}\frac{\partial T}{\partial x_j}\frac{\partial T}{\partial x_j}, \quad g_{mass} = \frac{R_a R_v}{Y_a Y_v \left(R_v Y_v + R_a Y_a\right)}\frac{1}{\rho \mathcal{D}}\left[-\frac{\partial (cX_v)}{\partial x_j}\right]\left[-\frac{\partial (cX_v)}{\partial x_j}\right] \tag{3.9}$$

where $R_v = R_u/\theta_v$ and $\mu_v = h_v - Ts_v$ is the chemical potential with s_v being the entropy of the pure vapor which is calculated for a perfect gas as

$$s_v = \int C_{p,v}(T)\frac{dT}{T} - \int R_v \frac{dp}{p}, \tag{3.10}$$

given a functional form for $C_{p,v}(T)$, where it is required that s be null at 0K (in practice the integration is carried out from 1K due to the logarithmic singularity at $T = 0$). Therefore,

$$s_v = s_v^0 + \int_{T^0}^{T} C_{p,v}(T)\frac{dT}{T} - R_v \ln(p/p^0), \tag{3.11}$$

where s_v^0 is the reference entropy at the reference temperature T^0 and pressure p^0, typically obtained from integration or tables.

Considering the entire g contribution due to drop source terms

$$g_d = g_{III} + g_{II} + g_{I,kine} + g_{I,chpot}, \tag{3.12}$$

$$g_d = -\frac{Q_{\text{conv-diff}}}{T} - \dot{m}_d s_{v,s} - \frac{\dot{m}_d}{T}\frac{u_{sl,i}u_{sl,i}}{2} + \frac{M_d}{\tau_d}f_1\frac{u_{sl,i}u_{sl,i}}{T}, \tag{3.13}$$

having assumed that s_v is calculated at the drop surface (consistent with the calculation of h_v in S_{en}), shows that because the last term in equation 3.13 is always positive, the sign of g_d is determined by the sign and magnitude of the first three terms. Under net evaporative conditions, $\dot{m}_d < 0$, and thus the second and third terms of equation 3.13 are also positive; the opposite happens under net condensation conditions. Finally, for $T_d < T$, which are the prevailing conditions in the present simulations, the first term

is negative. Thus, under net evaporative conditions, the sign of g_d is determined by the relative magnitude of the first term compared to sum of the other terms of equation 3.13. The implication is that strong droplet heating promoted by a large value of $(T-T_d)$ could lead to a reduction in g with respect to a SP flow having the same thermodynamic gradients, if evaporation is weak, that is, if the liquid is not very volatile, and also if the slip velocity is small. These considerations show that liquid volatility plays a strong role in determining the value of the dissipation, and identifies the reasons why TP flows with liquids of different composition have disparate characteristics.

Presented in table 4 is the g budget for all $ML_0 = 0$ simulations. Similar to the findings of Okong'o & Bellan (2004) for SC SP simulations, g_{visc} augments with increasing Re_0 and g_{temp} is very small. We find here that a mass flux similar in magnitude to that occurring at transitional states for the MC TP flows can add for SP flows about 7% of g_{visc} to the average g in the form of scalar dissipation; the relative r.m.s. of g_{mass} to g_{visc} is though much larger, $\sim$ 12%. Not only is there the additional contribution of g_{mass}, but also g_{visc} is greater and this augmentation increases with Re_0 to up to $\sim$ 15% when Re_0 increases by a factor of 2.5. For corresponding simulations, both g and its contributions are larger for SC SP flows (compare table 4 to table 10 of Okong'o & Bellan (2004)), indicating that even for SP situations, the MC feature may affect the turbulent characteristics of a flow, mainly through the change in molar mass.

Because calculation of the g budget involves for TP flows the value of s_v^0, which may be difficult to compute for MC liquids, this potential intricacy is here bypassed by considering the budget of

$$g^* = g - s_v^0 S_{mass} \tag{3.14}$$

which is the irreversible entropy production associated with $(s - s_v^0)$ and by calculating $(s - s_v^0)$ according to equation 3.11 with the choice of $T^0 = T_l$ so as to eliminate the

computation of the problematic liquid entropy; we choose $p^0 = p_0$. The budget of g^* is calculated in the same manner as that of g, except that in equation 3.6 $g_{I,chpot}$ is now replaced by $g^*_{I,chpot} = g_{I,chpot} - s^0_v S_{mass}$. The g^* budget for TP simulations is presented in tables 5 and 6 for quantities calculated at grid nodes (e.g. the first row and first column value represents $\langle\langle g_{III}\rangle\rangle$), and in table 7 for quantities calculated at grid nodes and then interpolated at the drop location (e.g. the first row and first column value represents $\left\{\left\{g^T_{III}\right\}\right\}$). All tables list averages, r.m.s. and the % of the ensemble where positive or negative values occur. The vertical listing of terms in the tables follows that of Okong'o & Bellan (2004) (where they were listed in decreasing order of r.m.s. values for the baseline case) for easy comparison of terms other than $g^*_{I,chpot}$ and g^*.

It is apparent from table 5 that, excluding the non-comparable $g^*_{I,chpot}$, the decreasing order of the r.m.s. values remains from the SC n-decane study of Okong'o & Bellan (2004). However, at same initial conditions, g_{III} is smaller in magnitude, whether average or r.m.s., and this holds for diesel and all kerosenes (tables 5 and 6), with RP-1, the liquid with the narrowest PDF, approaching n-decane closest. For diesel at the (7% relatively) higher T_0 (table 5), the average g_{III} is larger by $\sim$ 15% for the average and $\sim$ 23% for the r.m.s. confirming the important influence of T_0 for liquids of low volatility. A similar comparison for Jet A (table 6) reveals practically no difference with T_0, which is attributed to the more modest role of a such small relative increase in T_0 for fuels of higher volatility. Because

$$\begin{aligned} sign(g_{III}) &= -sign\left[v_j F_j + Q_{\text{conv-diff}} + Q_{\text{evap}} + \dot{m}_d\left(\frac{v_j v_j}{2} + C_l T_d\right)\right] \\ &= -sign\left[v_j F_j + \frac{\lambda Nu}{D}\frac{\ln(1+B_T)}{B_T} A\left(T - T_d\right) + \dot{m}_d\left(\frac{L_{veff}}{B} + \frac{v_j v_j}{2} + C_l T_d\right)\right] \end{aligned} \tag{3.15}$$

it is clear that $g_{III} < 0$ only if the sum of the first two terms, representing the work due to drag and drop heating, dominate the effect of evaporation. Although $\langle\langle g_{III}\rangle\rangle > 0$

for all simulations, and in most of the domain $g_{III} > 0$, there is a non-negligible % (more than 15%) of the volumetric domain where its value is negative for all $ML_0 = 0.2$ simulations, and this percentage increases at the larger T_0. With increasing ML_0, the % of the domain with $g_{III} < 0$ decreases, which is attributed to the reduction in $\dot{m}_d$ combined to the larger drag and flow-to-drop heat transfer associated with the much larger number of drops. Of note, the percentages of strictly positive and strictly negative g_{III} activity do not necessarily add up to 100 because there may be no activity at all in the considerable part of the domain represented by the upper stream; in fact, only $\sim 74\%$ to 79% of the volume is prone to non null g_{III} activity, and this percentage increases at larger ML_0 or T_0 but is not sensitive to liquid volatility.

For all fuels and under all conditions, $\left\langle\left\langle g^*_{I,chpot}\right\rangle\right\rangle < 0$ and dominates g^* in magnitude; similarly, the r.m.s. of $g^*_{I,chpot}$ is the largest among all contributions to g^*. This means that the composition of the fuel has a major impact on the irreversible $(s - s^0_v)$ production. Both the $g^*_{I,chpot}$ average and r.m.s. increase with ML_0 but slightly less than proportionally, and with T_0 or larger fuel volatility.

In contrast to g_{III}, the g_{visc} contribution, whether average or r.m.s., is here larger in magnitude (by $\sim 20\%$) than in Okong'o & Bellan (2004), decisively explaining why the smallest scales in the energy spectra of figure 4 contain here orders of magnitude less energy than in the equivalent spectra of Okong'o & Bellan (2004). None of the parameters considered here (ML_0, T_0 or liquid volatility) affect this conclusion, which seems to be entirely related to the MC aspect of the flow. Like for all other flux-related dissipation terms (i.e. g_{mass} and g_{temp}), the entire domain has a positive activity. Relative to the SP budget of table 4, g_{visc} is now larger by $\sim 35\%$ in average and $\sim 29\%$ in r.m.s.. Although at first consideration this result may seem contradictory to the reduced energy in the small scales for SP flows evident in figures 4a and 4b, the fact is that the initial energy in

SP and TP flows is not the same (because of the additional energy due to the presence of drops) as shown in figure 4b, and moreover the kinetic energy in TP flows first increases with time compared to the decrease experienced by SP flows (figure 5a), which brings the correct perspective to this result.

Previously analyzed in detail by Okong'o & Bellan (2004) in their n-decane study, here $\langle\langle g_{II}\rangle\rangle > 0$ for diesel, but $\langle\langle g_{II}\rangle\rangle < 0$ for all kerosenes independent of T_0, indicating that for diesel it is drag that dominates, whereas for the kerosenes it is evaporation that governs the sign of this term. Confirming this interpretation, $\langle\langle g_{II}\rangle\rangle$ becomes increasingly positive at the larger ML_0 and substantially decreases with augmenting T_0; the same variation is apparent for the r.m.s., portraying the increased (decreased) heterogeneity in the flow with increasing (decreasing) ML_0 (T_0). For diesel, an approximately similar % of the domain experiences positive or negative $\langle\langle g_{II}\rangle\rangle$ activity, whereas for all kerosenes there is a larger % of negative activity regions. At the larger ML_0, the % of regions of positive activity increases, which results from the increased drag on a larger number of drops combined with the decreased evaporation due to heat-transfer limitations, and at the larger T_0 the opposite holds, owing to the increased evaporation rate due to promoted heat transfer combined with the decreased drag on smaller drops.

Both g_{mass} and g_{temp} are for all liquids more than a factor of 50 smaller than the largest g contribution, and $g_{I,kine}$ is even smaller. Because

$$sign(g_{I,kine}) = sign(-\frac{d(\mathcal{N}\theta_l)}{dt}) \tag{3.16}$$

this means that regions of $\langle\langle g_{I,kine}\rangle\rangle > 0$ ($\langle\langle g_{I,kine}\rangle\rangle < 0$) correspond to net evaporation (net condensation). Apparently, independent of the the liquid, ML_0 or T_0, net evaporation occurs in a larger % of the domain than net condensation. The kerosenes with a narrower composition PDF (i.e. RP-1 and JP-7) are particularly prone to net evaporation over a larger part of the domain due to the lack of much more volatile species than the

mean that could have condensed on the drops. Similarly, the extent of net evaporation regions also becomes more preponderant with increasing ML_0 presumably due to the larger number of drops which increases the portions of the domain populated by drops. The results show almost no sensitivity to T_0, however, with increasing liquid volatility $g_{I,kine}$ increases, consistent with the plots of figure 5b.

Compared to MC SP simulations, the values of all flux contributions of g are larger for MC TP flows, whether average or r.m.s.; this is similar to the SC results of Okong'o & Bellan (2004). However, one noteworthy distinguishing feature is that in going from SC to MC flows, the g_{visc} average increases by only half as much from SP to TP situations, whereas its r.m.s. augmentation is by a factor of 3 larger than for SC flows, suggesting that the MC-liquid phase change suppresses the increase in the average and introduces additional variability in g_{visc}.

Whereas tables 5 to 6 correspond to the dissipation in an Eulerian framework, table 7 is an example of the gas dissipation g^* as 'seen' by the drops, that is, in a Lagrangian framework. In this Lagrangian framework, the % regions of positive activity added to the % of negative activity locations yields 100%. A small error is evident in the computed values for g_{mass} and g_{temp}, which, although adding to the expected 100%, show an unphysical 1% region of negative activity; the computation error is evidently due to the operation $\mathcal{I}$. Similar to $\langle\langle g^* \rangle\rangle$, $\left\{\left\{(g^*)^{\mathcal{I}}\right\}\right\}$ is negative and decreases in magnitude with ML_0 and T_0, and increases with fuel volatility, that is with a smaller γ (see table 1). The negative value of $\left\{\left\{(g^*)^{\mathcal{I}}\right\}\right\}$ again represents the dominance of $g^*_{I,chpot}$ which is the only negative contribution. It is clear that for all liquids (only diesel and Jet A shown) and for each specified simulation, over the drop ensemble g_{III} has a much larger value than at grid nodes, both average and r.m.s.; $g^*_{I,chpot}$ is in average larger in magnitude than at grid nodes by a factor of $\sim$2.5 to 4.5 for diesel and $\sim$4 for kerosenes, and its r.m.s. is

larger than at grid nodes by a factor of ~2 to 3; g_{visc} is smaller both in average and r.m.s. for all liquids; g_{II} has a similar average value but a larger r.m.s. for diesel, a much larger absolute value (by a factor of 26) and a much larger r.m.s. for Jet A (and both other kerosenes; not shown); for all liquids, g_{mass} and g_{temp} are 50% to a factor of 2 larger in average and r.m.s. when calculated over the drop ensemble; and independently of liquid, $\{\{g^{\mathcal{I}}_{I,kine}\}\}$ is by a factor of 2-3 larger than $\langle\langle g_{I,kine}\rangle\rangle$ with now a larger % allocated to negative values, corresponding to net condensation, and ~ a factor of 2 larger in r.m.s.. For all liquids, the T_0 variation of each contribution to $(g^*)^{\mathcal{I}}$ is consistent with that seen for the domain statistics. The general picture obtained when scrutinizing g^* over the drop ensemble is that although the general conclusions are similar with those obtained for the g^* statistics over the volumetric domain, the details may considerably vary. This raises the question of how does the composition PDF, which according to equation 2.16 is a DGPDF for the vapor at the drop surface, evolve in mathematical form from the drop surface to the grid nodes; this topic is addressed in §3.6.

3.5.2. *Scalar dissipation representation*

Although the present results agree with the study of Okong'o & Bellan (2004) regarding the negligible aport of g_{mass} to g, this does not imply that g_{mass} is not a quantity of interest. For example, in non-premixed turbulent combustion models it is frequently assumed, for simplicity, that flames are infinitesimally thin with respect to turbulence scales, and thus that the role of turbulence is merely to distort these infinitely thin flames, thus increasing their surface and augmenting the reaction rate; these are called 'flamelet' models. The turbulent reaction rate is then assumed to be proportional to g_{mass}, which is specified through a mathematical form. The g_{mass} mathematical form has been assumed Gaussian until recently, without much experimentally-based justification.

Beyond the practical need of modeling flamelet reaction rates lies the general topic

of passive (no reaction; only transport) or active (phase change and/or reaction and transport) scalar dispersion and mixing in turbulent flows, also related to quantifying intermittency in turbulent mixing. This topic has sparked substantial interest in the past, but has so far been addressed only for either liquid or gaseous SP flows. Concentrating on the investigations of the last decade, the experimental work of Buch & Dahm (1996) for liquid flows (i.e. $Sc = O(10^2)$ conditions) preceded their SP gaseous flow (i.e. $Sc = O(1)$ conditions) studies. Passive scalars have been investigated by Tong & Warhaft (1995), Buch & Dahm (1998), Su & Clemens (1999), Warhaft (2000), Kothnur & Clemens (2001), Probst & Ghandi (2003) (although their experimental set up is that of a spray engine, the drops are allowed a 4 ms stay in pressurized air, after which the resulting gaseous mixture is injected in the measurement chamber) and Su & Clemens (2003). Active, reactive scalars have been studied by Karpetis & Barlow (2002), Mason, Chen & Im (2002), Karpetis & Barlow (2004), Barlow & Karpetis (2004a), Barlow & Karpetis (2004b) and Karpetis, Settersten, Schefer & Barlow (2004). Kothnur & Clemens (2001) addressed the relationship between scalar dissipation and strain in non-reacting turbulent planar jets at atmospheric conditions. The work of Su & Clemens (1999) and of Su & Clemens (2003) focused on measuring the dissipation in propane jets (seeded with acetone) co-flowing with air. Karpetis & Barlow (2002), Karpetis & Barlow (2004), Barlow & Karpetis (2004a), Barlow & Karpetis (2004b), and Karpetis, Settersten, Schefer & Barlow (2004) concentrated on measuring the scalar dissipation for atmospheric methane/air jet flames; some evidence is presented in Karpetis & Barlow (2004) showing that simple flamelet concepts may not be applicable to those flames.

Illustrated in figure 20a is the visualization of $\log_{10}[(\nabla(cX_v)) \cdot (\nabla(cX_v))]$ in the same between-the-braid plane as the visualizations of §3.3. The legend extends from practically null values (i.e. 10^{-8}) to $\sim 10^{-1}$, encompassing a very wide variation. The filamentary

structure widely discussed in the literature is evident, as is also the increasing level of structural complexity when compared to the passive scalar results of Su & Clemens (2003) (their figure 4). Notably, cX_v is here an active scalar, as it originates from drop evaporation. Figure 20a shows no activity in the upper stream, and minimal activity in the lower stream. However, the mixing layer displays highly contorted regions of large scalar dissipation, indicative of intense mixing, coexisting with adjacent locations of low scalar dissipation.

The lucid presentation of Su & Clemens (2003) identifies the crucial questions when studying the scalar dissipation, one of which is: What is the mathematical form of the

$$\Pi \equiv \mathcal{D}\left[-\frac{\partial(cX_v)}{\partial x_j}\right]\left[-\frac{\partial(cX_v)}{\partial x_j}\right] = g_{mass}\rho\frac{Y_a Y_v\left(R_v Y_v + R_a Y_a\right)}{R_a R_v} \tag{3.17}$$

PDF? Is the Gaussian PDF typically assumed for $\log\Pi$ in flamelet models a good representation? All experimental investigations of passive scalars, examples of which are Buch & Dahm (1996), Su & Clemens (2003) and Probst & Ghandi (2003), show that the PDF of $\log\Pi$ is indeed close to a Gaussian, but that it exhibits a small negative skewness that distinguishes it from the Gaussian (which has null skewness). The departure from Gaussian was shown by Su & Clemens (2003) to hold at significant values and over an engineering-useful range of (outer scale) Re (3290 to 8330). When conditioned to larger Re, the skewness magnitude was reduced, consistent with the clear discussion of Warhaft (2000) regarding the subtle departure from local isotropy for both inertial and dissipation scales at experimentally attainable values of (rather than infinite) Re and with his considerations on the scalar PDF tails. Nevertheless, the fact is that for the Re magnitudes relevant to engineering applications, the non-Gaussian behavior prevails, as also experimentally found by Karpetis & Barlow (2004) for active scalars.

The present results extend the existing SP studies to TP flows. Because the drop/flow interaction affects both vapor release and mixing, there is no guarantee that the previous

SP conclusions are applicable. Plotted in figure 20b is an example of the $\log(\Pi/\mathcal{D})$ PDF at t^*_{tr}, computed here for the baseline case (table 1); because $\mathcal{D}$ is constant, this does not change the interpretation of the result. To differentiate between mixing in the relatively low-turbulence lower and upper streams from that in the full mixing layer, which is in a transitional state, and moreover from that in the core of the mixing layer which experiences the largest mixing activity (see figure 20a), separate PDFs are presented. In all three regions, the PDF is decisively non-Gaussian, although it displays a Gaussian-like portion. In the lower stream, the PDF peaks at small scalar products, which is a manifestation of the flow near-uniformity, and a small tail extends into the region of larger scalar products. In contrast, the full mixing layer PDF peaks in the region of relatively larger scalar products with a secondary peak in the range of small values and finally a tail at very small values; the secondary peak is due to regions of relative inactivity included in the domain (see figure 20a). Finally, in the mixing layer core the PDF expectably peaks at the same location that the PDF in the full mixing layer, but is more akin to a Gaussian, although it also displays the tail characteristic of the full layer. The same effect of tendency towards Gaussian behavior with increased turbulent activity was found by Warhaft (2000), Su & Clemens (2003) and others, but for a passive scalar and in SP flows. Comparing to the results of Su & Clemens (2003) (their figure 5a; note that the abscissa is not the same as here), we find a fuller PDF in the large side of the scalar products with respect to the peak, which is indicative of the larger heterogeneity of the conditions in our layer relative to the Su & Clemens (2003) turbulent jet; this increased heterogeneity is evident in comparisons of the present figures 12a and 20b with figures 2 and 4, respectively, of Su & Clemens (2003) and is attributed to the drop/flow interaction. Effectively, the vapor source terms locally increase X_v, thus generating higher gradients. This generation of high gradient (that is, larger scalar dissipation) zones is typical to

TP flows. Therefore, we have highlighted a qualitative difference between SP and TP scalar dissipation distributions that could, with additional modeling, be integrated in combustion models for TP flows.

The implication of this discussion is that a scalar dissipation rate modeled as a Gaussian is strictly valid only at infinite Re values, recalling the similar statement of Warhaft (2000). Compared to SP flows, for TP flows the Gaussian assumption may be additionally questionable due to the increased range of Re values in the flow, which is a manifestation of the drop/flow interaction, leading to increased mixing-level heterogeneity.

3.6. *Vapor-composition PDF representation*

The discussion of the dissipation in §3.5.1 raises the possibility that given the different 'appearance' of the flow in the Eulerian or Lagrangian frameworks, the vapor-composition PDF, which is a DGPDF at drop locations may not have the same mathematical form at grid nodes. Le Clercq & Bellan (2005) assumed in their pre-transitional simulations that the vapor composition remained a DGPDF, an approximation which was justified by the relatively lower heterogeneity in composition relative to the present transitional simulations (compare their figures 12 and 13 with present figures 13 and 14, respectively). Thus, here we explore the mathematical form of the vapor-composition PDF through the excess moments $\xi'_{n,v}$ of equation 2.4. That is, we compare the vapor-composition PDF, of which we only know the calculated first four moments computed as the solution of the gas-phase equations, with the SGPDF that has the same first two moments as the computed PDF; this PDF has so far an unknown mathematical form.

Figures 21a and 21b show $\left\langle \xi'_{3,v}/\xi^{SGPDF}_{3,v} \right\rangle$ and figures 21c and 21d display $\left\langle \xi'_{4,v}/\xi^{SGPDF}_{4,v} \right\rangle$. In all cases, both $\left\langle \xi'_{3,v}/\xi^{SGPDF}_{3,v} \right\rangle$ and $\left\langle \xi'_{4,v}/\xi^{SGPDF}_{4,v} \right\rangle$ are very small, $\sim O(10^{-3})$ and negative, although the fourth order moment tends to have values larger by a factor of 5 than the corresponding third moments. The smallest magnitude of $\left\langle \xi'_{3,v}/\xi^{SGPDF}_{3,v} \right\rangle$ and

$\left\langle \xi'_{4,v}/\xi^{SGPDF}_{4,v} \right\rangle$ is in the lower and upper streams, while the mixing layer hosts the largest values. The deviation from the SGPDF increase with decreasing ML_0 (figures 21a and 21c) and with increasing T_0 (figures 21b and 21d); at more elevated Re_0, the region of larger departure shifts towards the upper stream, and the departure from the SGPDF is larger (figures 21a and 21c). A smaller ML_0, larger T_0 or higher Re_0 promote evaporation (figure 6) and thus the evolution of species that potentially could condense and could contribute to the formation of a PDF different from the SGPDF; notably, Harstad, Le Clercq & Bellan (2003) showed that for the liquid, departures from the SGPDF increased at larger evaporation rates and these departures were traced to species condensation on the drops. The departure from the SGPDF decreases in the lower stream with increasing value of the lowest-m species, as vapor evolution in this region is entirely due to the most volatile species of the liquid; because Jet A exhibits here considerably more evaporation than diesel and the two other kerosenes, its P_v displays most departure from the SGPDF (figures 21b and 21d). The mixing layer being a region of evaporation where a multitude of molar mass species are released from the drops, the departures from the SGPDF align here with the width of $P_{l,0}$ because more species are available for condensation and the vapor emanating from the liquid with the largest $P_{l,0}$ width – diesel – has the largest departure from the SGPDF.

Finally, $\{\varepsilon_l\}$ is illustrated in figure 21e, and now assuming that the vapor-composition PDF is of the double-Gamma form, $\langle \varepsilon_v \rangle$ is portrayed in figure 21f; the jagged aspect of the curves in figure 21e is due to ensemble averaging a liquid variable over drops residing in planes (see discussion in §3.4.1). The activity is almost uniquely confined to the mixing layer. Clearly, the deviation of the vapor composition from SGPDF is greater by $\sim 50\%$ in the vapor than in the liquid, although in both cases the departure is small; according to Harstad, Le Clercq & Bellan (2003), this small departure is though crucial

to the physical tenability of the model. Thus, if P_v is a DGPDF, its departure from the equivalent SGPDF is larger than that of P_l from its corresponding SGPDF. Comparing all liquids according to their composition, a relatively larger departure from the SGPDF in the liquid leads to a relatively smaller departure for the vapor; we interpret this opposite variation as being the effect of condensation onto the drops which depresses the minor double-Gamma peak in the vapor and increases it in the liquid, this interpretation being supported by the approximate coincidence of the peaks in figure 21f with the peaks in figures 19b and 19d. Most deviation in the liquid and least departure in the vapor from the SGPDF are for RP-1 and JP-7 because of their narrower initial composition PDF implying a narrower range of saturation pressures. Decreasing (increasing) in deviation from SGPDF, Jet A liquid (vapor) is intermediary between the other two kerosenes and diesel. At the more elevated T_0 (ML_0), both liquid and vapor experience larger (smaller) DGPDF effects. The major and minor mixing-layer peaks in figure 21f coincide with isolated regions of high ρ_n (figure 8), prone to large net evaporation.

4. Conclusions

Transitional states were created through Direct Numerical Simulation (DNS) for both multicomponent-species (MC-species) gaseous mixing layers and drop-laden mixing layers where the evaporating liquid is a MC mixture of a very large number of species. The mixing layer was three-dimensional, and when drops were present, they were initially confined to the lower stream. The gas was followed in an Eulerian framework, whereas the drops were described in a Lagrangian frame, with complete coupling between drops and carrier gas accounting for exchanges of mass, species, momentum and energy. The liquid and vapor composition resulting from evaporation/condensation were modeled using Continuous Thermodynamic concepts wherein a Probability Distribution Function

(PDF), taken here as a function of the species molar mass, describes each evolving PDF; the gas PDF is a function of time and location, and the liquid PDF varies with time and is specific to each drop. The liquid PDF was initially specified as a single Gamma PDF (SGPDF) and was allowed to evolve into a linear combination of two Gamma PDFs (DGPDF); according to Cotterman, Bender & Prausnitz (1985), the vapor composition at the drop surface has the same functional form as the liquid PDF, but this does not mean that the PDF form is conserved away from the drop surface. Indeed, the conservation equations were written for the first four moments of the vapor composition away from the drops, but the vapor composition mathematical form was not presumed to necessarily be either a SGPDF or a DGPDF. The layer initially consists of four spanwise vortices whose double pairing, promoted by a perturbation, results in the formation of an ultimate vortex in which small scales proliferate. The criterion for transitional state achievement was that one-dimensional energy spectra based on velocity fluctuations display the smooth aspect characteristic of turbulence.

For gaseous (i.e. single phase; SP) mixing layers, the emphasis was on the characteristics of the transitional states as a function of the initial Reynolds number, Re_0, and of the initial species mass flux between the two streams. For drop-laden (i.e. two phase; TP) mixing layers, the emphasis was on the drop/flow interaction and the influence of the initial mass loading, ML_0, of the initial carrier gas temperature, T_0, and of the identity of the liquid; no Re_0, effect could be studied for TP flows due to computational platform memory constraints. Also, because the characteristic drop lifetime had to be matched to that of the flow at values of Re_0 that were lower than in a fully turbulent combustor, selected T_0 values were here smaller than those in combustors. The non-dimensional initial conditions were all matched for the four liquids investigated - diesel and the three kerosenes Jet A, RP-1 and JP-7 - and specified the same ML_0, Re_0, and drop/flow in-

interaction through the Stokes number, St_0, all being non-dimensional numbers that allow comparisons of self-similar solutions in the spirit of Batchelor (1967). Comparisons of the present findings with the single-component (SC) DNS results of Okong'o & Bellan (2004) and with the pre-transitional DNS solutions of Le Clercq & Bellan (2005) using the same model as here were also performed.

The findings show that for SP flows, the value of Re_0 only influences the growth of the layer at transition, but not its evolution to transition. For TP flows, the layer growth was mainly affected by ML_0 and T_0, but not by the liquid identity; all parameters, but primarily the liquid identity had an impact on the amount of vapor released in the gas. The global vortical aspects of the flow were strongly dependent on Re_0 for SP flows and were impacted by ML_0 and especially by T_0, but were found insensitive to the identity of the liquid for TP flows. The variation with Re_0 and ML_0 is similar to that found by Okong'o & Bellan (2004) in equivalent simulations, and the sensitivity to T_0 constitutes a major difference from the pre-transitional results of Le Clercq & Bellan (2005) with the present model.

Ensemble averages over the drops in the mixing layer at transition showed that the drop temperature, T_d, is mostly affected by T_0, ML_0 and liquid identity and that small differences in T_d result in large differences in drop diameter reduction due to evaporation. T_0 and ML_0 have opposite effects in that increasing the former promotes evaporation whereas increasing the latter hinders it, resulting in much larger drops. The kerosenes evaporated much faster than diesel, due to their much higher volatilities. The standard deviation of the liquid composition showed that strong early drop evaporation is followed by drop condensation, resulting in the mean liquid molar mass, θ_l, monotonically increasing but at a varying rate determined by the relative evaporation/condensation process. Volumetric averages over the mixing layer showed that, for the chosen vapor

initial condition, strong condensation initially occurs concurrent with species addition through evaporation. Whether in the liquid or the vapor, the liquid identity is the prime determinant of the composition evolution with respect to the initial conditions, followed by ML_0 and T_0.

Examination of flow visualizations, probabilities over the drop ensemble of drop-related quantities, drop ensemble averages of gas quantities calculated at the drop locations, and homogeneous plane averages, all at transition, allowed an in-depth probing of the database. A very complex drop number distribution was evident that was liquid and T_0 specific, confirming the important role of T_0 in these transitional simulations; the drops in the mixing layer were shown to overwhelmingly congregate in high-strain locations, as first found by Squires & Eaton (1991). In the mixing layer, T_d displayed a high level of heterogeneity, with the largest values encountered mainly at the top of the ultimate vortex, where there is contact with the free-stream highest-temperature carrier gas; however, drops having the highest temperature values were also interspersed in the lower part of the mixing layer. Whether in the mixing layer or in the lower stream, T_d exhibited two preferential values, but the range between preferential values was narrower in the mixing layer. The value of θ_l was generally, but not entirely correlated with the drop temperature in that the majority of the highest values occurred at the top of the ultimate vortex where strong evaporation depletes the volatiles, leaving behind a liquid with relatively high θ_l; the value of θ_l increased with T_0 indicating that at combustor magnitudes diesel drops will attain θ_l values conducive to tar, and therefore cenosphere formation. The lack of complete correlation between drop location and θ_l is a manifestation of the turbulent mixing that imparts to each drop its specific evolution. For SP flows, the flow spanwise vorticity increased with increasing Re_0 and decreasing species mass flux, the latter effect being traced to the reduced scalar dissipation. As in the findings of Okong'o & Bellan

(2004), the maximum value of the spanwise vorticity was larger for TP flows than for SP flows, which was attributed to the source of vorticity represented by the drop/flow interaction, but with increasing ML_0 the opposite occurred along with the formation of concentrated regions of high vorticity conjectured to result from the amplified local interaction between the larger size drops with the flow. The distribution of the spanwise vorticity strongly varied with liquid initial composition, its maximum attained value was mainly influenced by the lightest species entering the composition of the liquid rather than by the width of the composition PDF, and its maximum was larger with T_0, departing from the results of Le Clercq & Bellan (2005) and being the manifestation of the turbulence production due to drop/flow interaction. The distribution and values of the vapor mass fraction and vapor composition displayed high variation with all parameters of the simulations, and generally the range of the mean molar mass, θ_v, aligned with that of the initial liquid composition. Unlike in the results of Le Clercq & Bellan (2005), regions of high θ_v no longer entirely coincided with regions of high vapor composition standard deviation, which was attributed to the enhanced mixing due to turbulence. Consideration of all vapor properties indicated that the core of the layer is composed of high molar mass species having a relatively narrower distribution than at either lower or upper layer boundaries. The lower part of the mixing layer contains relatively low molar mass species, which are presumably entrained from the lower stream that contains the very volatile, early-evaporated species. The highest molar mass species accumulate at the upper part of the mixing layer, and the vapor composition is also wider than in the layer core.

Inspection of velocity-fluctuation-based energy spectra at transition revealed that the energy cascade is of similar strength in MC and SC equivalent flows but that the energy in the highest wavenumbers is reduced in MC TP flows by many orders of magnitude

from that of Okong'o & Bellan (2004) calculated for SC TP flows. An assessment of the irreversible entropy production (i.e. the dissipation) balance showed that the viscous dissipation is indeed here larger by $\sim 20\%$ for diesel (the exact amount is liquid composition dependent) than for the n-decane simulations of Okong'o & Bellan (2004), explaining the reduced energy in the smallest scales. For SP flows, it was found that both the total dissipation and each of its contributions were smaller for MC flows than in corresponding SC simulations. Therefore, whether gaseous or drop-laden flows, the gas composition has an impact on the turbulent characteristics of the flow.

Because the dissipation calculated at the drop locations showed that the flow aspect may change according to the frame of reference, the form of the vapor PDF, which is a DGPDF at each drop surface, was investigated at grid nodes. In all cases, the vapor composition at the nodes is distinct from a SGPDF, but the deviation is very small. Under the assumption that the form of the vapor PDF at the nodes is a DGPDF, it was shown that in the vapor the departure from the SGPDF is larger than that in the liquid. According to Harstad, Le Clercq & Bellan (2003), it is this small but necessary deviation that permits the achievement of a correct physical simulation.

Although the examination of the TP MC dissipation balance showed that the scalar dissipation is nearly one of its smallest contributions, recalling its utilization in the modeling of flamelets in combustion, its PDF has been examined. This examination extends previous gas or liquid scalar dissipation studies into the realm of two-phase flows. Visualization of the PDF revealed that the filamentary aspect exhibited in experiments with gaseous or liquid flows still prevails, but that the contours are here considerably more convoluted than those obtained for the passive scalars of the experiments; notably, the scalar is here active, as it results from drop evaporation. Plots of the PDF show that the PDF is close, but not identical to a Gaussian, with the well-known small but finite

negative skewness, and that when conditioning the ensemble to encompass increasingly larger Reynolds numbers, the PDF becomes closer to a Gaussian; these findings are similar to those obtained by others in SP flows. Compared to SP results, the PDF is here fuller on the side of large scalar products, which is attributed to the local heterogeneities produced by drop/flow interactions.

To summarize, transitional MC flows display significant distinctive features from transitional SC flows having the same initial conditions. Not only are there strong vapor and (if applicable) liquid composition nonuniformities in the layer, but also the turbulent character of the flow and its general dissipative features are different. The conclusion is that neither experiments nor theory conducted with SC flows are good surrogates for a MC flow application. As in pre-transitional simulations, composition effects are amplified with increasing carrier gas temperature, but here additionally the initial carrier gas temperature has a significant impact on the magnitude of the vorticity. Whereas in pre-transitional MC TP flows the regions of high-molar-mass vapor species entirely coincided with those of high vapor-PDF standard deviation, this is no longer the case.

Current effort is now devoted to *a priori* and *a posteriori* investigations, so as to reduce the large computational time of DNS and replace DNS with computationally-efficient Large Eddy Simulations, akin to the studies of Leboissetier, Okong'o & Bellan (2005).

Appendix A. Calculation of the heat flux portion due to transport of molar fluxes

Details of the heat flux in equation 2.7 are as follows:

$$\alpha_1(T) = R_u A_p (A_b - T) - \Delta s_{\mathrm{lg}} A_b \tag{A 1}$$

$$\alpha_2(T) = (C_{p,a} - R_u B_p) T + R_u (A_b B_p + A_c B_b) - \Delta s_{\mathrm{lg}} B_b - C_l A_b \tag{A 2}$$

$$\alpha_3 = B_b [R_u B_p - C_l] \tag{A 3}$$

where $C_{p,a} = \gamma_{ther,a} R_u / (\gamma_{ther,a} - 1) m_a$ (kJ/(kg K)) is the air heat capacity at constant pressure, $m_a = 29$ kg/kmol, $\gamma_{ther,a} = 1.4$ is the ratio of gas heat capacities, $\Delta s_{\mathrm{lg}} = mL_v/T_b$ where L_v is the latent heat and T_b is the normal boiling point, $R_u = 8.3142$ (kJ/(kmol K)) and

$$C_p(m) = (A_p + B_p m) R_u / m \quad \text{in (kJ/(kgK))}, \tag{A 4}$$

is the gas heat capacity where $A_p = 2.465 - 1.144 \times 10^{-2} T_r + 1.759 \times 10^{-5} T_r^2 - 5.972 \times 10^{-9} T_r^3$ and $B_p = -0.03561 + 9.367 \times 10^{-4} T_r - 6.030 \times 10^{-7} T_r^2 + 1.324 \times 10^{-10} T_r^3$ (see Chou & Prausnitz (1986)) with the reference temperature T_r being that of.Miller, Harstad & Bellan (1998). Following Tamim & Hallett (1995), $C_l = 2.26 - 2.94 \times 10^{-3} T_{r,d} + 9.46 \times 10^{-6} T_{r,d}^2$ (kJ/kgK) where $T_{r,d} = T_r$. Constants A_b and B_b are given in §2.2.

More details and transport property values are given in Appendix A of Le Clercq & Bellan (2005).

Acknowledgements

This study was conducted at the Jet Propulsion Laboratory (JPL), California Institute of Technology (Caltech), under the partial sponsorship of the Donors of The Petroleum Research Fund administered by the American Chemical Society through a grant (to JB) for Caltech Post Doctoral Fellow support and the U.S. Department of Energy under an

agreement with the National Aeronautics and Space Administration. The authors wish to thank Dr. Kenneth G. Harstad of JPL for useful discussions. Computational resources were provided by the supercomputing facility at JPL.

REFERENCES

ARIAS-ZUGASTI, M & ROSNER, D. E. 2003 Multicomponent fuel droplet vaporization and combustion using spectral theory for a continuous mixture. *Combustion and Flame* **135**, 271-284.

BARLOW, R. S. AND KARPETIS, A. N. 2004a Scalar length scales and spatial averaging effects in turbulent piloted methane/air jet flames. *Proc. Comb. Institute* **30**, 671-678.

BARLOW, R. S. AND KARPETIS, A. N. 2004b Measurements of scalar variance, scalar dissipation, and length scales in turbulent piloted methane/air jet flames. *Flow, Turbulence and Combustion* **72**, 427-448.

BATCHELOR, G. K. 1967 *The theory of homogeneous turbulence*, Cambridge University Press

BAUM, M., POINSOT T. J. & LELE S. K.1994 Accurate boundary conditions for multicomponent reactive flows. *J. Comp. Phys.* **116**, 247-261.

BOIVIN, M., SIMONIN, S. & SQUIRES, K. D. 1988 Direct numerical simulation of turbulence modulation by particles in isotropic turbulence. *J. Fluid Mech.* **375**, 235-263.

BUCH, K. A. & DAHM, W. J. A. 1996 Experimental study of the fine-scale structure of conserved scalar mixing in turbulent shear flows. Part 1. $Sc \gg 1$. *J. Fluid Mech.* **317**, 51-71.

BUCH, K. A. & DAHM, W. J. A. 1996 Experimental study of the fine-scale structure of conserved scalar mixing in turbulent shear flows. Part 2. $Sc \approx 1$. *J. Fluid Mech.* **364**, 1-29.

CHORIN A. J. 1991 *Vorticity and Turbulence*, Applied Mathematics Science **103**, Springer.

CHOU G. F. & PRAUSNITZ J. M. 1986 Adiabatic flash calculations for continuous or semicontinuous mixtures using an equation of state. *Fluid Phase Equilibria* **30**, 75-82.

COTTERMAN, R. L., BENDER R. & PRAUSNITZ J. M. 1985 Phase equilibria for mixtures containing very many components. Development and application of continuous thermodynamics for chemical process design. *Ind. Eng. Chem. Process Des. Dev.* **24**, 194–203.

EDWARDS, T. & MAURICE L. Q. 2001 Surrogate mixtures to represent complex aviation and rocket fuels. *J. Propul. Power* **17**(2), 461-466.

EDWARDS T. 2002 private comm.

GAL-OR, B., CULLINAN, JR., H. T. & GALLI, R. 1975 New thermodynamic-transport theory for systems with continuous component density distributions. *Chem. Eng. Sci.* **30**, 1085-1092.

GOLDSTEIN, H. L. & SIEGMUND, C. W. 1976 Influence of heavy fuel oil composition and boiler combustion conditions on particulate emissions. *Environmental Science and Technology* **10**(12), 1109-1114.

GROENZIN, H. & MULLINS, O. C. 2000 Molecular size and structure of asphaltenes from various sources. *Energy and Fuel* **14**, 677-684.

HALLETT W. L. H. 2000 A simple model for the vaporization of droplets with large numbers of components. *Combust. Flame* **121**, 334-344.

HARSTAD, K. 2005 Trend analysis for atmospheric hydrocarbon partitioning using continuous thermodynamics, in press, *J. Atmospheric Sci.*

HARSTAD, K. & BELLAN, J. 2004 Modeling evaporation of Jet A, JP-7 and RP-1 drops at 1 to 15 bars. *Combust. Flame* **137**(1-2), 163-177.

HARSTAD, K. G., LE CLERCQ, P. C. & BELLAN, J. 2003 A statistical model of multicomponent-fuel drop evaporation for many-droplet gas-liquid flow simulations. *AIAA J.* **41**(10), 1858-1874.

KARPETIS, A. N. AND BARLOW, R. S. 2002 Measurements of scalar dissipation in a turbulent piloted methane/air flame. *Proc. Comb. Institute* **29**, 1929-1936.

KARPETIS, A. N. AND BARLOW, R. S. 2004 Measurements of flame orientation and scalar dissipation in turbulent partially premixed methane flames. *Proc. Comb. Institute* **30**, 663-670.

KARPETIS, A. N. SETTERSTEN, T. B., SCHEFER, R. W. AND BARLOW, R. S. 2004 Laser imaging system for determinination of three-dimensional scalar gradients in turbulent flames. *Optics Letters* **29**(4), 355-357.

KENNEDY, C. & CARPENTER, M. 1994 Several new numerical methods for compressible shear layer simulations. *Applied Numerical Mathematics* **14**, 397–433.

KOTHNUR, P. S. AND CLEMENS, N. T. 2001 Experimental investigation of the relationship between strain and scalar dissipation in gas-phase turbulent jets. Paper AIAA 2001-1023.

LANDIS, R. B. & MILLS, A. F., 1974 Effect of internal diffusional resistence on the evaporation of binary droplets. *5th Int. Heat Transfer Conference* **4**, 345-349.

LEBOISSETIER, A., OKONG'O, N. A. & BELLAN, J. 2005 Consistent Large Eddy Simulation of a temporal mixing layer laden with evaporating drops. Part 2: *A posteriori* modeling. *J. Fluid Mech.* **523**, 37-78.

LE CLERCQ, P. C. & BELLAN, J. 2004 Direct numerical simulation of a transitional temporal mixing layer laden with multicomponent-fuel evaporating drops using continuous thermodynamics *Physics of Fluids* **16**(6), 1884-1907.

LE CLERCQ, P. C. & BELLAN, J. 2005 Direct numerical simulation of gaseous mixing layers laden with multicomponent-liquid drops: Liquid-specific effects. *J. Fluid Mech.* **533**, 57-94.

LIPPERT, A. M. & REITZ, R. D. 1997 Modeling of multicomponent fuels using continuous distributions with application to droplet evaporation and sprays. SAE paper 97FL-468.

MASHAYEK, F. 1998a Droplet-turbulence interactions in low-Mach-number homogeneous shear two-phase flows. *J. Fluid Mech.* **367**, 163–203.

MASHAYEK, F. 1998b Direct numerical simulations of evaporating droplet dispersion in forced low-Mach-number turbulence. *International Journal of Heat and Mass Transfer* **41**(17), 2601–2617.

MASHAYEK, F. & JABERI, F. A. 1999 Particle dispersion in forced isotropic low-Mach-number turbulence. *International Journal of Heat and Mass Transfer* **42**, 2823–2836.

MASON, S. D., CHEN, J. H. AND IM, H. G. 2002 Effects of unsteady scalar dissipation rate on ignition of non-premixed hydrogen/air mixtures in counterflow. *Proc. Comb. Inst.*, **29**, 1629-1636.

MILLER, R. S., HARSTAD, K. & BELLAN, J. 1998 Evaluation of equilibrium and non-equilibrium evaporation models for many-droplet gas-liquid flow simulations. *Int. J. Multiphase Flow* **24**, 1025-1055.

MILLER, R. S. & BELLAN, J. 1999 Direct numerical simulation of a confined three-dimensional

gas mixing layer with one evaporating hydrocarbon-droplet laden stream. *J. Fluid Mech.* **384**, 293-338.

MILLER, R. S. & BELLAN, J. 2000 Direct numerical simulation and subgrid analysis of a transitional droplet laden mixing layer. *Phys. Fluids* **12**(3), 650-671.

MOSER, R. D. & ROGERS, M. M. 1991 Mixing transition and the cascade to small scales in a plane mixing layer. *Phys. Fluids A* **3**, 1128–1134.

OKONG'O, N. A. & BELLAN, J. 2004 Consistent Large Eddy Simulation of a temporal mixing layer laden with evaporating drops. Part I: Direct Numerical Simulation, formulation and *a priori* analysis. *J. Fluid Mech.* **499**, 1-47.

POINSOT, T. J. & LELE, S. K. 1992 Boundary conditions for direct simulations of compressible viscous flows. *J. Comp. Phys.* **101**, 104-129.

PROBST, D. M. & GHANDI, J. B. 2003 An experimental study of spray mixing in a direct injection engine. *Int. J. Engine Res.* **4**(1), 27-45.

RÄTZSCH, M. T. & KEHLEN, H. 1983 Continuous thermodynamics model of complex mixtures. *Fluid Phase Equilibria* **14**, 225-234.

RÉVEILLON, J. & VERVISCH, L. 2000 Spray vaporization in nonpremixed turbulent combustion modeling: A single drop model. *Combustion and Flame* **121**, 75–90.

SHEU, E. Y. 2002 Petroleum asphaltene - properties, chracterization, and issues. *Energy and Fuels* **16**, 74-82.

SQUIRES, K. D. & EATON, J. K. 1991 Preferential concentration of particles by turbulence. *Phys. Fluids* A **3**, 1169-1178.

SU, L. K. & CLEMENS, N. T. 1999 Planar measurements of a full three dimensional scalar dissipation rate in gas phase turbulent flows. *Exp. In Fluids* **27**, 507-521.

SU, L. K. & CLEMENS, N. T. 2003 The structure of fine-scale scalar mixing in gas-phase planar turbulent jets. *J. Fluid Mech.* **488**, 1-29.

TAMIM, J. & HALLETT, W. L. H. 1995 A continuous thermodynamics model for multicomponent droplet vaporization. *Chem. Eng. Sci.* **50**, 2933-2942.

TENNEKES, H. & LUMLEY, J. L. 1972 *A first course in turbulence*, MIT Press.

TONG, C. & WARHAFT, Z. 1995 Passive scalar dispersion and mixing in a turbulent jet. *J. Fluid Mech.* **292**, 1-38.

WARHAFT, Z. 2000 Passive scalars in turbulent flows. *Ann. Rev. Fluid Mech.* **32**, 203-240.

WHITSON, C. H. 1983 Characterizing hydrocarbon plus fractions. *Soc. Pet. Eng. J.* **23**, 683-694.

WILLIAMS, F. A. 1965 *Combustion Theory* Addison-Wesley.

Case	fuel	T_0	ML_0	ρ_l	Re_0	$X^l_{v,0}$	$\{\{D_0\}\}$ $\times 10^5$	$\theta_{l,0}$ / $\sigma_{l,0}$	$\theta_{v,0}$ / $\sigma_{v,0}$	N_0 $\times 10^{-3}$
die375ML0R5	diesel	375	0	NA	500	$X^u_{v,0}$	NA	NA	140.0 / 28.0	NA
die375ML0R5X	diesel	375	0	NA	500	10^{-1}	NA	NA	140.0 / 28.0	NA
die375ML0R6	diesel	375	0	NA	600	$X^u_{v,0}$	NA	NA	140.0 / 28.0	NA
die375ML0R6X	diesel	375	0	NA	600	10^{-1}	NA	NA	140.0 / 28.0	NA
die375ML2R2	diesel	375	0.2	828	200	$X^u_{v,0}$	12.02	185.0 / 43.0	140.0 / 28.0	670
die400ML2R2	diesel	400	0.2	828	200	$X^u_{v,0}$	11.64	185.0 / 43.0	140.0 / 28.0	690
die375ML2R5*	diesel	375	0.2	828	500	$X^u_{v,0}$	7.601	185.0 / 43.0	140.0 / 28.0	2586
die375ML5R5	diesel	375	0.5	828	500	$X^u_{v,0}$	7.601	185.0 / 43.0	140.0 / 28.0	6451
die400ML2R5	diesel	400	0.2	828	500	$X^u_{v,0}$	7.359	185.0 / 43.0	140.0 / 28.0	2670
jetA375ML2R5	Jet A	375	0.2	800	500	$X^u_{v,0}$	7.732	161.0 / 29.7	131.4 / 22.4	2543
jetA400ML2R5	Jet A	400	0.2	800	500	$X^u_{v,0}$	7.487	161.0 / 29.7	131.4 / 22.4	2626
rp1375ML2R5	RP-1	375	0.2	800	500	$X^u_{v,0}$	7.732	165.2 / 17.7	153.5 / 14.8	2600
rp1400ML2R5	RP-1	400	0.2	800	500	$X^u_{v,0}$	7.487	165.2 / 17.7	153.5 / 14.8	2626
jp7375ML2R5	JP-7	375	0.2	800	500	$X^u_{v,0}$	7.732	167.1 / 19.2	153.7 / 15.7	2541
jp7400ML2R5	JP-7	400	0.2	800	500	$X^u_{v,0}$	7.487	167.1 / 19.2	153.7 / 15.7	2626

TABLE 1. Initial conditions. T_0 in K, ρ_l in kg/m^3, D_0 in m and mean molar mass and standard deviation in kg/kmol. In all simulations, $M_{c,0}$=0.35, $\delta_{\omega,0}$=6.859$\times 10^{-3}$m, $\{\{St_0\}\}$=3 and $\{\{(St_0 - \{\{St_0\}\})^2\}\}^{1/2}$=0.5, $T_{d,0}$=345K, $X^u_{v,0} = 10^{-4}$, γ=86kg/kmol for diesel, γ=41kg/kmol for Jet A, and γ=93kg/kmol for RP1 and JP7. For $\mathrm{Re}_0 = 200$ the grid is 200$\times$224$\times$120, for $\mathrm{Re}_0 = 500$ the grid is 360$\times$400$\times$216 and for $\mathrm{Re}_0 = 600$ the grid is 432$\times$480$\times$260. The baseline case is indicated by a superscript asterisk.

Case	CPU-hours	t^*_{tr}	$\mathrm{Re}_{m,tr}$	CPU-hours at t^*_{tr}
die375ML0R5	793	120	1332	793
die375ML0R5X	1083	120	1343	1083
die375ML0R6	2260	110	1482	2072
die375ML0R6X	2802	110	1483	2568
die375ML2R5*	1680	100	1386	1400
die375ML5R5	2533	100	1336	2111
die400ML2R5	1706	100	1396	1422
jetA375ML2R5	9331	100	1365	7776
jetA400ML2R5	1700	100	1375	1417
rp1375ML2R5	1679	100	1377	1399
rp1400ML2R5	1694	100	1371	1412
jp7375ML2R5	1662	100	1381	1385
jp7400ML2R5	1701	100	1373	1417

TABLE 2. Global characteristics of simulations at transition. t^*_{tr} is the nondimensional time at transition and $\mathrm{Re}_{m,tr}$ is the momentum-thickness based Reynolds number at transition. Except for the jetA375ML2R5 simulation which was perfoemd on a SGI Origin 2000 platform (64, R12000, 300MHz processors), all other simulations were conducted on an Altix 3000 machine (32, Intel Itanium2, 900MHz processors).

	$\nearrow \{\{A^{\mathcal{I}}\}\}$	quantity averaged over all N drops in the volume
$A \xrightarrow{\mathcal{I}} A^{\mathcal{I}}$	$\rightarrow \{A^{\mathcal{I}}\}$	quantity averaged over N_{x_2} drops in homogeneous (x_1, x_3) planes
	$\searrow [A^{\mathcal{I}}]_c$	quantity averaged over drops in the discretization volume $\Delta x_1 \times \Delta x_3 \times \Delta x_3$

TABLE 3. Definition of several types of drop-related averaging for a quantity A defined at grid nodes.

	die375ML0R5		die375ML0R6		die375ML0R5X		die375ML0R6X	
Term	Average	r.m.s.	Average	r.m.s.	Average	r.m.s.	Average	r.m.s.
g_{visc}	1178	2125	1141	2198	1230	2236	1307	2611
g_{temp}	12	31	10	26	11	29	11	28
g_{mass}	0	0	0	0	87	272	81	280
g	1190	2135	1151	2208	1328	2325	1399	2693

TABLE 4. Global entropy production for die375ML0R5, die375ML0R6, die375ML0R5X and die375ML0R6X at t^*_{tr}. Units are $\mathrm{Wm^{-3}K^{-1}}$.

	die375ML2R5				die375ML5R5				die400ML2R5			
	Volumetric				Volumetric				Volumetric			
Term	Average	r.m.s.	% >0	% <0	Average	r.m.s.	% >0	% <0	Average	r.m.s	% >0	% <0
g_{III}	7307	24695	57	17	16097	42372	70	9	8423	30536	55	22
$g^*_{I,chpot}$	-11479	50145	28	47	-23045	89873	28	51	-12203	58544	29	46
g_{visc}	3296	7248	100	0	3479	7543	100	0	3314	7296	100	0
g_{II}	152	4612	37	38	575	9647	42	37	26	3767	35	39
g_{mass}	122	447	100	0	155	632	100	0	160	601	100	0
g_{temp}	138	426	100	0	176	599	100	0	240	731	100	0
$g_{I,kine}$	30	232	47	28	71	365	51	28	27	281	46	29
g^*	-435	24917	78	22	-2492	45894	72	28	-14	27593	80	20

TABLE 5. Volumetric entropy production for die375ML2R5, die375ML5R5 and die400ML2R5 at t^*_{tr}. Units are $\mathrm{Wm^{-3}K^{-1}}$.

	jetA375ML2R5				jetA400ML2R5				rp1375ML2R5			
	Volumetric				Volumetric				Volumetric			
Term	Average	r.m.s.	% >0	% <0	Average	r.m.s.	% >0	% <0	Average	r.m.s.	% >0	% <0
g_{III}	10018	35523	58	18	10016	37759	56	19	12383	39873	61	15
$g^*_{I,chpot}$	-15351	63611	25	51	-14524	64159	26	50	-19090	68136	19	57
g_{visc}	3288	7310	100	0	3228	7235	100	0	3373	7480	100	0
g_{II}	-6	3527	34	41	-95	2744	27	48	-28	3574	31	45
g_{mass}	201	770	100	0	254	942	100	0	197	745	100	0
g_{temp}	182	577	100	0	294	943	100	0	153	469	100	0
$g_{I,kine}$	43	297	51	25	38	321	50	26	63	333	57	19
g^*	-1625	27387	77	23	-1625	27387	77	23	-2949	27565	72	28

TABLE 6. Volumetric entropy production for jetA375ML2R5, jetA400ML2R5 and rp1375ML2R5 at t^*_{tr}. Units are $\mathrm{Wm^{-3}K^{-1}}$.

	die375ML2R5				die375ML5R5				jetA375ML2R5			
	Drop-ensemble				Drop-ensemble				Drop-ensemble			
Term	Average	r.m.s.	% >0	% <0	Average	r.m.s.	% >0	% <0	Average	r.m.s	% >0	% <0
g_{III}	27210	63584	64	36	42611	97944	82	18	38499	100234	63	37
$g^*_{I,chpot}$	-45172	134423	59	41	-59245	209757	60	40	-61279	184177	52	48
g_{visc}	2308	5808	100	0	2560	6961	100	0	2199	5589	100	0
g_{II}	190	12785	48	52	455	25300	52	48	-155	9413	48	52
g_{mass}	152	543	99	1	152	748	99	1	268	1045	99	1
g_{temp}	288	848	99	1	280	1156	99	1	385	1190	99	1
$g_{I,kine}$	99	542	41	59	134	635	40	60	143	731	48	52
g^*	-14926	66548	66	34	-13053	106403	71	29	-19939	79451	64	36

TABLE 7. Drop-ensemble-based entropy production for die375ML2R5, die375ML5R5 and jetA375ML2R5 at t^*_{tr}. Units are $\mathrm{Wm^{-3}K^{-1}}$.

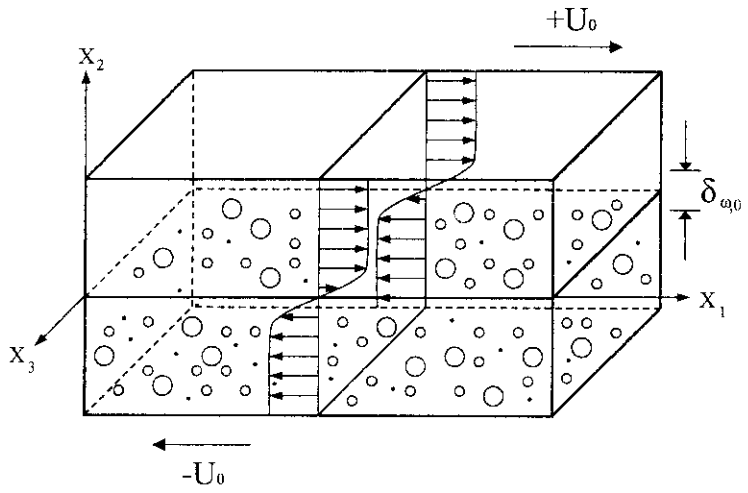

FIGURE 1. Mixing layer configuration.

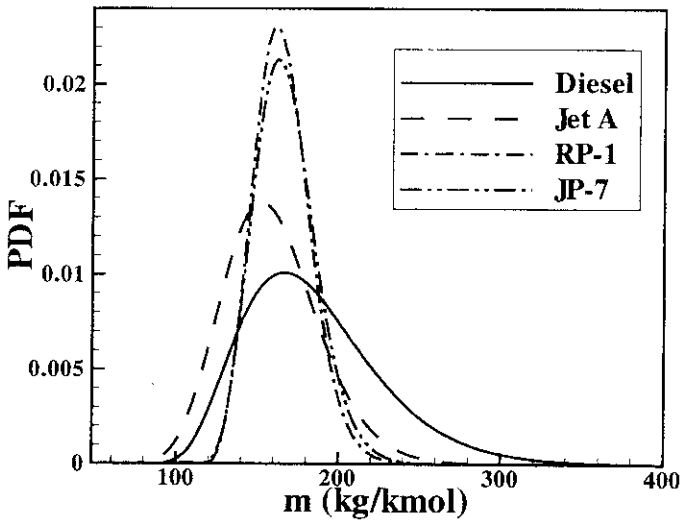

FIGURE 2. Liquid initial PDF for each fuel.

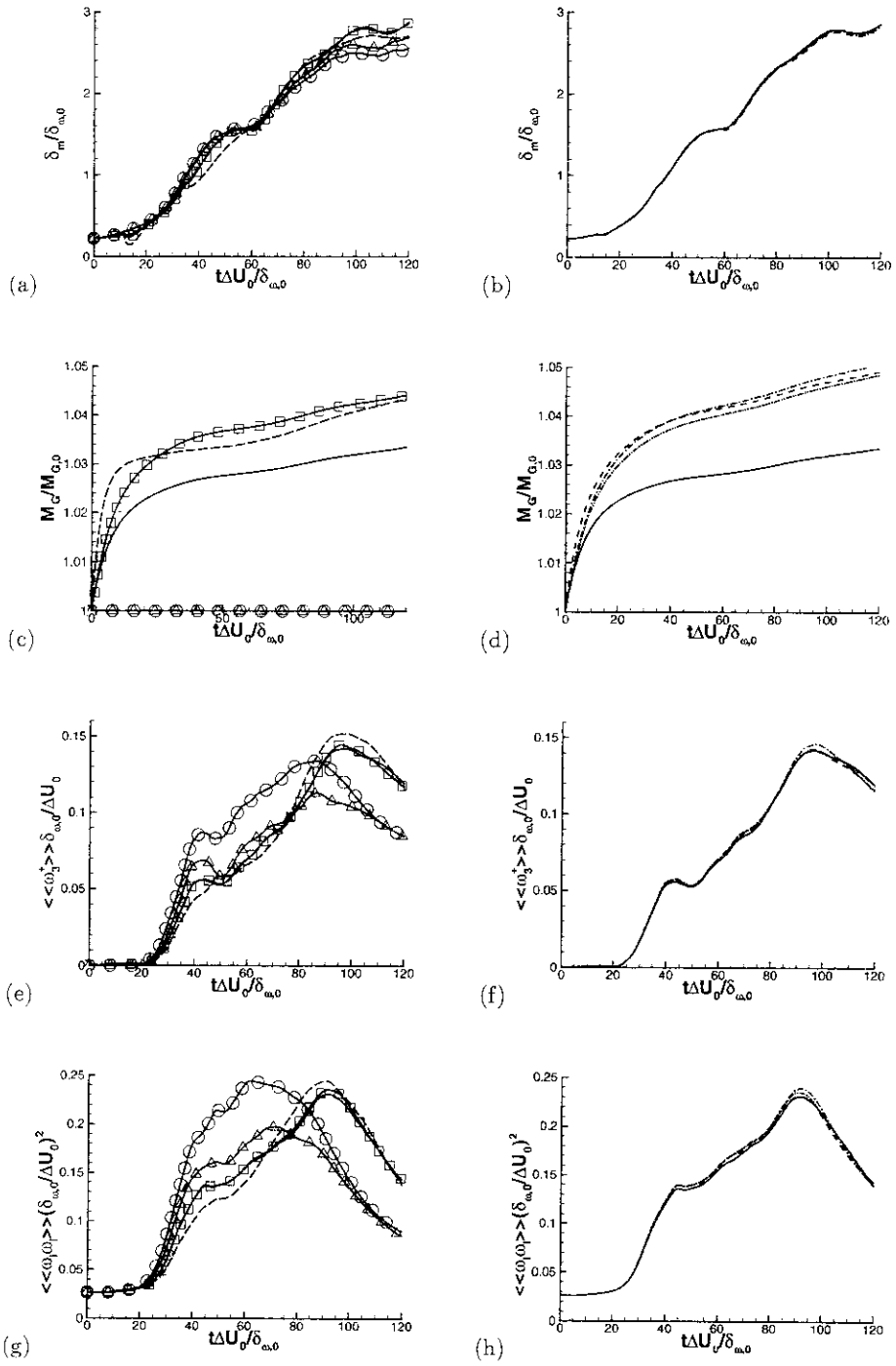

FIGURE 3. Global layer characteristics: (a) $\delta_m/\delta_{\omega,0}$ for die375ML0R5 —△—, die375ML0R6 —○—, die375ML2R5 ——, die375ML5R5 — — —, and die400ML2R5 —□—; (b) $\delta_m/\delta_{\omega,0}$ for die375ML2R5, jetA375ML2R5 – – –, rp1375ML2R5 – · – · –, and jp7375ML2R5 – ·· · ·· –; (c) $M_G/M_{G,0}$ for all (a) simulations; (d) $M_G/M_{G,0}$ for all (b) simulations; (e) $\langle\langle\omega_3^+\rangle\rangle\delta_{\omega,0}/\Delta U_0$ for all (a) simulations; (f) $\langle\langle\omega_3^+\rangle\rangle\delta_{\omega,0}/\Delta U_0$ for all (b) simulations; (g) $\langle\langle\omega_i\omega_i\rangle\rangle(\delta_{\omega,0}/\Delta U_0)^2$ for all (a) simulations; (h) (g) $\langle\langle\omega_i\omega_i\rangle\rangle(\delta_{\omega,0}/\Delta U_0)^2$ for all (b) simulations.

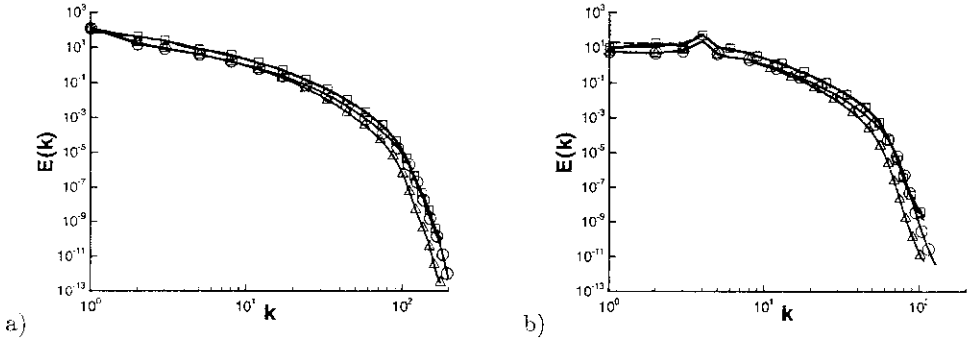

FIGURE 4. One-dimensional u_1 energy spectra, at t^*_{tr} for die375ML0R5, die375ML0R6, die375ML2R5, die375ML5R5 and die400ML2R5: a) streamwise b) spanwise. The curve labels are listed in the figure 3 caption.

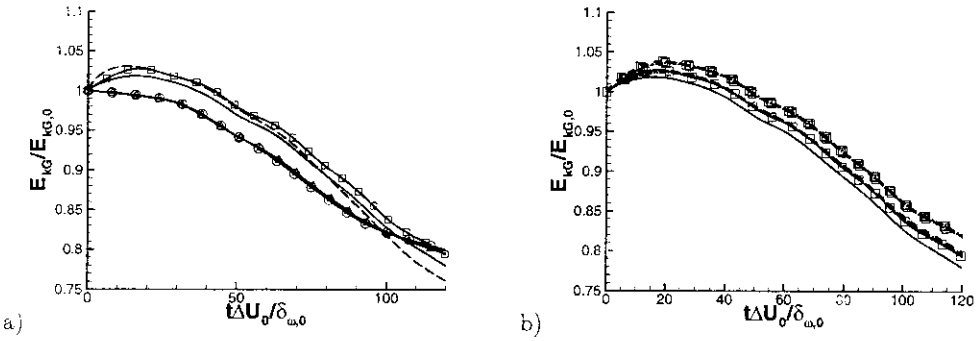

FIGURE 5. Kinetic energy at t^*_{tr} normalized by the total initial gas energy (a) die375ML0R5, die375ML0R6, die375ML2R5, die375ML5R5 and die400ML2R5 (b) die375ML2R5, jetA375ML2R5, rp1375ML2R5, jp7375ML2R5, die400ML2R5, jetA400ML2R5, rp1400ML2R5 and jp7400ML2R5. The curve labels are listed in the figure 3 caption and additionally jetA400ML2R5 - □ –, rp1400ML2R5 – · □ – · □ – and jp7400ML2R5 – ·· □ – ·· □ – .

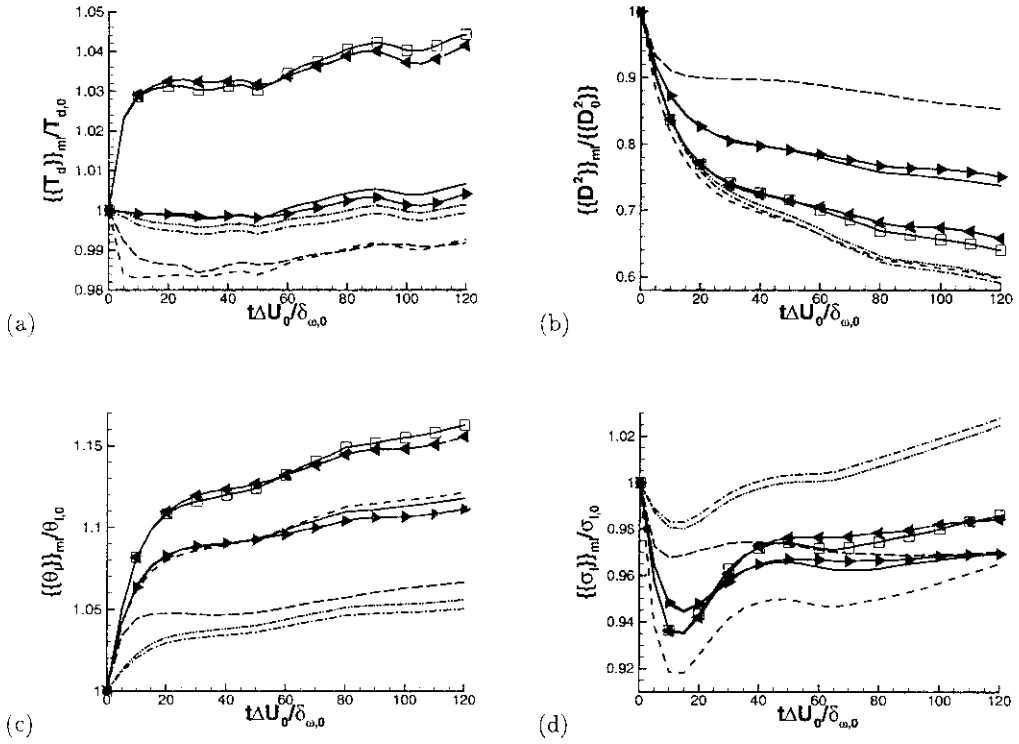

FIGURE 6. Timewise evolution of drop characteristics ensemble averaged in the mixing layer portion of the domain. Legend: die375ML2R2 —▶—, die400ML2R2 —◀—. Other curve labels are listed in the figure 3 caption.

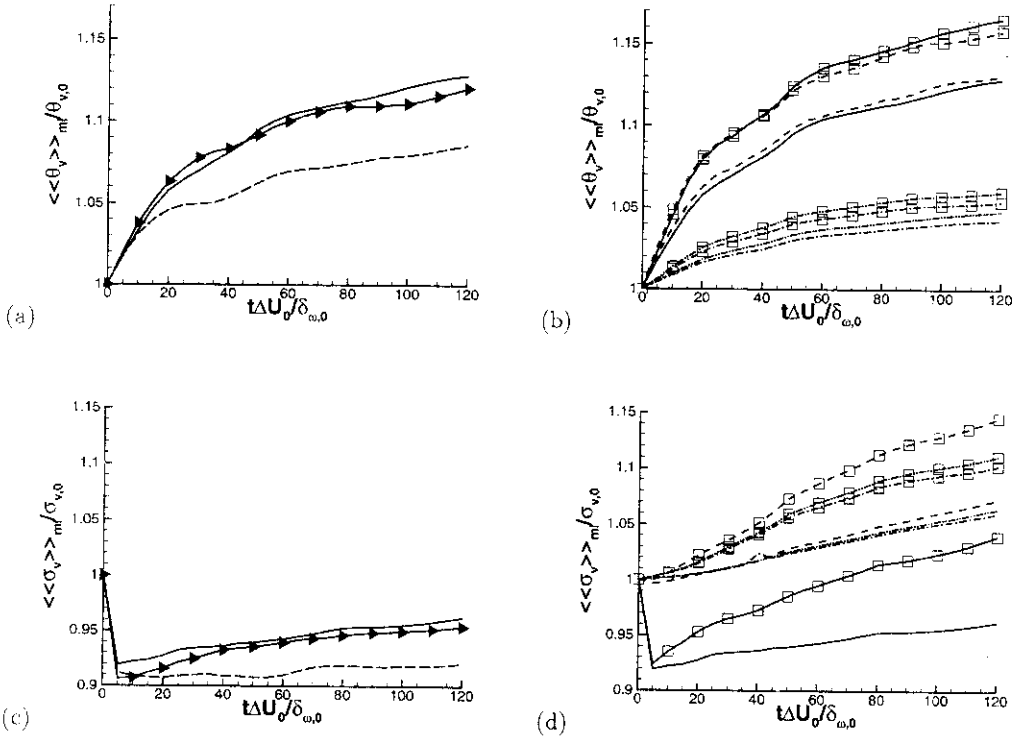

FIGURE 7. Timewise evolution of domain-averaged gas characteristics in the mixing layer. (a,c) die375ML2R2, die375ML2R5 and die375ML5R5, and (b,d) die375ML2R5, die400ML2R5, jetA375ML2R5, jetA400ML2R5, rp1375ML2R5, rp1400ML2R5, jp7375ML2R5 and jp7400ML2R5. Curve labels are listed in the figures 3, 6 and 5 captions.

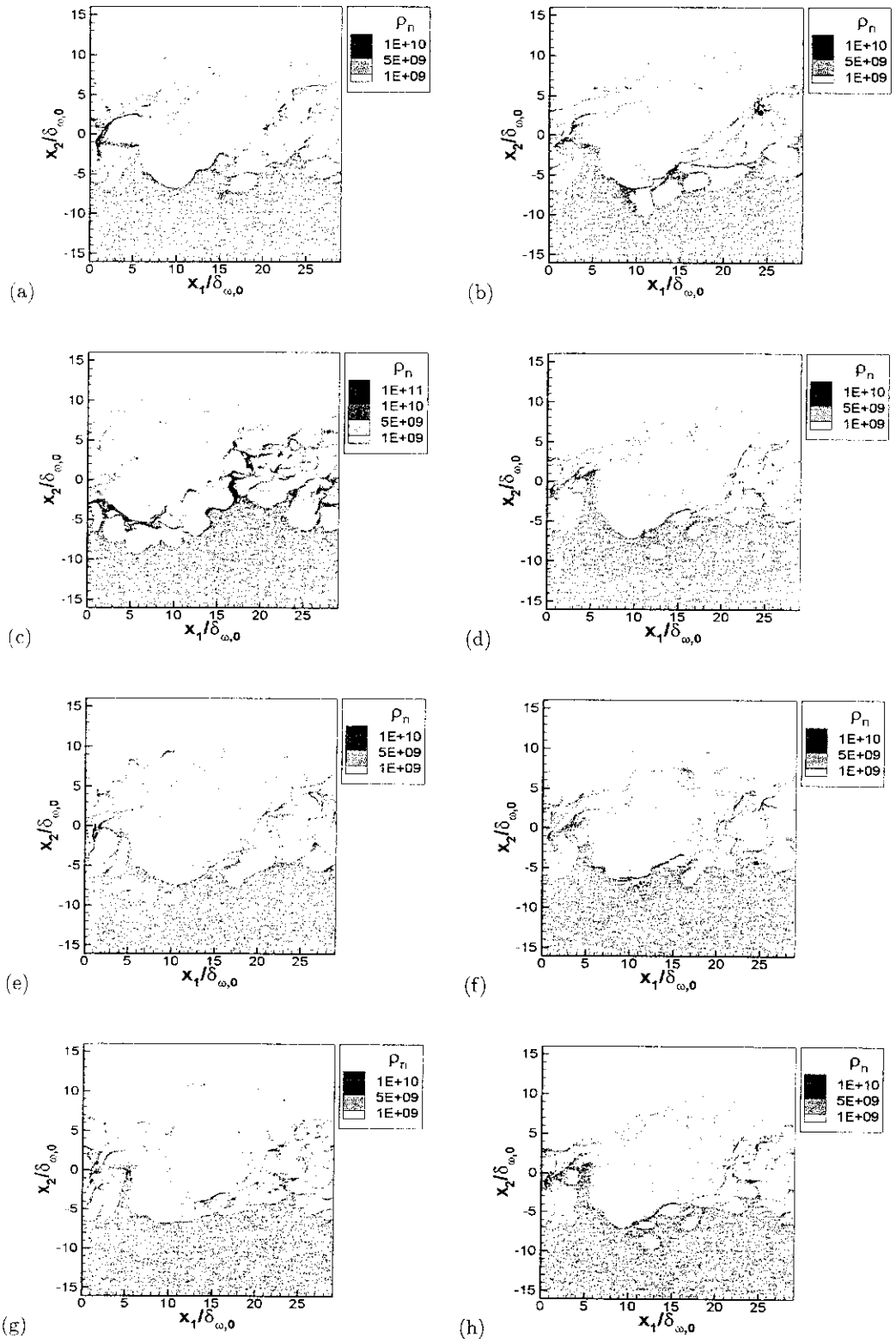

FIGURE 8. Drop number density (m^{-3}) in the between-the-braid plane ($x_3/L_3 = 0.5$) at t^*_{tr}: (a) die375ML2R5, (b) die400ML2R5, (c) die375ML5R5, (d) rp1400ML2R5, (e) jetA375ML2R5, (f) jetA400ML2R5, (g) jp7375ML2R5 and (h) jp7400ML2R5.

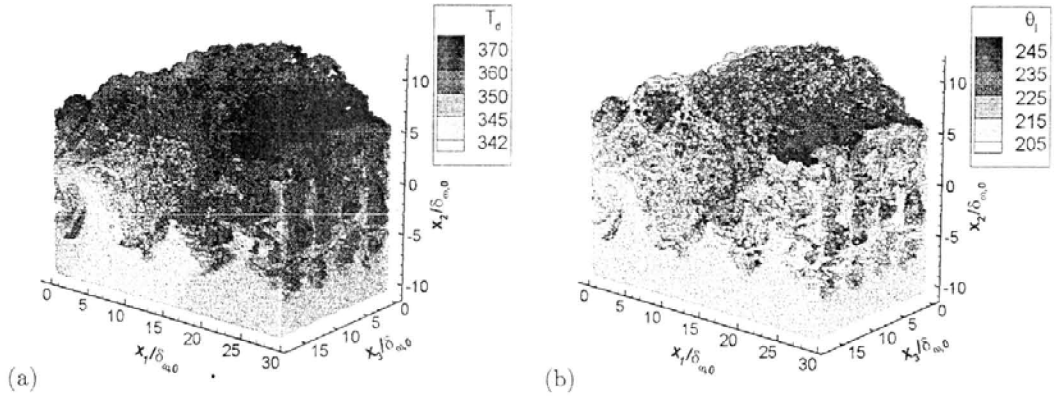

FIGURE 9. Lagrangian plot of all drops at t^*_{tr} for die375ML2R5. (a) T_d and (b) θ_l. The drops are magnified and their volume is not proportional to their size.

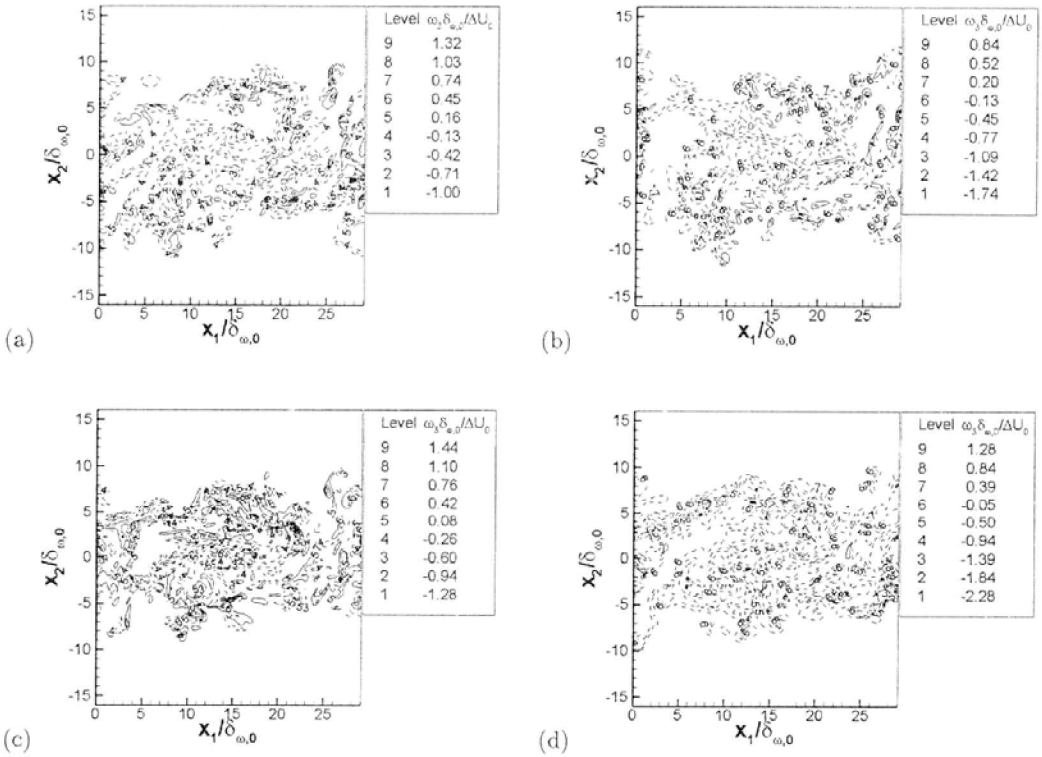

FIGURE 10. Spanwise vorticity in the between-the-braid plane ($x_3/L_3 = 0.5$) at t^*_{tr}: (a) die375ML0R5, (b) die375ML0R5X, (c) die375ML0R6 and (d) die375ML0R6X. Dashed lines represent negative vorticity values.

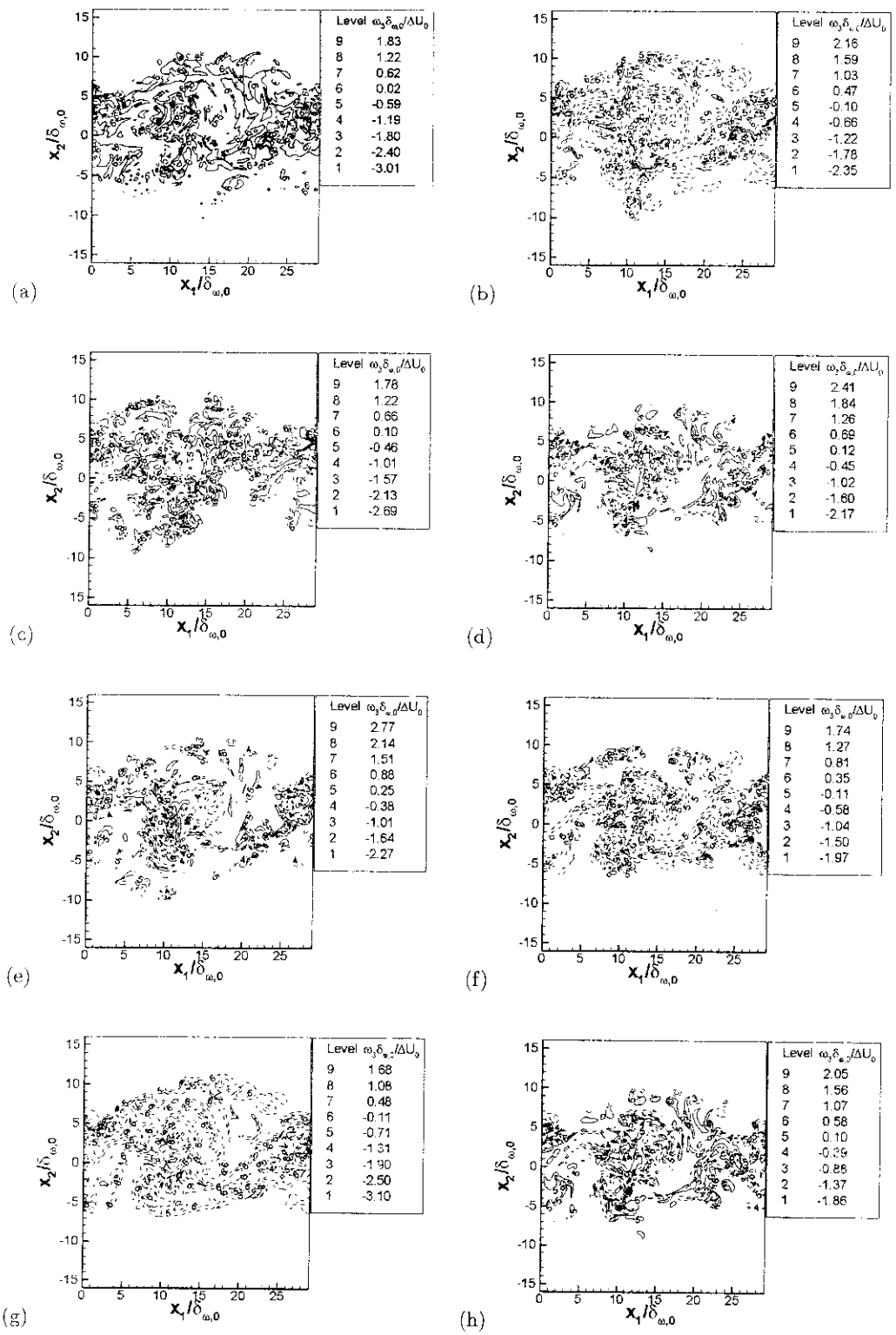

FIGURE 11. Spanwise vorticity in the $x_3/L_3 = 0.5$ plane at t^*_{tr}: (a) die375ML2R5, (b) die400ML2R5, (c) die375ML5R5, (d) rp1400ML2R5, (e) jetA375ML2R5, (f) jetA400ML2R5, (g) jp7375ML2R5 and (h) jp7400ML2R5. Dashed lines represent negative vorticity values.

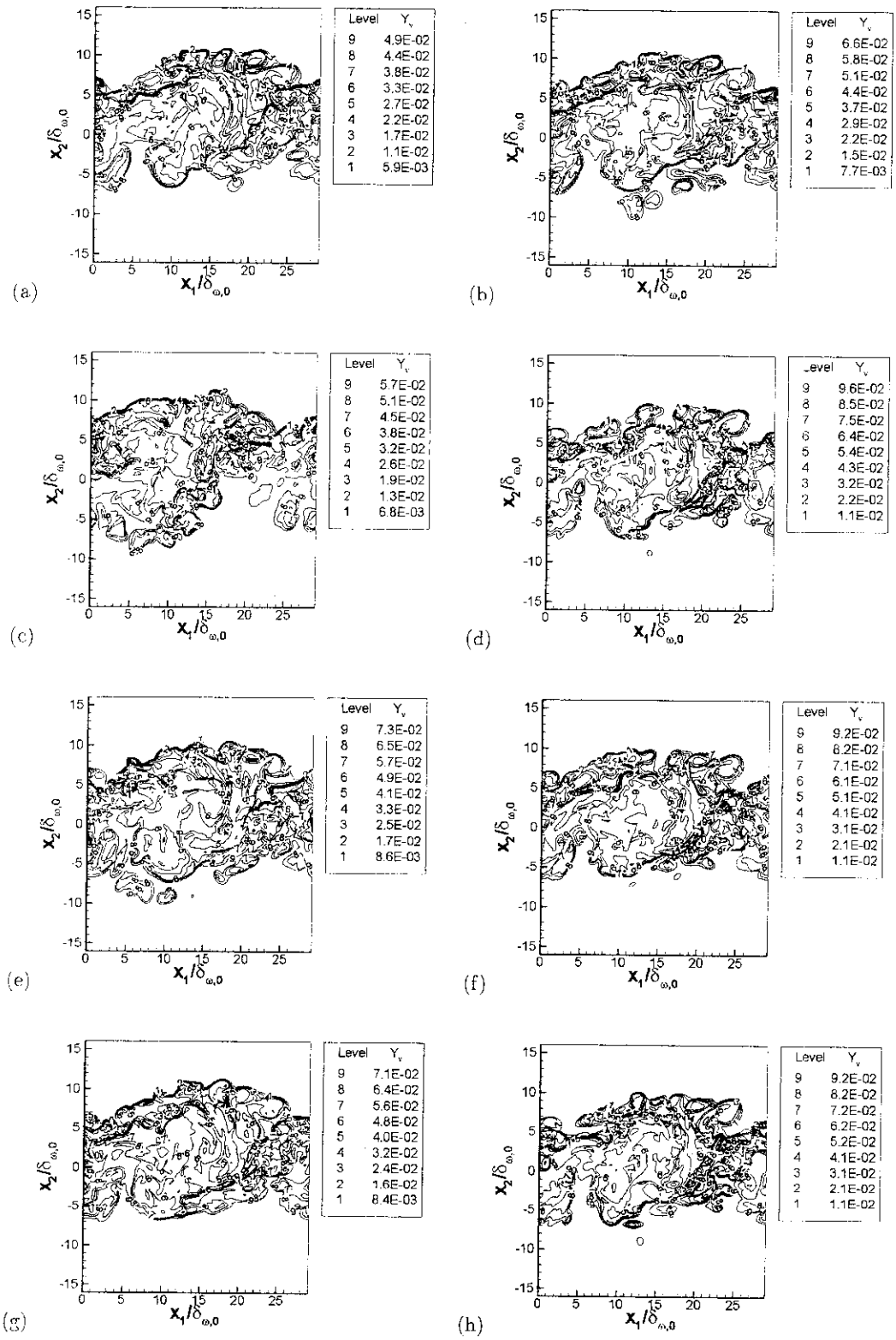

FIGURE 12. Vapor mass fraction in the between-the-braid plane ($x_3/L_3 = 0.5$) at t_{tr}^*: (a) die375ML2R5, (b) die400ML2R5, (c) die375ML5R5, (d) rp1400ML2R5, (e) jetA375ML2R5, (f) jetA400ML2R5, (g) jp7375ML2R5 and (h) jp7400ML2R5.

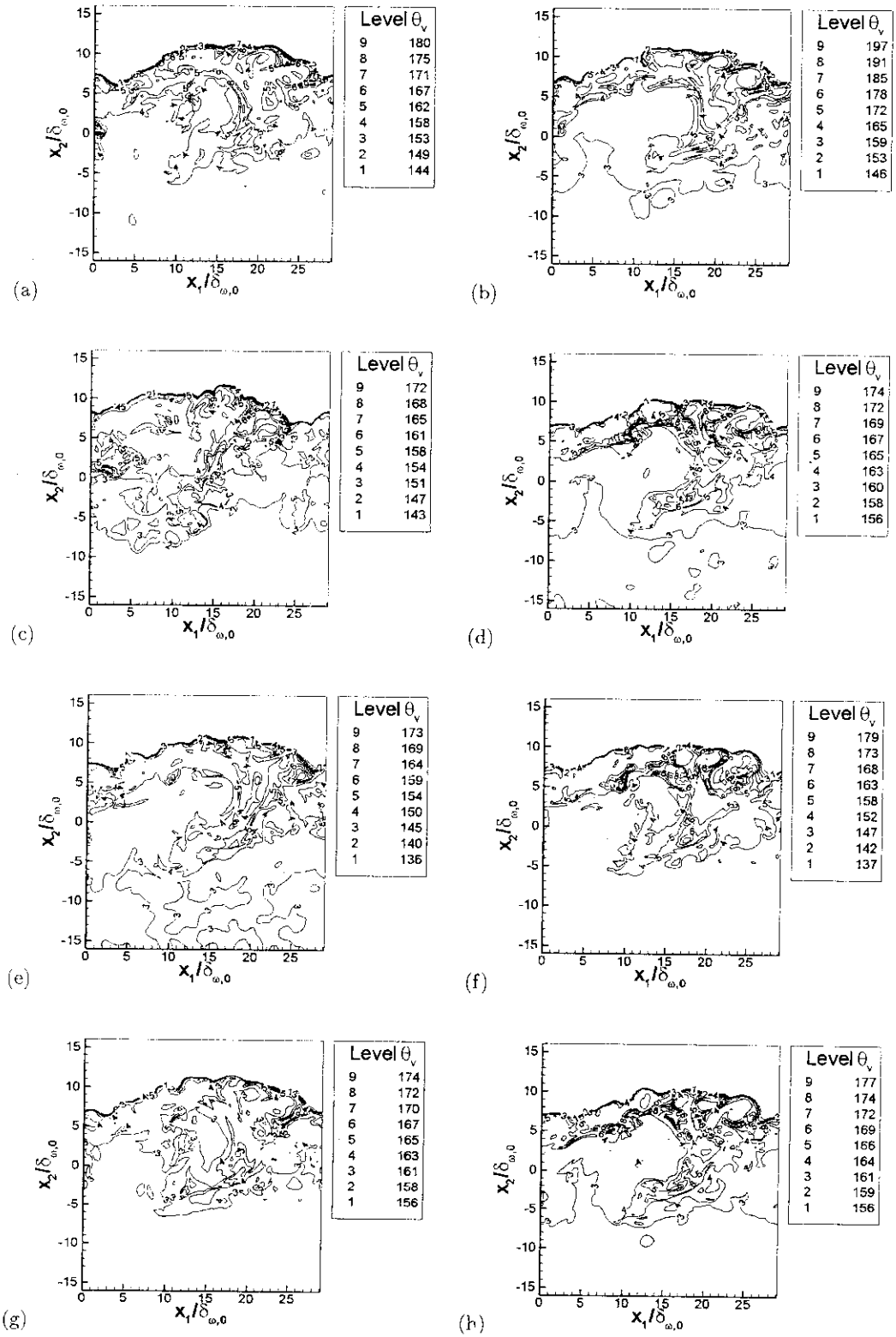

FIGURE 13. Vapor mean molar mass (kg/kmol) in the between-the-braid plane ($x_3/L_3 = 0.5$) at t^*_{tr}: (a) die375ML2R5, (b) die400ML2R5, (c) die375ML5R5, (d) rp1400ML2R5, (e) jetA375ML2R5, (f) jetA400ML2R5, (g) jp7375ML2R5 and (h) jp7400ML2R5.

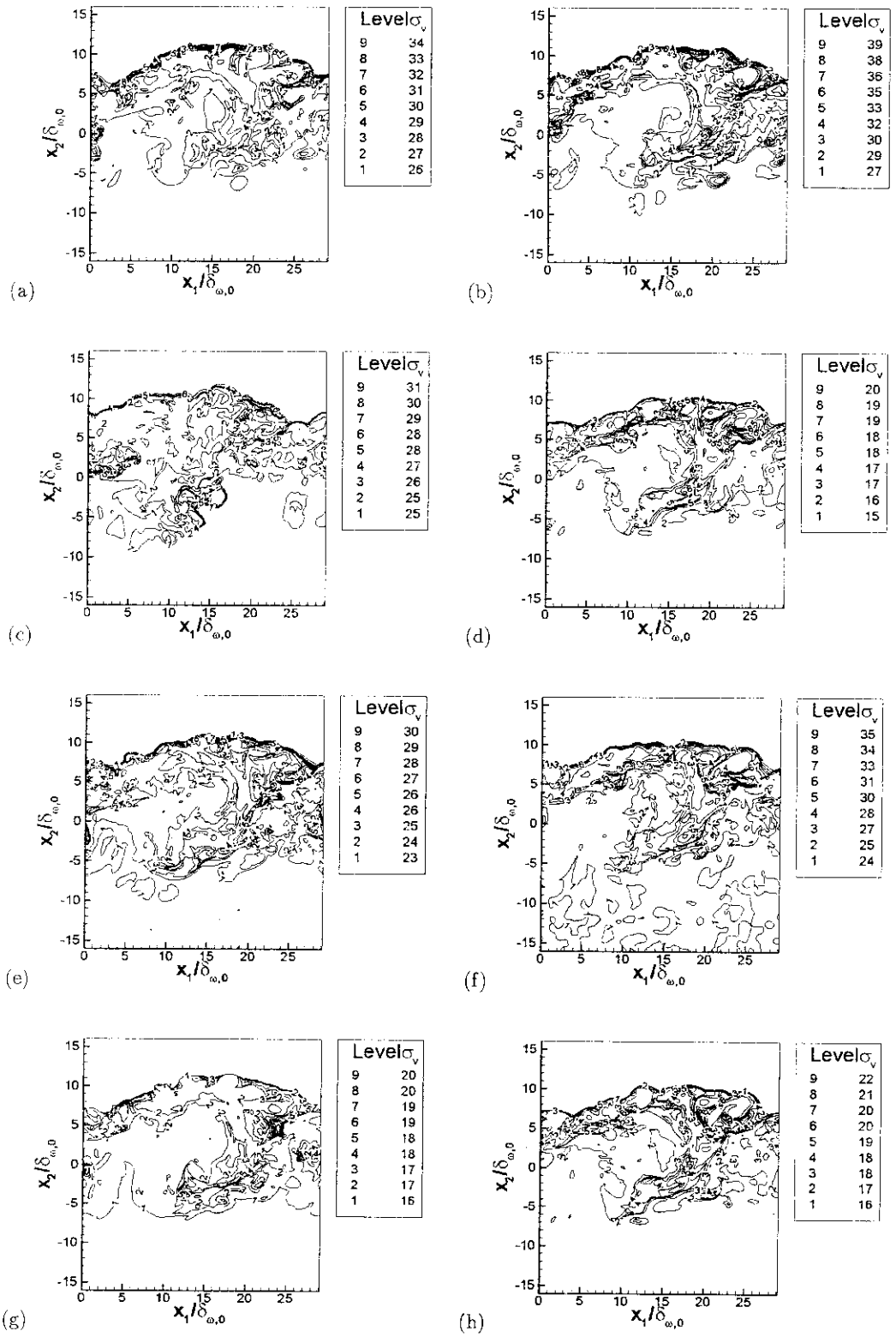

FIGURE 14. Standard deviation of the vapor composition (kg/kmol) in the $x_3/L_3 = 0.5$ plane at t^*_{tr}: (a) die375ML2R5, (b) die400ML2R5, (c) die375ML5R5, (d) rp1400ML2R5, (e) jetA375ML2R5, (f) jetA400ML2R5, (g) jp7375ML2R5 and (h) jp7400ML2R5.

b]

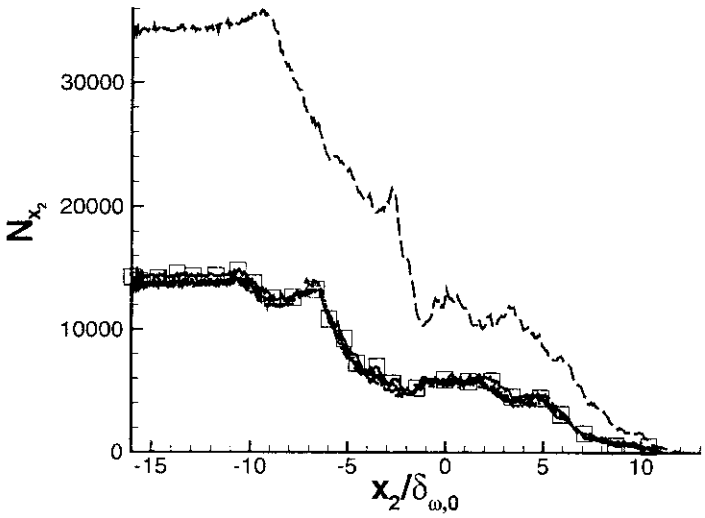

FIGURE 15. Homogeneous (x_1, x_3) plane average number of drops at t^*_{tr}. The curve labels are listed in the figure 3 caption.

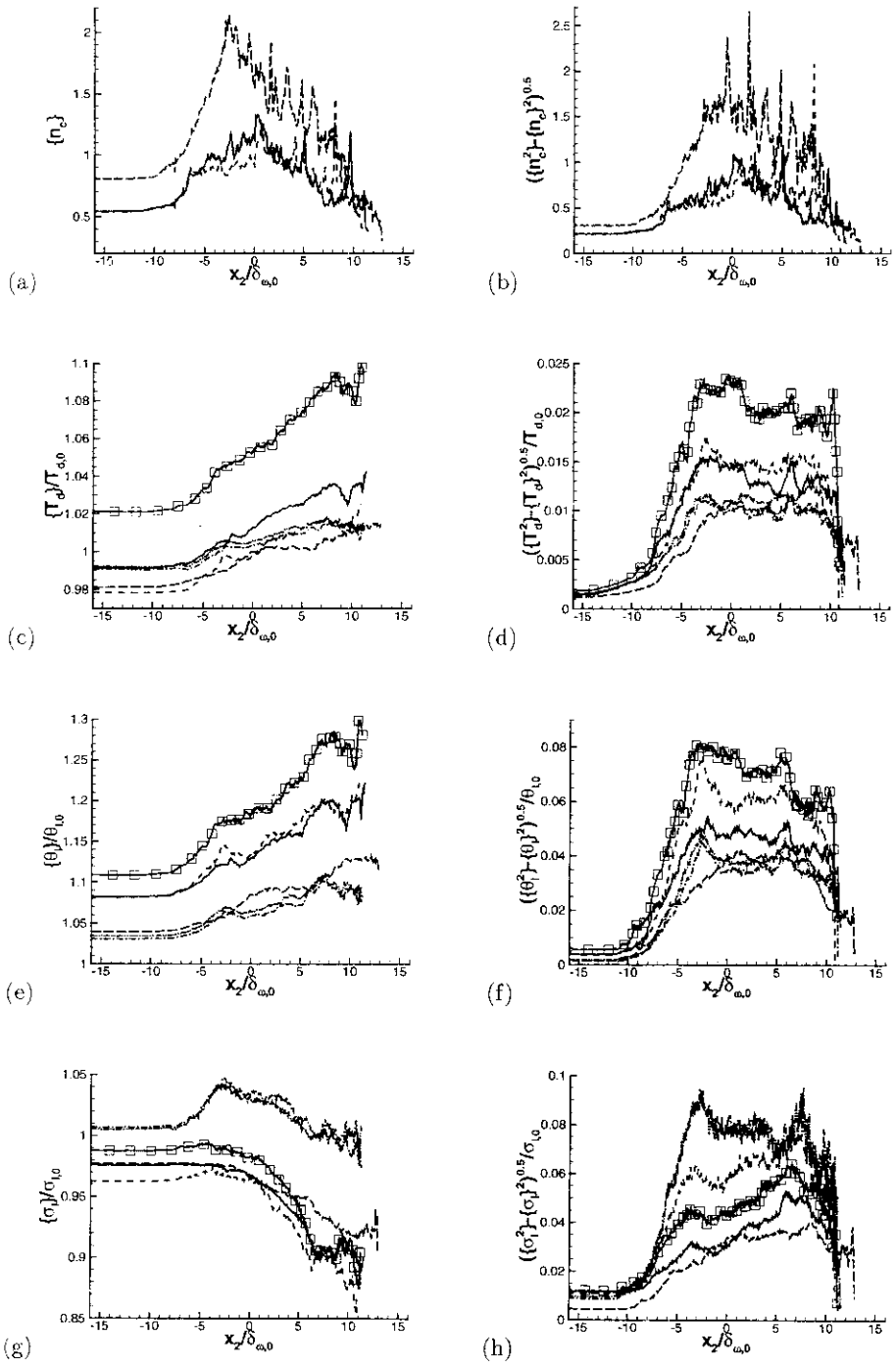

FIGURE 16. Homogeneous (x_1, x_3) plane average drop statistics at t^*_{tr}. For die375ML2R5, die375ML5R5 and jetA375ML2R5 for (a) and (b). (a) $\{n_c\}$, (b) $(\{n_c^2\} - (\{n_c\})^2)^{0.5}$. For die375ML2R5, die375ML5R5, die400ML2R5, jetA375ML2R5, rp1375ML2R5 and jp7375ML2R5 for all following figures. (c) $\{T_d\}/T_{d,0}$, (d) $(\{T_d^2\}/T_{d,0}^2 - (\{T_d\}/T_{d,0})^2)^{0.5}$, (e) $\{\theta_l\}/\theta_{l,0}$, (f) $(\{\theta_l^2\}/\theta_{l,0}^2 - (\{\theta_l\}/\theta_{l,0})^2)^{0.5}$, (g) $\{\sigma_l\}/\sigma_{l,0}$, (h) $(\{\sigma_l^2\}/\sigma_{l,0}^2 - (\{\sigma_l\}/\sigma_{l,0})^2)^{0.5}$. The curve labels are listed in the figure 3 caption.

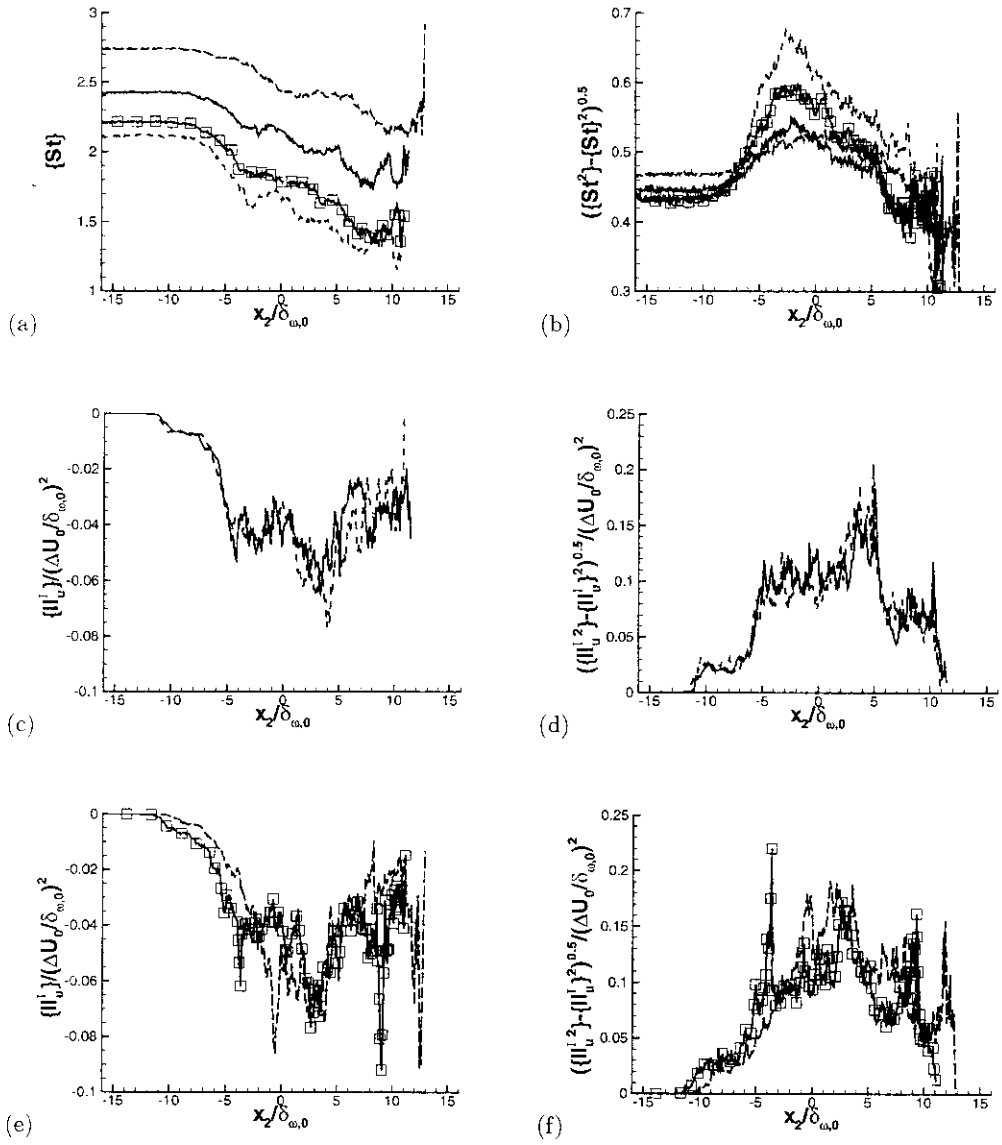

FIGURE 17. Homogeneous (x_1, x_3) plane average drop statistics at t_{tr}^*. (a, b) die375ML2R5, die375ML5R5, die400ML2R5, jetA375ML2R5; (c,d) die375ML2R5, die375ML5R5; (e,f) die400ML2R5, jetA375ML2R5. (a) St, (b) $(\{St^2\} - (\{St\})^2)^{0.5}$, (c) $\{II_u^I\}/(\Delta U_0/\delta_{\omega,0})^2$, (d) $(\{(II_u^I)^2\} - (\{II_u^I\})^2)^{0.5}/(\Delta U_0/\delta_{\omega,0})^2$. The curve labels are listed in the figure 3 caption.

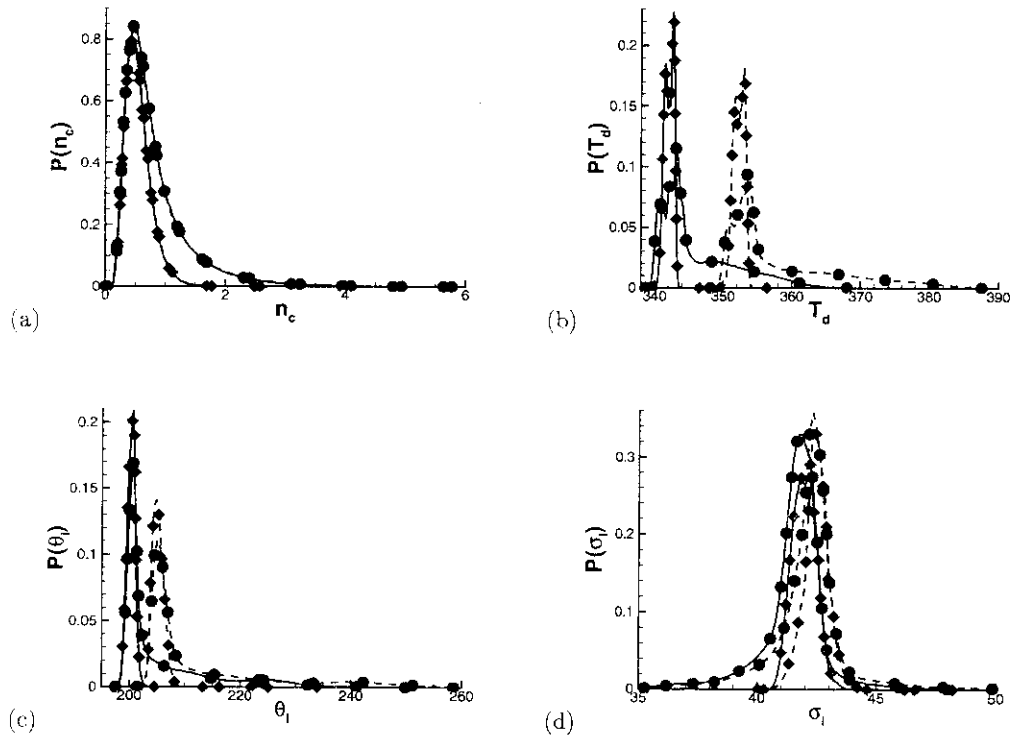

FIGURE 18. Probabilities computed over the drop ensemble in the lower stream (♦) and in the mixing layer (•) for die375ML2R5 and die400ML2R5 at t^*_{tr}. the criterion for defining the lower stream and the mixing layer is that of §3.2.2. The curve labels are changed from those listed in figure 3 caption: die375ML2R5 —— and die400ML2R5 – – –. (a) $P(n_c)$, (b) $P(T_d)$, (c) $P(\theta_l)$ and (d) $P(\sigma_l)$.

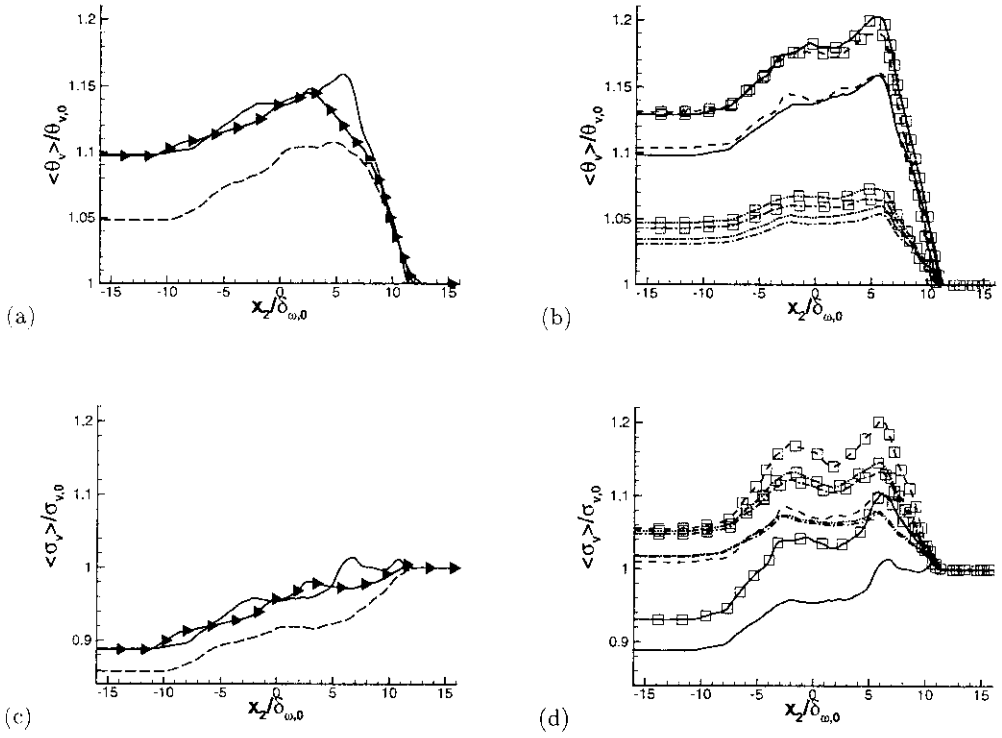

FIGURE 19. Homogeneous (x_1, x_3) plane average vapor composition at t^*_{tr} for all transitional simulations and $t^* = 100$ for die375ML2R2 : (a,b) $\langle\theta_v\rangle/\theta_{v,0}$ and (c,d) $\langle\sigma_v\rangle/\sigma_{v,0}$. (a,c) die375ML2R2, die375ML2R5, die375ML5R5 and (b,d) die375ML2R5, die400ML2R5, jetA375ML2R5, jetA400ML2R5, rp1375ML2R5, rp1400ML2R5, jp7375ML2R5 and jp7400ML2R5. The curve labels are listed in the figures 3, 6 and 5 captions.

b]

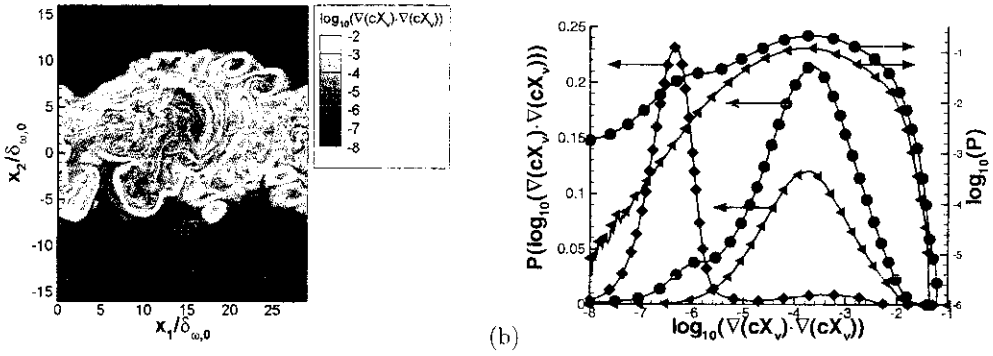

(a) (b)

FIGURE 20. Scalar dissipation rate for die375ML2R5 at t^*_{lr}. (a) visualization of $\log_{10}[(\nabla(cX_v)) \cdot (\nabla(cX_v))]$ in the between-the-braid plane ($x_3/L_3 = 0.5$), and (b) PDFs, where (♦) represents the lower stream, (•) represents the mixing layer restricted to $|x_2/\delta_{\omega,0}| < 8$ (◄) represents the core of the mixing layer restricted to $|x_2/\delta_{\omega,0}| < 4$.

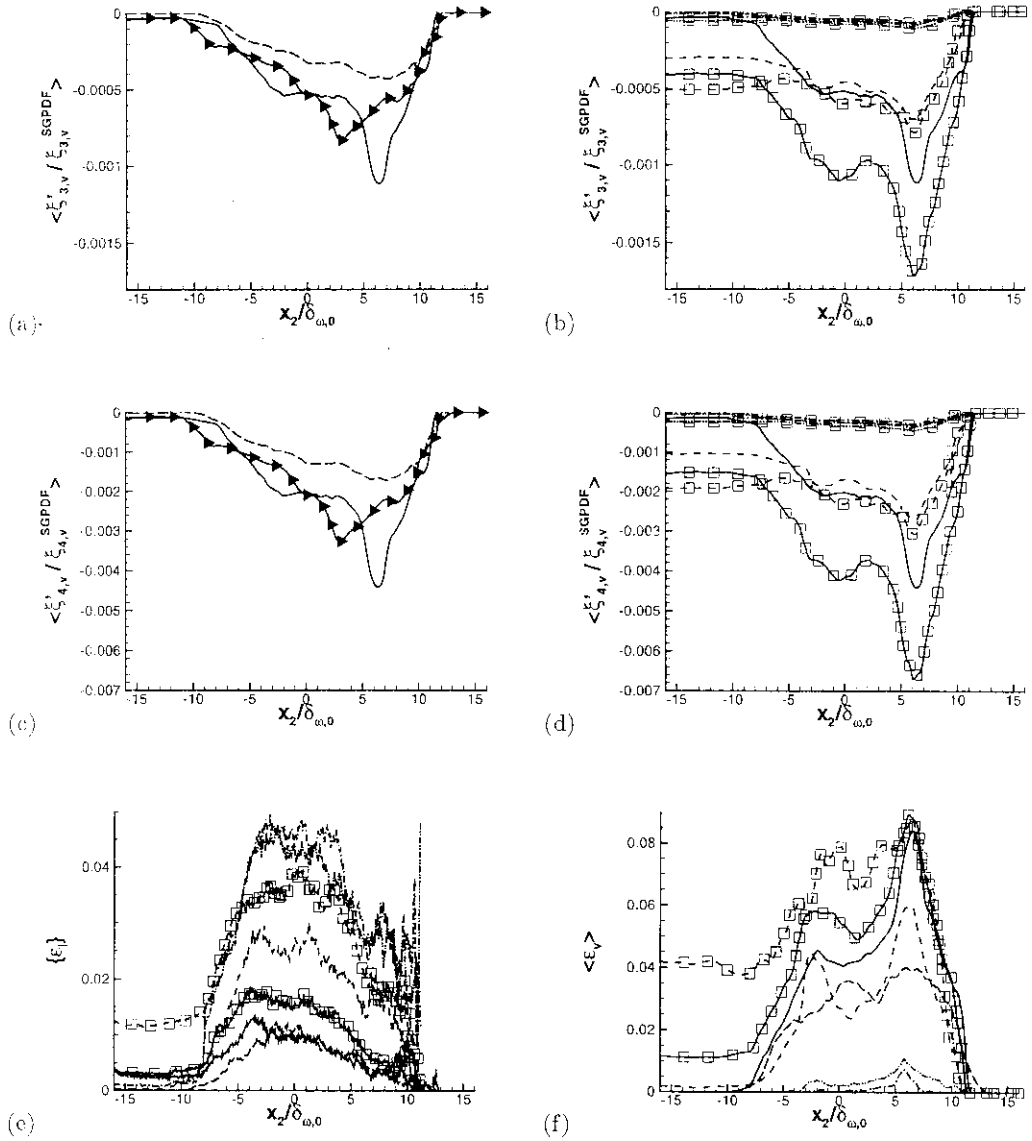

FIGURE 21. Homogeneous (x_1, x_3) plane average vapor composition deviation at t^*_{tr} from the Gamma PDF: (a,b) $\left\langle \xi'_{3,v}/\xi^{SGPDF}_{3,v} \right\rangle$, (c,d) $\left\langle \xi'_{4,v}/\xi^{SGPDF}_{4,v} \right\rangle$, (e) $\{\varepsilon_l\}$ and (f) $\langle\varepsilon_v\rangle$. (a,c) die375ML2R2, die375ML2R5, die375ML5R5; (b,d) die375ML2R5, die400ML2R5, jetA375ML2R5, jetA400ML2R5, rp1375ML2R5, rp1400ML2R5, jp7375ML2R5 and jp7400ML2R5; (e,f) die375ML2R5, die375ML5R5, die400ML2R5, jetA375ML2R5, jetA400ML2R5, rp1375ML2R5 and jp7375ML2R5. The curve labels are listed in the figures 3, 6 and 5 captions.